SURFACE SCATTER OF ANTIREFLECTIVE NANOSTRUCTURED DIELECTRIC INTERFACES

by

David Aaron Gonzalez Jr

A dissertation submitted to the faculty of
The University of North Carolina at Charlotte
in partial fulfillment of the requirements
for the degree of Doctor of Philosophy in
Optical Science and Engineering

Charlotte

2023

Approved by:

Dr. Menelaos Poutous

Dr. Glenn Boreman

Dr. Tino Hofmann

Dr. Nathaniel Fried

Dr. Ritika Prasad

ABSTRACT

DAVID AARON GONZALEZ JR. Surface Scatter of Antireflective Nanostructured Dielectric Interfaces. (Under the direction of DR. MENELAOS K. POUTOUS)

Anti-reflective nanostructured surfaces (ARSS) enhance optical transmission through suppression of Fresnel reflection at boundaries between layered media by creating a gradually increasing ratio of material to air volume fraction. Previous studies show random ARSS (rARSS) exhibit broadband enhancement and polarization insensitivity in transmission when applied to flat optical windows. Windows with rARSS treatment are characterized (transmittance, reflectance, and angular scatter) using spectrophotometry and scatterometry to assess transmission enhancement over a spectral band of interest. Using measured spectral data, partial-integrated scatter values can be obtained, allowing the comparison of random anti-reflective boundary performance to optically flat surfaces. By comparing axial transmission and specular reflection with the scattered performance, an accurate determination of the redistribution of incident energy is obtained. The results show differences in scattered intensity over the wavelength bands of interest, correlating with surface random feature populations.

Rigorous full-wave solvers of light scatter from aperiodic surfaces can be computationally intensive, therefore alternative methods are desired to predict and analyze bi-directional surface scatter. Using a transfer function approach, an approximation of far-field light scatter can be modeled based on surface statistics. rARSS feature topology was determined using optical profilometry to obtain statistical surface roughness parameters and granulometric analysis of nano-roughened substrates SEM images, to assess the structured-surface feature scales. Random rough surfaces, which are generally globally isotropic and polarization insensitive, are well-modeled by Gaussian statistics, making them ideal candidates for a surface transfer function approach of surface scatter analysis. Generalized Harvey-Shack surface scatter theory was used to calculate surface feature diffractive effects. Scatter distributions predicted using a Gaussian parameter model of a random surface and structured surface metrology data were compared to measured scatter data for assessment of the transfer function model validity within the bandlimit of interest. Results show that prediction of wide angle rARSS optical scatter is viable using the transfer function approach, but the theory fails to predict transmission enhancement due to the inclusion of roughness.

DEDICATION

This dissertation is dedicated to…

… my lovely partner in life, Bethany. Without you, I simply couldn’t exist.
Forever and always.

ACKNOWLEDGEMENTS

Most importantly, I would like to thank my advisor, Dr. Menelaos Poutous for his mentorship over the course of my graduate career. Your guidance was paramount to my success. “In order to save the world, first he had to pass Physical Optics.”

Thank you to my committee members, Dr. Glenn Boreman, Dr. Nathaniel Fried, Dr. Tino Hofmann, and Dr. Ritika Prasad for their feedback and advice throughout the dissertation process. I immensely appreciate all of the time my committee has invested in me.

I would like to thank Dr. Nathaniel Fried for the opportunity to work in the Biomedical Optics Laboratory. I learned much about what it means to be an experimentalist from your mentorship and my time working in your lab.

Thank you to the Science, Mathematics, & Research for Transformation (SMART) Scholarship for funding me during my graduate school career. I am lucky to have had the financial support and the opportunity to work with some of the greatest minds of the DoD community.

I would like to thank the Center for Optoelectronics and Optical Communications for the use of its equipment and facilities. Many thanks to Mr. Scott Williams, Dr. Jeffery Thousand, and Dr. Lou Deguzman for their efforts in teaching me how to use the equipment and for listening to my unending rants about the scatterometer.

Thank you to the past and present members of the Optical Micro-Structured Interfaces Laboratory, Abigail Eckart, Karteek Kunala, Praneeth Gadamsetti, Uma Subhash, Subahsree Srinivas, Samir Paudel, Christopher Wilson, and Thomas Hutchens for all the support.

Thank you to the willing (and unwilling) who listened to my unprompted lectures and (mostly) uninformed hypothesis; I thoroughly enjoyed pontificating to rolling eyes and slowly sagging smiles.

Finally, thank you everyone who has been here since the beginning. I will never forget your friendship and care for me over the years. You all make up the greatest family I could ever ask for. Cheers.

TABLE OF CONTENTS

LIST OF TABLES xi

LIST OF FIGURES xii

LIST OF ABBREVIATIONS xviii

CHAPTER 1: INTRODUCTION 1

- 1.1: Antireflective Treatments 1
- 1.2: Nanostructured Surface Fabrication and Characterization 2
- 1.3: Modeling Antireflective Structured Surface Scatter Effects 3
  - 1.3.1: Gradient-index Modeling of Structured Surfaces 3
  - 1.3.2: Modeling Aperiodic Scatter 4
  - 1.3.3: Rayleigh-Rice Surface Scatter Theory 5
  - 1.3.4: Scalar Diffraction Theory 8
  - 1.3.5: Harvey-Shack Surface Scatter Theory 9
  - 1.3.6: Preliminary Modeled Results 12
- 1.4: Dissertation Overview 13

CHAPTER 2: SPECTROPHOTOMETRIC CHARACTERIZATION 15

- 2.1: Introduction 15
- 2.2: Nanostructured Materials for IR Transmission Enhancement 16
  - 2.2.1: Structured Surface Fabrication 16
  - 2.2.2: Spectral Characterization 18
  - 2.2.3: Spectrophotometry Methodology 20
- 2.3: Spectral Analysis of Bidirectional Scatter 21

2.3.1: Single-surface Optical Scatter Results 24
2.4: Measuring Wide-angle Reflected Scatter 25
2.4.1: Directional Scatter Results 25
2.5: Discussion of Spectral Results 31
2.6: Conclusions 32
CHAPTER 3: SCATTEROMETRY 35
3.1: Introduction 35
3.2: Scatterometry Methodology 35
3.2.1: Diffuse Scatter Measurements 37
3.2.2: Nanostructured Surface Scatter in the Visible 43
3.3: Surface Scatter in the Mid-wave Infrared 47
3.3.1: Diffuse Surface Infrared Scatter 48
3.3.2: Nanostructured Surface Infrared Scatter 49
3.4: Discussion of Scatterometry Measurements 51
3.5: Conclusions 53
CHAPTER 4: MODELING OPTICAL SCATTER 56
4.1: Introduction 56
4.1.1: The Generalized Harvey-Shack Surface Scatter Theory 56
4.1.2: Surface Feature Descriptions 57
4.1.3: Recoupling of Evanescent Energy 59
4.2: Surface Profile Characterization 59
4.2.1: Optical Profilometry of Structured Surfaces 61
4.3: Spectral Scatter Characterization 67

4.4: Modeled Scatter using the Generalized Harvey-Shack Theory 69

4.5: Conclusions 79

CHAPTER 5: CONCLUSIONS 81

5.1 Summary of Nanostructured Surface Spectral Characterization 81

5.2 Summary of Experimental and Modeled Optical Scatter 81

REFERENCES 84

APPENDIX A: PUBLICATIONS AND PRESENTATIONS 88

APPENDIX B: EQUIPMENT SPECIFICATIONS 89

APPENDIX C: ADDITIONAL DATA 90

LIST OF TABLES

TABLE 2.1: Surface randomness averaged dimensions for nanostructured ZnSe samples. 18

TABLE 3.1: Angular shift of the maximum BSDF value and angular full width at half max of measured scatter distributions. 41

TABLE 4.1: Selected surface roughness parameters obtained from analysis of UV confocal microscope images. 62

LIST OF FIGURES

FIGURE 1.1: (Left) 10x magnification image of diamond-turned (machined) Al imaged using confocal microscopy. (Right) Height profile slice against the grooves of the surface. Cusps are leftover tooling marks from the machining process. The spatial period of the features is approximately 60 µm. 6

FIGURE 1.2: (Top) Calculated PSD using measured surface height map profile of 60 µm period machined Al. (Bottom) Calculated intensity distribution using the Rayleigh-Rice surface scatter theory at 5° AOI, 633 nm wavelength, and PSD calculated from surface height map as inputs. Grating orders locations were calculated using grating equation. 7

FIGURE 1.3: Calculated intensity distribution of 60 µm period machined Al using the Original Harvey-Shack surface scatter theory with 633 nm wavelength source at 5° AOI. 11

FIGURE 1.4: Comparison of measured scatter data vs. Rayleigh-Rice and Harvey-Shack surface scatter theories for the machined Al shown in Figure 1.1. (Top) Linearly scaled abscissa shows HS theory and experimental data agree up to 45° AOC. RR data was mirrored over the specular direction to produce the angular distribution shown (Bottom) Log-scaled abscissa shows finer details in the scatter distribution at near-specular angles. RR theory agrees very well with measured data. 13

FIGURE 2.1: SEM images of four randomly nanostructured ZnSe surfaces (A-D), including top-down of the structured dielectric surface (left) and monolith features at 45° angle of viewing (right). 17

FIGURE 2.2: (A) Configuration of reflection measurement of the spectrophotometer used in this study. Light is focused onto the transparent sample plane and the reflected cone of light (red shaded area) is collected by rotationally scanning the collection mirror. Nano-roughened substrates may scatter light outside of the directional cone of collection (dotted outlined area). (B) Angular intensity distribution is presented as a directional diagram from -15° to 45° AOC, on a radial logarithmic normalized power scale. An aluminum mirror is used as a background (dashed line). Nano-roughened sample reflected intensity (red circles) is compared to the optically flat sample (black squares). 19

FIGURE 2.3: Measured normal incidence (axial) transmission (T(λ)) and specular reflection at 15° (R(λ)), for the single-surface rARSS processed samples(A-D) (red) and an optically flat ZnSe substrate (black). 19

FIGURE 2.4: Calculated bi-directional scatter (Σ) (grey), single-surface reflectance (R), and single-surface transmittance (T) for each single surface processed ZnSe substrate (red), and the optically flat ZnSe window (black) using Equation 2.3-2.5. Light scatter from the optically flat substrate was negligible over the wavelength band of interest. 25

FIGURE 2.5: Measured reflected directional intensity distributions at 4 µm wavelength, including scattered light outside of the directional cone (+3°< θ_c <+27°). The processed ZnSe surface (red circles) is compared to its unprocessed counterpart (black squares) and the mirror signature (dashed line). 27

FIGURE 2.6: Measured reflected directional intensity distributions at 10 µm wavelength, including scattered light outside of the directional cone (+3°< θ_c <+27°). The processed ZnSe surface (red circles) is compared to its unprocessed counterpart (black squares) and the mirror signature (dashed line). 27

FIGURE 2.7: Measured reflected angular intensity distribution at 4 µm wavelength, from the rARSS substrates (red circles), the unprocessed ZnSe window (black squares), and the reference mirror (dashed line), presented as logarithmic reflectance functions of parameter $\beta = \sin(\theta_c)$. 29

FIGURE 2.8: Measured reflected angular intensity distribution at 10 µm wavelength, from the rARSS substrates (red circles), the unprocessed ZnSe window (black squares), and the reference mirror (dashed line), presented as logarithmic reflectance functions of parameter $\beta = \sin(\theta_c)$. 29

FIGURE 2.9: Processed samples (ZnSe:A–D) are characterized by comparing their reflectance distribution contour gradients to that of the optically flat sample (ZnSe:O). 30

FIGURE 3.1: (Left) Photograph of CASI scatterometer setup with visible HeNe laser source. The sample is visible on the right edge of the photograph; the detector arm is beyond the image. (Right) Diagram of the CASI scatterometer layout. A laser source is directed towards the sample located at the center of rotation of the setup, with detector capable of measuring radiance over the 36

equatorial plane of the unit sphere. The detector aperture size is adjusted for specific angular ranges as the detector scans across the hemisphere.

FIGURE 3.2: FS substrates of different roughness scales were measured using confocal microscopy taken with 405 nm UV laser illumination. (Left to right): optical quality FS flat, ground FS, and rARSS added FS surfaces. Samples with nanostructures were processed using random gold masking and etch method explained in Chapter 1. Statistical distributions of surface features (lateral spacing and depth of features) conventionally determine the spectral response of the interface. 37

FIGURE 3.3: Measured BSDF of ground glass obtained using the CASI. 38

FIGURE 3.4: Scaling BTDF by cosine of the scatter angle produces a radiant intensity distribution. Due to the cosine dependence, the distribution approaches zero at large (>85°) angles of collection. 39

FIGURE 3.5: Beta-projection BSDF. Scatter distribution is projected into cosine space by taking the sine of the collection angle ($\beta = \sin\theta_s$). 39

FIGURE 3.6: Near shift-invariance of the scatter distributions is visualized using shifted coordinates (β-β_0) based on the incidence ($\beta_0 = \sin\theta_i$) and collection ($\beta = \sin\theta_s$) angles. 40

FIGURE 3.7: Shift of the distribution, by the BTDF peak value per AOI, shows the light transverse profile FWHM to be similar in value. The distributions have an average width of 17.6° ± 2.0°. 41

FIGURE 3.8: Logarithmic scaling of the diffuse scatter distribution reveals the wide-angle scatter is non-negligible. 42

FIGURE 3.9: Curve fit of the BSDF peak value vs. AOI (left). Fitted BSDF distribution at normal incidence calculated using empirical fit from the literature (right). 43

FIGURE 3.10: Single rARSS sample has an enhancement of 3.5% at the scatter wavelength of interest (top). BTDF of the rARSS sample (solid line) compared to an optical flat (points) at normal, 15°, and 50° AOI. rARSS sample has enhanced trasnmission and narrow paraxial scatter, compared to the polished surface, but with increased wide angle scatter (middle). Limiting the abscissa and converting the collection angle to shifted-beta shows the shift-invariance of measured scatter (bottom). 45

FIGURE 3.11: BRDF of selected rARSS samples compared to optical flat, gold mirror, and dielectric mirror. Compared to the optical flat, the rARSS wide angle scatter is increased by three orders of magnitude, while it has increased by two orders of magnitude in the paraxial region. For the rARSS samples, the specular peak was suppressed by 50% compared to their optically flat counterpart. 46

FIGURE 3.12: Comparison of single-surface processed (grey) nano-roughened ARSS samples to their double-sided processed (red) ARSS counterpart and optical flat (black). The amount of scatter increases with added surface roughness and is the higher for the double-sided roughened sample. 46

FIGURE 3.13: LEXT confocal images of infrared windows with different surface feature size scales, measured with 405 nm UV laser illumination. 48

FIGURE 3.14: BTDF of ground glass samples normal (black), 15° (red), 30° (gray), 45° (dark red), and 70° (teal) AOI. Fused Silica (left) and Si (right) ground glass BTDF provide a baseline for the scattering characteristics of a surface with features comparable to the incident wavelength. Ground Si, which has a peak depth comparable to the incident wavelength, scatter distribution values span five orders of magnitude compared to nine orders difference between peak and side angle scatter values for ground FS. 49

FIGURE 3.15: Spectra of the flat and processed rARSS samples (left column) and their BTDF at wavelength labeled in the spectral graphs. Optical flat (middle column) and rARSS (right column) BTDF at normal (black), 15° (red), 30° (gray), 45° (dark red), and 70° (teal) AOI are presented. rARSS samples had enhanced transmission and narrowed paraxial scatter than the flat. Ge rARSS substrates have increased wide angle scatter (top right) while Si rARSS scatter is nearly unresolvable by the setup (bottom right). 51

FIGURE 4.1: SEM micrographs of rARSS in: (A) – fused silica and, (B) – silicon. The corresponding granulometric normalized (to the measured areas) histograms are shown as (C) and (D). The red bars indicate island distributions, and the black bars void distributions. 60

FIGURE 4.2: LEXT UV confocal images of polished FS (A), unpolished FS (B), rARSS FS (C), polished Si (D), unpolished Si (E), and rARSS Si (E) at 100x magnification. For reference, rARSS 63

images (C and F) include inset of their respective SEM image shown in Figure 1. Images were processed using accompanying LEXT software to obtain selected surface roughness parameters shown in Table 4.1.

FIGURE 4.3: Polished FS (A), unpolished FS (B), rARSS FS (C), polished Si (D), unpolished Si (E), and rARSS Si (F) experimental PSD (black) was calculated by FFT of the surface height map profile and Gaussian PSD (red) was calculated by inserting surface roughness parameters into a characteristic Gaussian equation (PDF) for random systems. PSD cutoff frequency (vertical black dotted line) at normal incidence for the experimental wavelength of interest is shown for visualization of limits for calculation of the relevant roughness of the surface. 65

FIGURE 4.4: Polished FS (A), unpolished FS (B), rARSS FS (C), polished Si (D), unpolished Si (E), and rARSS Si (F) experimental ACV was calculated via serial multiplication of the measured surface height map profile. (Left) Three-dimensional output of ACV calculation. (Middle) Top-down visualization of experimental ACV. (Right) Comparison of experimental ACV (black) array slice taken in the y = 0 µm plane and Gaussian ACV (red). 66

FIGURE 4.5: FS (left) and Si (right) of polished and nanoroughened rARSS samples normal incidence axial transmission (T(λ)), 15° AOI specular reflection (R(λ)), and calculated TIS (Σ(λ)). 67

FIGURE 4.6: Experimental TIS (grey) is compared to theoretical TIS (teal) for two rARSS samples. (Left) Theoretical TIS for rARSS FS matches the trend of experimental TIS for shorter wavelengths. (Right) Theoretical and experimental TIS follow similar $1/e^2$ trends, but with mismatched slopes. 68

FIGURE 4.7: Calculated ASF (solid line) using a Gaussian model of the surface ACV (left) and experimentally derived ACV (right) is compared to measured BTDF (points) at 633 nm for ground FS samples at normal (black), 15° (red), and 50°(grey) AOI. The specular (axial) transmitted angle is notated by a vertical dotted line. Specular peak is suppressed for experimental data and scatter distributions were normalized for comparison of measured and simulated data. 71

FIGURE 4.8: Calculated ASF (solid line) using a Gaussian model of the surface ACV (left) and experimentally derived ACV (right) is compared to measured BTDF (points) at 633 nm for ground Si samples at normal (black), 15° (red), and 50°(grey) AOI. The specular 72

(axial) transmitted angle is notated by a vertical dotted line. Specular peak is suppressed for experimental data and scatter distributions were normalized for comparison of measured and simulated data.

FIGURE 4.9: Calculated ASF (solid line) using a Gaussian model of the surface ACV (left) and experimentally derived ACV (right) is compared to measured BTDF (points) at 633 nm for polished FS samples at normal (black), 15° (red), and 50°(grey) AOI. 74

FIGURE 4.10: Calculated ASF (solid line) using a Gaussian model of the surface ACV (left) and experimentally derived ACV (right) is compared to measured BTDF (points) at 3.39 μm for polished Si samples at normal (black), 15° (red), 45° (grey), and 70° (dark red) AOI. 75

FIGURE 4.11: Calculated ASF (solid line) using a Gaussian model of the surface ACV (left) and experimentally derived ACV (right) is compared to measured BTDF (points) at 633 nm for nanostructured FS samples at normal (black), 15° (red), and 50°(grey) AOI. 76

FIGURE 4.12: Calculated ASF (solid line) using a Gaussian model of the surface ACV (left) and experimentally derived ACV (right) is compared to measured BTDF (points) at 3.39 μm for nanostructured Si samples at normal (black), 15° (red), 45° (grey), and 70° (dark red) AOI. 77

LIST OF ABBREVIATIONS

ACV	Autocovariance
Al	Aluminum
AlN	Aluminum Nitride
AOI	Angle of incidence
AR	Anti-reflective
ARSS	Anti-reflective structured surface
ASF	Angle spread function
Au	Gold
BDS	Bidirectional scatter
BRDF	Bidirectional reflection distribution function
BSDF	Bidirectional scattering distribution function
BTDF	Bidirectional transmission distribution function
CASI	Complete Angle Scattering Instrument
FFT	Fast Fourier Transform
FS	Fused Silica
FWHM	Full width at half max
Ge	Germanium
GHS	Generalized Harvey-Shack
HeNe	Helium Neon
HS	Harvey-Shack
IR	Infrared

LWIR	Long-wave infrared
MWIR	Mid-wave infrared
Ni	Nickel
NIR	Near-infrared
PSD	Power spectral density
rARSS	Random anti-reflective structured surface
RCWA	Rigorous coupled wave analysis
RIE	Reactive ion etching
RR	Rayleigh-Rice
S_a	Arithmetic average height
S_{al}	Autocorrelation length
SEM	Scanning electron microscope (or microscopy)
Si	Silicon
S_q	Root-mean-square height
STF	Surface transfer function
S_{tr}	Surface texture ratio
S_z	Peak-valley height
TIS	Total integrated scatter
UV	Ultraviolet
ZnSe	Zinc Selenide

CHAPTER 1: INTRODUCTION

1.1: Antireflective Treatments

Ideally, every optical system would perform at its highest efficiency—components would be lossless and without aberration errors. High power laser applications would benefit from increased transmission throughput without potential damage to other components or personnel [1]. Conversely, every photon counts in low power astronomical imaging systems where there is a continuous need to see fainter objects [2]. Improving light throughput of an optical system can improve contrast and clarity of the image, hopefully without sacrificing resolution.

Real optical components are not ideal and therefore not lossless. Fresnel reflection occurs when light is incident on boundaries separating dielectric regions with different optical refractive indices, and results in energy redirection, extinction, or both, within the incident and transmitted direction of propagation. Anti-reflective (AR) treatments, such as thin-film coatings, suppress reflections by destructive interference along the propagating directional axis. Reducing the reflection from the surface subsequently enhances the transmission throughput of the surface and can be beneficial for applications ranging from photovoltaics to infrared astronomy [1-3]. AR treatments can be grouped into two categories, homogeneous and inhomogeneous, based on the type of surface used to produce the reflectivity-suppressing effect.

Thin films fall into the homogeneous category of AR surfaces. These can be single- or multi-layered, with designs reliant on the substrate material and the bandwidth over which AR performance is desired. The simplest case, a perfect single-layer thin film, eliminates reflection by inducing a π phase shift to the wavefront as it passes through the film. For this to occur, the thin film needs a thickness equal to odd multiples of quarter wavelengths (λ/4) and a refractive index equal to the geometric mean of the substrate and superstrate refractive index ($\sqrt{n_0 n_s}$) where n_s and n_0 are the refractive index of the substrate and superstrate, respectively [4]. Unfortunately, single-layer perfect thin films cannot effectively produce broadband AR effects, are limited to moderate angles of incidence (AOI), and materials with the required refractive index simply do not exist for most cases. Multi-layer thin films are engineered to subvert the limitations in bandwidth, AOI, and choice of materials but are much more complicated to produce [3].

Inhomogeneous surfaces produce an AR effect through gradual transition of superstrate to substrate refractive index. Gradient index materials "soften" the discontinuity between material boundaries, hereby reducing Fresnel reflection [4-6]. Structured materials achieve a gradient boundary by controlling the surface feature density (fill-fraction) and can be approximated by an effective index for analysis, similar to a single layer thin film. By fabricating a surface with specific feature density, a perfect "thin film" layer can be achieved.

AR structured surfaces (ARSS) transverse components, period (cell size) and feature size, are generally subwavelength. Because the feature size is smaller than the incidence wavelength, only the zeroth order propagates while all other diffracted orders become evanescent. Modifying the feature shape or slope changes the material fill-fraction (e.g., monolithic vs. conic structures), and can be used to tune the AR effect bandwidth. Wide bandwidth AR effects are achieved by creating high aspect ratio features [8].

Random anti-reflective structured surfaces (rARSS) are a subset of subwavelength gradient index materials used as an alternative to thin film coatings, with broadband response, high transmission across wide ranges of AOI, and polarization insensitivity—reducing Fresnel reflections in the visible and infrared (IR) [9-12].

1.2: Nanostructured Surface Fabrication and Characterization

In this case, rARSS are fabricated by top-down microlithography methods. Substrates are coated with a porous layer of metal which is either etched directly or thermally annealed. To achieve the necessary aspect ratio for broadband antireflectivity, sample may be coated with a dielectric layer before applying the metal layer to act as a buffer for deep etching. The distribution of metallic islands acts as a random-distribution mask which is transferred to the substate via reactive ion etching [13-14].

Since rARSS are made to be antireflective, it is necessary to characterize their optical performance. Experiments use spectrophotometry to give information on the bandwidth of transmission enhancement and potential parasitic diffractive effects. Optimally, rARSS will reduce reflection while also enhancing axial transmission. In unoptimized cases, it is possible that the addition of structures can cause a reduction of reflection and transmission simultaneously. Scatter induced at an interface can potentially diminish image contrast or resolution, inhibiting the performance of imaging or signal processing systems.

1.3: Modeling Antireflective Structured Surface Scatter Effects

1.3.1: Gradient-index Modeling of Structured Surfaces

Modeling topological scatter can aid in the prefabrication process of structured surfaces and can explain the mechanism behind finalized AR spectral response. Previously, AR effects have been correlated with the nanostructure density, simulating an effective-medium gradient-index boundary profile as a thin film [16]. For wavelengths much larger than the structured surface features, the AR effect is accurately modeled. However, because the surface is a structured diffractor, not a perfectly smooth thin film, short-wavelength optical scatter present in experimental measurements is not accurately represented by the model.

Rigorous coupled-wave analysis (RCWA) can be used to analyze diffraction by general periodic dielectric surfaces bounded by two different media. RCWA solves the resulting electric field amplitude and distribution after perturbation of a surface with an incident wavefront by defining strict boundary conditions via scattering matrices [17-18]. The surface is modeled using a layered approach, similar to effective thin films, with each layer having a density defined by a spatial period and feature size. Using this model, it is efficient to calculate the diffraction pattern from structured surfaces ranging from binary, 50% duty cycle, gratings to multilevel phase holograms. Unfortunately, the theory is restrictive in the requirements for solving boundary conditions [18]. For aperiodic surfaces such as rARSS, it can be difficult to accurately represent the full spectrum of spatial periods that define the surface profile without extremely high-fidelity simulations, extending computation time. Additionally, the unit cell over which the calculations occur can induce incorrect scatter behavior due to periodic effects. Although the theory is rigorous, alternative methods are desired to predict and analyze bi-directional surface scatter without periodic requirements and long computation time.

1.3.2: Modeling Aperiodic Scatter

Complex (random, aperiodic) surfaces with a continuum of spatial features can be modeled using statistical parameters obtained via profilometric measurements. Topological nano-scale features on surfaces are described using statistical distributions, which quantify their transverse-size population groupings (cross-sections), their packing density, and their height values (or depth below the original surface level) [19]. Redistribution of light from the wavevector axial region into wider angles correlates with the relevant high-spatial frequencies approaching the order of the incident wavelength; conversely, mid-spatial frequencies are generally responsible for broadening the near-specular beam width in the far field [20-25]. Statistical surface profiles therefore give insight into the directional scatter of interfaces and visa-versa.

Surface profiles and statistical parameters are obtained using profilometry and optical metrology. Surface roughness parameters are mathematical definitions of surface feature distributions that provide varying levels of surface information based on the specific calculation and application of the parameter. For example, it has been shown that random rough surfaces generally have Gaussian distributions of scaled features and can be approximately characterized by a surface root-mean-square roughness parameter [26].

1.3.3: Rayleigh-Rice Surface Scatter Theory

The surface scatter model developed by Lord Rayleigh uses the full spectrum of spatial features, relating the incident wavelength of light λ, angle of incidence θ_i, angle of viewing θ_s, and roughness of the surface to the observed scatter distribution $I(\theta_i, \theta_s)$

$$I(\theta_i, \theta_s) = \left(\frac{16\pi^2}{\lambda^4}\right)\cos\theta_i \cos\theta_s Q S_2(f_x, f_y) \tag{1.1}$$

where Q is the polarization dependent reflectance of the surface, and S_2 is the 2-dimensional power spectral density (PSD) S_2 describing the rough surface [27]. Rayleigh-Rice (RR) theory follows a vector perturbation model and is dependent on the incident polarization of light. The material refractive index and incident and collection angles are used to calculate the surface reflectance. Q has four functional forms depending on incident wavefront and detector s- and p- polarization combinations (parallel and cross terms) [20]. When considering measurements in the plane of incidence, the cross-polarization terms are zero. In the specular direction, the polarization equation reduces to the familiar Fresnel reflection coefficients [ref]:

$$\begin{aligned} R_s(\theta_i) &= \left|\frac{n_1 cos\theta_i - n_2 cos\theta_s}{n_1 cos\theta_i + n_2 cos\theta_s}\right|^2 = Q_{ss} \\ R_p(\theta_i) &= \left|\frac{n_1 cos\theta_s - n_2 cos\theta_i}{n_1 cos\theta_s + n_2 cos\theta_i}\right|^2 = Q_{pp} \end{aligned} \tag{1.2}$$

The nearly single spatial frequency surface of diamond turned aluminum (Al) is a basic example of a diffractive scattering surface. Frequency content along the surface is mostly due to tooling marks leftover from the diamond tip, at a spatial frequency related to the machine cutting speed, with some noise due to imperfections in the material surface (Figure 1.1). Based on the fabrication parameters, the Al part was expected to have a spatial period of 60 µm.

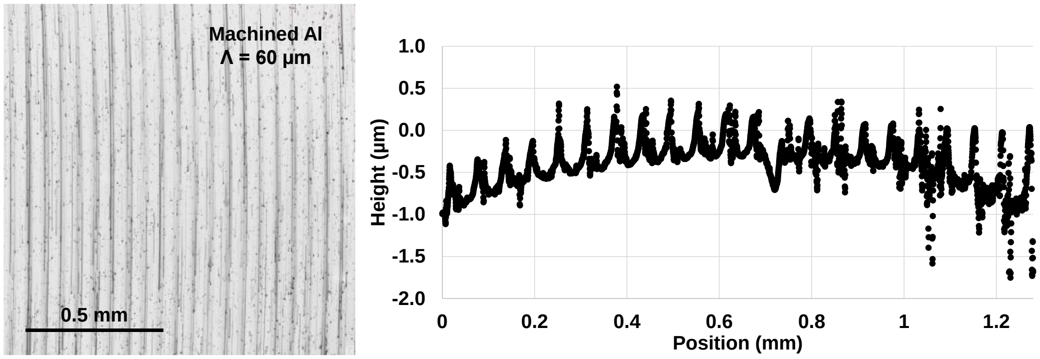

Figure 1.1. (Left) 10x magnification image of diamond-turned (machined) Al imaged using confocal microscopy. (Right) Height profile slice against the grooves of the surface. Cusps are leftover tooling marks from the machining process. The spatial period of the features is approximately 60 µm.

PSD function is calculated by taking a Fourier transform of the 2-dimensional height map profile obtained via optical profilometry [28-29]. The PSD gives functional information on the total spatial content of the surface, limited by the modality of the measurement tool. A Fourier transform of the machined Al height profile is shown in Figure 1.2 top. The PSD has strong peaks at 0.0164, 0.0336, 0.050, 0.0664 µm^{-1}, indicating an actual tooling period of 61 µm and its second, third, and fourth harmonics. Other harmonics are present but are masked by the continuous low frequency spectrum.

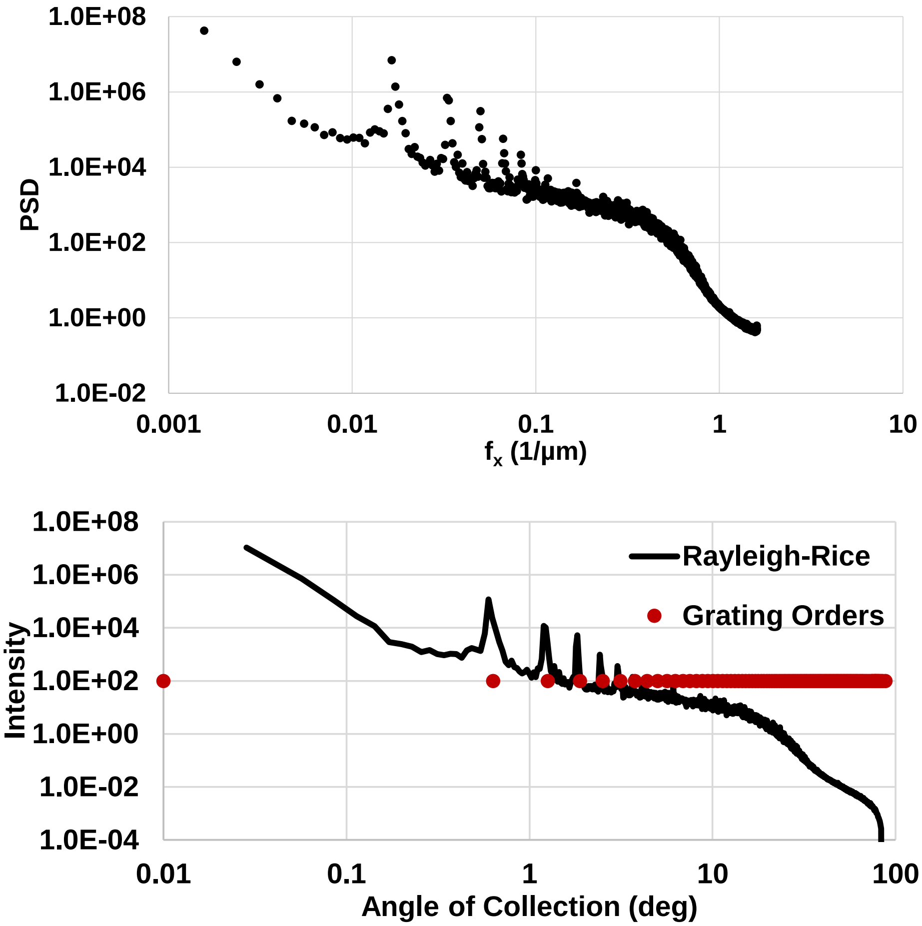

Figure 1.2. (Top) Calculated PSD using measured surface height map profile of 61 µm period machined Al. (Bottom) Calculated intensity distribution using the Rayleigh-Rice surface scatter theory at 5° AOI, 633 nm wavelength, and PSD calculated from surface height map as inputs. Grating orders locations were calculated using grating equation.

Using the PSD of the machined Al surface as input for the RR theory, we calculated the expected scatter of the surface at 633 nm (Figure 1.2 bottom). The functional form of the RR theory depends heavily on the PSD, therefore the harmonic peaks are present as diffraction orders. Diffraction order locations calculated using the grating equation ($m\lambda =$

$d(\sin\theta_i + \sin\theta_s)$, where m is the grating order and d is the grating period) are presented alongside RR scatter data. Analysis of the PSD peaks revealed the spatial period is closer to 61.0 µm, and the grating equation prediction agrees based on the closely matching grating order locations.

RR theory is used when surfaces are considered sufficiently smooth compared to the incident wavelength of light. In this case, the transverse spatial features of the surface are on the order of 100x larger than the probing wavelength of 633 nm. Additionally, the depth of these features ranges from 2-5 µm. For random nanorough surfaces, the transverse features are subwavelength, almost 10-100x smaller than the incident wavelength, but the depths are on the order of the wavelength. This means that nano-rough surfaces are not "smooth" compared to low aspect ratio scalloped machined surfaces that diffract light similarly to sinusoid gratings. Diffuse rough surfaces do not scatter light into distinct orders, but a continuum. A general diffraction theory can take input in the form of pupil functions, and determine the distribution of light in angular space.

1.3.4: Scalar Diffraction Theory

The Kirchoff diffraction theorem can be used to find the diffraction pattern of an aperture $g(x_0,y_0)$ when illuminated by a point source of wavelength λ and projected onto a screen at a distance r [4]. Development of the theory considers a source at the origin (denoted by a "*0*" subscript), with the resulting diffraction pattern at a position (x_i,y_i) . In rectangular coordinates, this is expressed by:

$$u(x_i, y_i) = \frac{1}{j\lambda} \iint_{-\infty}^{\infty} \frac{g(x_0, y_0) e^{jkr}}{r} dx_0 dy_0 \tag{1.3}$$

where

$$r = \sqrt{z_i^2 + (x_i + x_0)^2 + (y_i + y_0)^2}$$

In the far-field region, where $(x_0 - x)^2 + (y_0 - y)^2$ is less than z_i^2, we can take a binomial expansion of r:

$$r \cong z_i + \frac{{x_i}^2 + y_i^2}{2z_i^2} - \frac{x_i x_0 + y_i y_0}{z_i} + \frac{x_0^2 + y_0^2}{2z_i} - \frac{[(x_i - x_0)^2 + (y_i - y_0)^2]^2}{8z_i^3} \ldots \qquad (1.4)$$

Keeping the first three terms in Equation 1.4 designates the region called the far-field region or Fraunhofer regime. The case of including the first four terms of Equation 1.4 is known as the near-field region or Fresnel regime. If the region of interest is very close to the aperture, these approximations are no longer applicable, and the binomial expansion cannot be applied [4,30].

For complex apertures that consist of features much smaller than probing wavelengths, and physical measurements of scale that far exceed the size of the features of interest, the far field approximation is of best application, therefore we can use the first three terms of Equation 1.4 to examine the resulting diffraction pattern. Considering the first three terms of Equation 1.4 with $r \cong z_i$ in the denominator, Equation 1.2 becomes

$$u(x_i, y_i) = \frac{1}{j\lambda z_i} e^{jk(z_i + \frac{x_i^2 + y_i^2}{2z_i})} \iint_{-\infty}^{\infty} g(x_0, y_0) e^{-j2\pi(\frac{x_i x_0}{\lambda\, z_i} + \frac{y_i y_0}{\lambda\, z_i})}\, dx_0 dy_0 \qquad (1.5)$$

Equation 1.5 is the Fourier transform of the aperture function $g(x_0,y_0)$. For well behaving functions, such as rectangular aperture, analytical solutions of Equation 1.5 are possible. More complex pupil functions that include broadband frequency contributions are more difficult to solve without using characteristic functions approximations but can be easily solved numerically using Fourier transform algorithms.

1.3.5: Harvey-Shack Surface Scatter Theory

Using a linear-systems transfer function approach, an approximation of far-field light scatter can be modeled based on surface statistics. Harvey originally described the effects of surface scatter as aberration errors (residual roughness) for structured (machined) surfaces [31]. The higher order terms from Equation 1.4 encompass the range of spatial frequencies present on the surface that contribute to diffractive scatter. Using the machined Al surface, we can explore the Harvey-Shack (HS) surface scatter theory.

Based on empirical data showing the shift invariance of radiance, Harvey and Shack produced a linear systems formulation for examining scatter behavior [31]. HS surface scatter theory requires that the surface $h(x,y)$ is a single-valued Gaussian random process, the roughness is locally stationary (isotropic), any pair of random variables along the surface are jointly normal (linear combinations of heights along the surface have a normal distribution), and the sampled surface is ergodic (sample groups taken of the surface generally represent the surface as a whole). With these requirements, Harvey derived the Original Harvey-Shack scatter theory [20].

The surface transfer function (STF) of a surface is similar to traditional modulation and optical transfer functions. The STF is based on a complex pupil function, $P(x,y) = a(x,y)e^{j\phi(x,y)}$, similar to the aperture function, $g(x_0,y_0)$, introduced in Equation 1.3. The pupil amplitude, $a(x,y)$, is uniform (equal to the root of the Fresnel coefficient of the surface) and the phase, $\phi(x,y)$, is imparted on the wavefront due to height variations (roughness) along the surface. Taking the Fourier transform of the STF yields the angle spread function (ASF).

The STF can be written as

$$STF(x,y) = e^{-(4\pi\sigma_s)^2[1-ACV(x,y)/\sigma_s^2]} \tag{1.6}$$

where *ACV* is the 2D autocovariance function, and σ_s is the rms surface roughness. Equation 1.6 can be parametrized into specular and diffuse components, and ultimately Fourier transformed to obtain the *ASF*:

$$ASF(\alpha,\beta) = F\big(STF(x,y)\big) \tag{1.7}$$

where α and β are direction cosine coordinates. *ASF* is converted to radiant intensity by multiplying Equation 1.6 by an angular cosine term (assuming unit power illumination).

HS theory uses the autocovariance as its functional form, rather than the PSD. Autocovariance function (ACV) is calculated via serial multiplication or Fourier transform (Weiner-Khinchin theorem) of a zero-mean surface height profile [32]. The transverse (aperture) features of the surface are not considered in Harvey's theory, only the feature heights (phase imparted on the wavefront). Using the ACV and rms surface roughness as input, we can calculate the scatter distribution of the machined Al shown in Figure 1.1 (Figure 1.3).

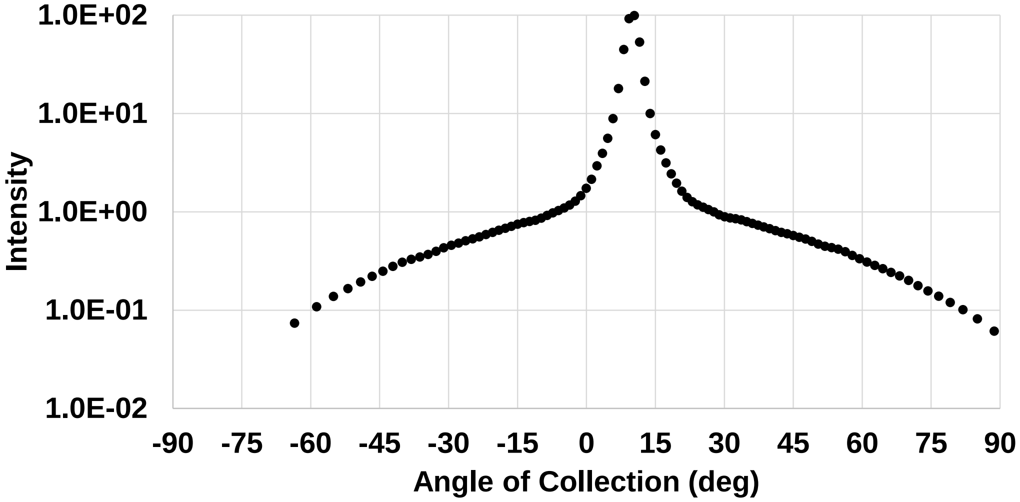

Figure 1.3. Calculated intensity distribution of 60 µm period machined Al using the Original Harvey-Shack surface scatter theory with 633 nm wavelength source at 5° AOI.

Diffraction orders are not present in the resulting scatter distribution (Figure 1.3) because the HS algorithm uses surface-averaged parameters as inputs, smoothing over fine details in the scatter pattern. Random rough surfaces are ideal candidates for a surface transfer function approach of scatter analysis because they are generally globally isotropic and polarization insensitive, are well-modeled by Gaussian statistics, and have height features on the order of the incident wavelength for wavebands of transmission enhancement [11,12].

1.3.6: Preliminary Modeled Results

The final aspect of the scatter problem relies on experimental scatter measurements. Spectrophotometry alone gives limited data on the scatter properties of a surface, namely the axial transmission and specular reflection. Using scatterometry techniques discussed in Chapter 3, we measure the equatorial slice of a full 4π sr scatter distribution from a structured surface [21]. Experimental and theoretical values are compared for judgement of machined Al scatter performance (Figure 1.4). RR theory accurately predicts the location and magnitude of the diffraction orders near specular, while the HS theory averages out the orders and extends further into wider angles than RR.

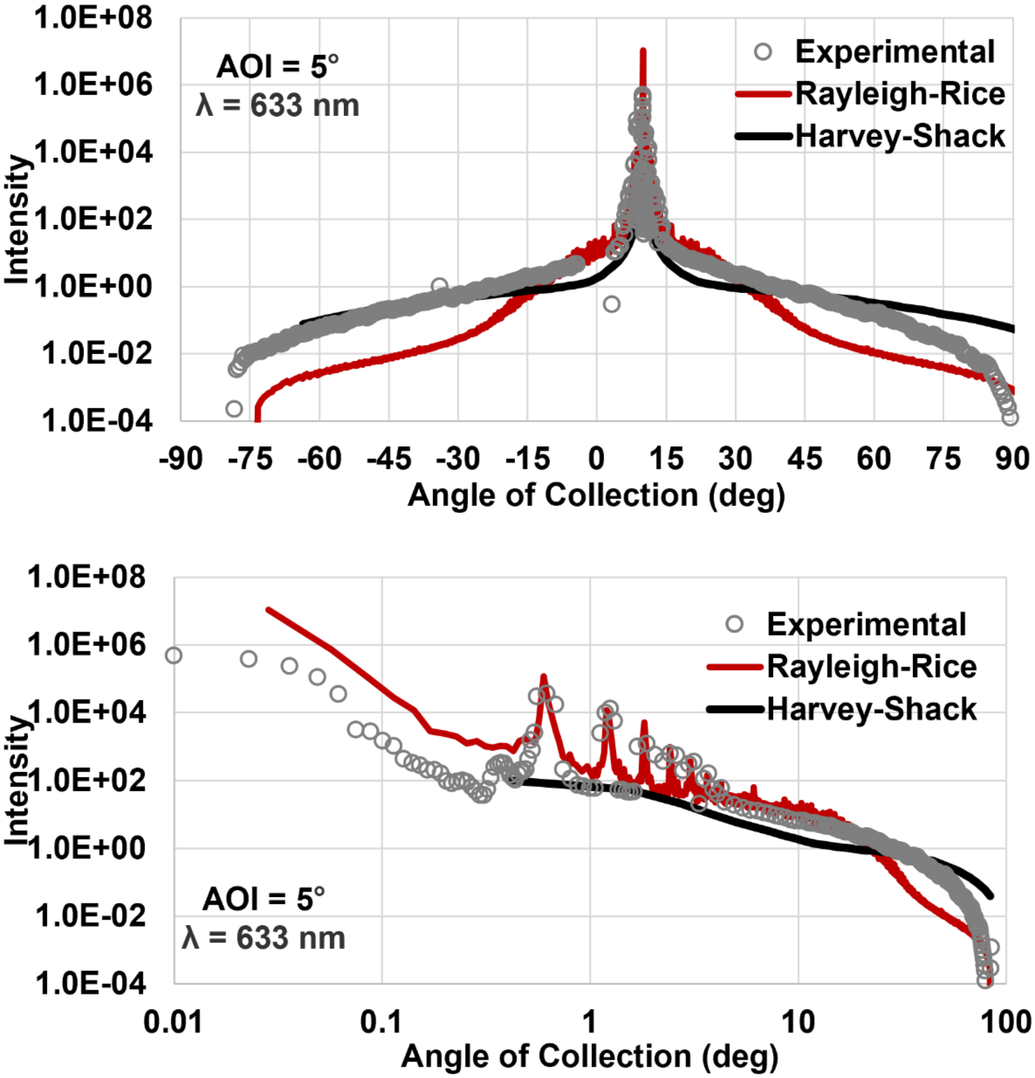

Figure 1.4. Comparison of measured scatter data vs. Rayleigh-Rice and Harvey-Shack surface scatter theories for the machined Al shown in Figure 1.1. (Top) Linearly scaled abscissa shows HS theory and experimental data agree up to 45° AOC. RR data was mirrored over the specular direction to produce the angular distribution shown (Bottom) Log-scaled abscissa shows finer details in the scatter distribution at near-specular angles. RR theory agrees very well with measured data.

1.4: Dissertation Overview

Chapter 1 introduced the concept of diffractive scatter from structured surfaces and showed the viability of measuring and predicting reflected optical scatter from a trivial, periodic, macro-structured surface. Characterization of aperiodic, nano-structured dielectric surfaces made for transmission enhancement is the goal of this project. Chapter 2 explores traditional spectrophotometry for optical characterization, and calculations of scatter using measured spectral data. Chapter 3 revisits the methodology of scattering measurements and showcases data for micro-rough and nano-rough diffusers in both the visible and infrared spectrum. Chapter 4 focuses on the Generalized Harvey-Shack surface scatter theory, its implementation, and its viability for predicting scatter from random AR structured surfaces. A repository of data of various samples can be found in the Appendix, following similar routines to those discussed within the chapters.

CHAPTER 2: SPECTROPHOTOMETRIC CHARACTERIZATION

2.1: Introduction

Light incident at a refractive index transition boundary between materials with different refractive indices, results in a redistribution of transmitted and reflected energy, proportional to the square modulus of the corresponding Fresnel coefficients. Spectral transmission and reflection is characterized using spectrophotometers to assess material performance over wavelength bands of interest. For normal dispersion materials, the addition of random nanostructures can produce an antireflective effect through gradient "softening" of the index boundary.

Antireflective surface transmission enhancement is quantified through comparisons of spectral data for structured and polished substrates [10]. While transmission enhancement can be achieved by suppression of specular Fresnel reflection, the inverse argument does not hold. In cases where surface-induced scatter is evident, the on-axis spectral reflection and transmission can be reduced simultaneously. In those cases, the sum of the detected power along the propagation wavevector axis is lower than the total incident power; or, if the measurements are normalized to one of the measured quantities and extrapolated, the sum of the reflected and transmitted powers result in greater values than the incident normalization (i.e. greater than 100%). This is mainly due to the random surface nano-roughness transverse cross-sections, which scatters light non-specularly and distributes irradiance within solid angles much wider than optical quality polished substrates do.

2.2 Nanostructured Materials for IR Transmission Enhancement

Off-axis scatter was investigated using optical-quality Zinc Selenide (ZnSe) windows processed with antireflective structures and measured using spectrophotometry to gather data on their optical performance in the mid-wave and long-wave infrared (MWIR, LWIR). ZnSe is a typical material used in infrared optics due to its low absorption and high transmissivity (normal dispersion) over the infrared spectrum. The 25.4 mm-diameter round substrates had optical high-quality polish, with 7 nm average roughness, 9 nm rms-roughness, and a thickness of 3 mm. Random nanostructuring of the surfaces was achieved using the “thermodot" method described in brief below [13].

2.2.1: Structured Surface Fabrication

Substrates were coated with a thin, hard dielectric film (in this case AlN) at an empirically determined thickness, which is sufficient to mask the substrate from reactive-ion plasma etching radicals for the duration of the fabrication etch process. A thin layer of metal (Ni) is deposited on top of the dielectric film and is rapidly annealed to form nano-scale islands on the dielectric surface. Metallic island density is controlled by the rapid thermal annealing process schedule, and the surface energy between the metal and the dielectric and the island height depends on deposited metal-film thickness.

The dielectric film is etched completely from the metal-vacant areas in a reactive-ion plasma (RIE), resulting in transfer of the random island metal-footprint patterns in the AlN layer. The resulting random surface mask is then etched using a substrate-selective plasma, resulting in pillars with a “top-capped” profile. Thermodot Ni masking-caps were removed after the substrate etch step, using a commercially available wet chemical Ni-etchant solution. Residual AlN caps remain on the original substrate pillars. Pillar height is controlled by the total etch time, whereas chamber pressure and applied RF-power RIE parameters control the sidewalls of the pillars. Thermal process parameters vary dot footprint shape and diameter—with an averaged-diameter population distribution that is statistically repeatable. Scanning electron-microscope (SEM) images of four randomly nanostructured ZnSe surfaces are shown in Figure 2.1.

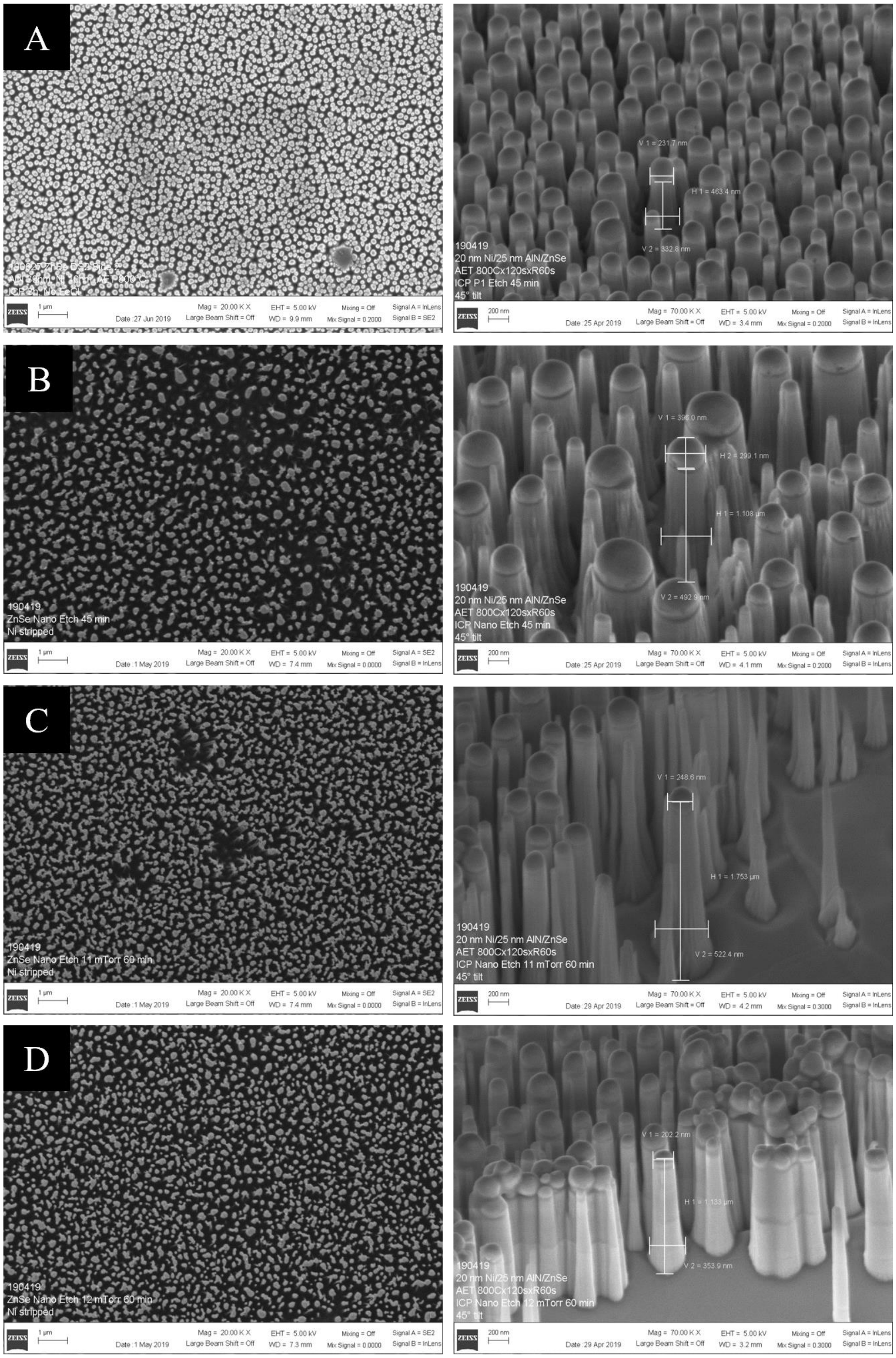

Figure 2.1. SEM images of four randomly nanostructured ZnSe surfaces (A-D), including top-down of the structured dielectric surface (left) and monolith features at 45° angle of viewing (right).

Table 2.1. Surface randomness averaged dimensions for nanostructured ZnSe samples.

	ZnSe:A	ZnSe:B	ZnSe:C	ZnSe:D
Diameter (nm)	214	233	175	174
Cell Size (nm)	487	457	360	368
Spacing (nm)	273	224	185	194
Height (nm)	653	1600	2500	1600
Density ratio	44%	51%	49%	47%
Aspect ratio	3.05	6.87	14.29	9.20

The pillar density ratio, calculated as the ratio of the average diameter to cell size, and their height-to-diameter aspect ratio, are comparative indicators of the random pattern density and effective depth. Pillar height is measured from the 45°-tilted, wide-field-of-view SEM images. For the representative sample group shown in this report, the pillar density varies from 44% (ZnSe:A) to 51% (ZnSe:B), and the aspect ratio from 3 (ZnSe:A) to 14 (ZnSe:C). Qualitatively we can describe the samples tested as ranging from shallow and sparse (ZnSe:A), to deep and dense (ZnSe:C).

2.2.2: Spectral Characterization

Spectral $T(\lambda)$ and $R(\lambda)$ were measured for all ZnSe substrates shown in Figure 2.1. The measurements were collected using a spectrophotometer (Bruker, Vertex-V80), across the MWIR and LWIR spectrum (2-12 µm), at normal incidence for $T(\lambda)$ and, at 15° AOI for $R(\lambda)$, sweeping AOC from 15° to 45° (Figure 2.2).

For unpolarized and incoherent light, specular reflectivity is not appreciably changing for angles between normal incidence and the substrate's Brewster angle value. This allows, to a good approximation, pairing the 15° AOI $R(\lambda)$ data with the normal-incidence $T(\lambda)$ measurements. The results of the specular reflection and axial transmission are shown in Figure. 2.3.

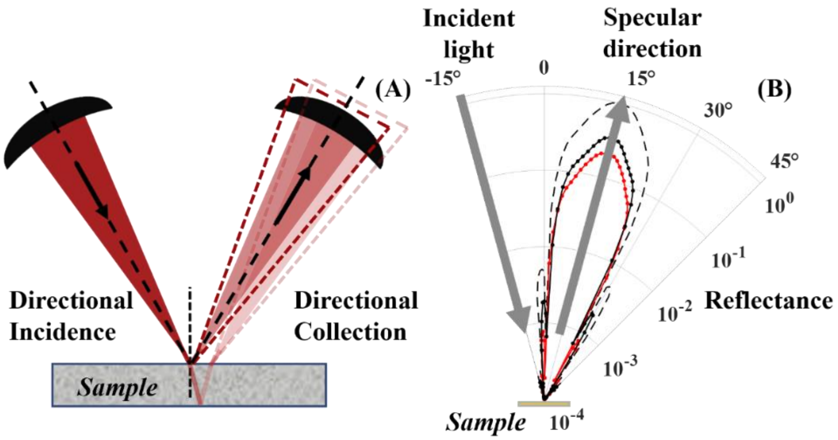

Figure 2.2. (A) Configuration of reflection measurement of the spectrophotometer used in this study. Light is focused onto the transparent sample plane and the reflected cone of light (red shaded area) is collected by rotationally scanning the collection mirror. Nano-roughened substrates may scatter light outside of the directional cone of collection (dotted outlined area). (B) Angular intensity distribution is presented as a directional diagram from -15° to 45° AOC, on a radial logarithmic normalized power scale. An aluminum mirror is used as a background (dashed line). Nano-roughened sample reflected intensity (red circles) is compared to the optically flat sample (black squares).

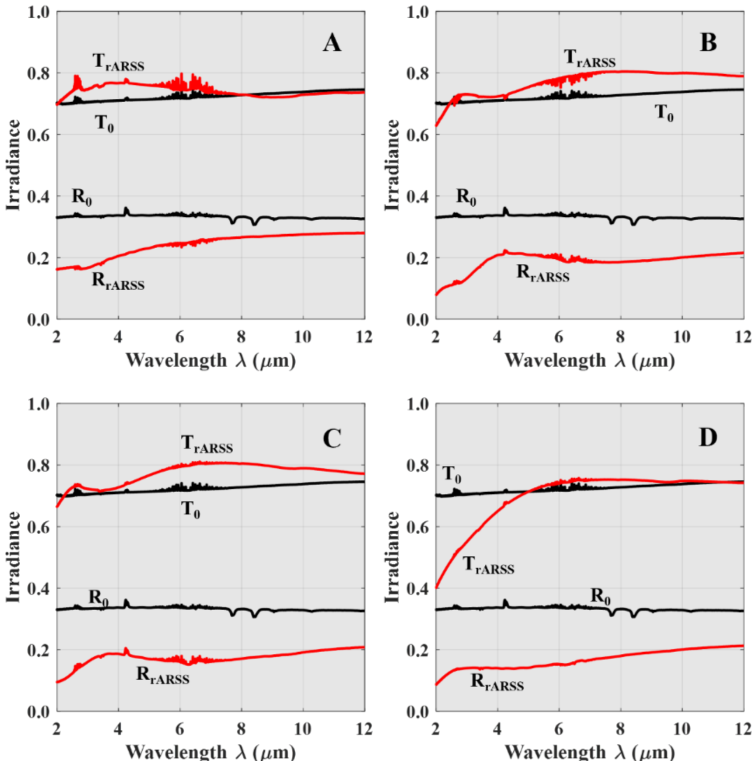

Figure 2.3. Measured normal incidence (axial) transmission ($T(\lambda)$) and specular reflection at 15° ($R(\lambda)$), for the single-surface rARSS processed samples(A-D) (red) and an optically flat ZnSe substrate (black).

Three of the four ZnSe nanostructured substrates, ZnSe:A, B and C, have axial transmission enhancement within the wavebands measured, due to the presence of the rARSS on a single facet. Transmission is enhanced by 7% for sample A at MWIR wavelengths, while Samples B and C have increased transmission (+10%) in the LWIR (8-12 µm). Sample D shows no improvement across the measured wavelength bands. While the measured spectra of samples B and C are similar, it is noted that the surface features of the two samples shown in Figure. 2.1, and the surface randomness scale descriptors in Table 2.1, are morphologically distinct. The most noticable difference between the two samples is their pillar aspect ratio, which is more than twice as large for sample ZnSe:C, whereas the pillar density ratio is more comparable between the two. The transverse-feature cell size is smaller for ZnSe:C compared to ZnSe:B, and almost identical to ZnSe:D. On the other hand, ZnSe:A and B have the same cell size and clearly different pillar aspect and density ratios.

2.2.3: Spectrophotometry Discussion

MWIR and LWIR measurements of spectral Transmittance ($T(\lambda)$) and Reflectance ($R(\lambda)$), are collected using spectrophotometers with temporally incoherent and unpolarized light sources (e.g., globars). Such instruments have much larger apertures than the wavelengths in the IR band, resulting in poor spatial coherence, in addition to their poor temporal coherence due to the thermal nature of their light-emission mechanisms. Because of low coherence, interference phenomena induced between surfaces of relatively thick ($> 500\lambda$) transparent substrates are not prominent. Additionally, spectrophotometers normalize their measurements using a “background spectrum” or baseline, which is taken differently for each type data set. In transmission, the background is collected as the irradiance through the system in the absence of the substrate to be tested. In reflection, the background irradiance of the system includes a reflective mirror, which is a single-surface optical component. Although this restriction is not significant for opaque substrates within the test bands, for transparent substrates there are multiple “front-to-back” reflections that contribute to the detected signal, and the normalization is not strictly comparable.

Spectrophotometric intensity measurements cannot distinguish between single-surface reflections and overlapping reflections from the front and back surface of a transparent substrate, especially when the two surfaces are not identical. Therefore, at off-normal-incidence reflection conditions, the “top” and “bottom” irradiance reflections will overlap and the measured angular intensity distribution will be greater than the “top” single-surface response alone. For nano-roughened substrates, the directional distribution of light from the front and back surface contribution will have additional scatter which is different than that of an optically flat sample. Due to the finite size of the movable collection mirror used in the setup, scattered light outside the directional collection cone (AOC) is not captured, as seen in the diagram of Figure 2.2.

2.3: Spectral Analysis of Bidirectional Scatter

The presence of nanostructures simultaneously increased the axial transmission throughput and reduced the specular reflection. At MWIR wavelengths (3-5 µm), summing the normalized transmission and reflection from the processed samples does not yield unity (100%), within our measurement’s degree of uncertainty (±0.5%), suggesting there is an additional mechanism that is removing light from the axial light-propagation direction.

Total integrated scatter (TIS) is a measure of all scattered intensity outside the region strictly defined by the light beam along the axial or specular direction. TIS can be useful for reducing large amounts of scattering data to a single comparative quantity, which defines the general scattering performance of optical interfaces. Due to the finite size of the spectrophotometer collection mirror, the specular region is taken as the cone of collection spanned by the mirror, defining a limited integrated scatter region.

When testing transparent windows, surface scatter propagates in both the reflection and transmission directions; therefore, the spectrometer's detector mirror collects integrated scatter data in transmission mode over the finite collection aperture as well. By combining the data of both the transmitted partial integrated scatter (contained in our normal incidence axial direction), as well as the integrated scatter cone of the specular reflection, bi-directional scatter (BDS) can be determined, to further distinguish between the scattering induced by the various roughened surfaces.

As mentioned, wide-angle scattered light escapes the spectrometer's cone-of-collection. To assess the magnitude of the scatter losses, both transmission and reflection spectra are needed. To calculate the BDS, due to a single nano-structured surface on a transparent substrate, the unprocessed sample's double-sided intensity measurements $T_{UDS}(\lambda)$ and $R_{UDS}(\lambda)$ are first summed to quantify the instrument's total measured irradiance reference. This value is used as a re-normalization:

$$T_{UDS}(\lambda) + R_{UDS}(\lambda) = I_U(\lambda) \tag{2.1}$$

In general, these quantities are normalized independently by the instrument, and may not add to unity (100%), as their respective "baseline" normalizations are different: in the $R_{UDS}(\lambda)$ case it is a front surface metal mirror, whereas in the $T_{UDS}(\lambda)$ case it is the unobstructed incident light beam. We assumed that the unprocessed substrates, having a high-quality optical polish, have no appreciable scatter within the dynamic range of the spectrophotometer's detector. Following Equation 2.1, the nano-structured surface sample's measurements $T_{PDS}(\lambda)$ and $R_{PDS}(\lambda)$ are summed, while also including a loss term $\Sigma_{PSS}(\lambda)$:

$$T_{PDS}(\lambda) + R_{PDS}(\lambda) + \Sigma_{PSS}(\lambda) = I_P(\lambda) + \Sigma_{PSS}(\lambda) = 1 \qquad (2.2)$$

where $\Sigma_{PSS}(\lambda)$ is the non-captured single surface BDS, and $I_P(\lambda)$ is the total irradiance measured by the instrument. Dividing Equation 2.2 by Equation 2.1 results in the net scattered irradiance ratio $\sigma_{PSS}(\lambda)$, which is normalized to the non-scattering, unprocessed substrate's total irradiance:

$$\sigma_{PSS}(\lambda) = 1 - \left({}^{I_P(\lambda)}\!/_{I_U(\lambda)}\right) \qquad (2.3)$$

Re-normalization of the processed window reflection and transmission, to the unprocessed sample values, eliminates the unprocessed back-surface intensity contributions, common to all tested substrates, and produces a value for the radiative BDS, depending only on the presence of the processed single-sided surface. If the sum from Equation 2.1 results in values near unity across the entire spectral range of measurements, then the single surface scatter $\Sigma_{PSS}(\lambda)$ in Equation 2.2 and the scattered irradiance ratio $\sigma_{PSS}(\lambda)$ from Equation 2.3 are going to be within the instrument's measurement uncertainty, and we can consider them equal. Proceeding with this assumption and re-arranging Equation 2.2, we can relate the processed samples $R_{PDS}(\lambda)$ to the unprocessed sample double-sided intensity measurements $R_{UDS}(\lambda)$ by a wavelength-dependent scaling factor $f(\lambda)$:

$$1 - \sigma_{PSS}(\lambda) - T_{PDS}(\lambda) \approx R_{PDS}(\lambda) = f(\lambda) \cdot R_{UDS}(\lambda) \qquad (2.4)$$

In this sense the processed scattering substrate is a "lossy" version of the double-sided polished substrate, with the losses attributed only to the single processed face. We note that $f(\lambda) < 1$, since the randomly nanostructured surface reflectance can only decrease along the specular direction, as the scattered power will distribute over a solid angle of 2π-sr. Because all scatter is due to the single nanostructured surface, the same scaling factor could apply to the processed single-side reflectance $R_{PSS}(\lambda)$ relating it to the unprocessed single side value $R_{USS}(\lambda)$:

$$R_{PSS}(\lambda) \approx f(\lambda) \cdot R_{USS}(\lambda) = f(\lambda)\left({R_{UDS}(\lambda)}\Big/{\left(2 - R_{UDS}(\lambda)\right)}\right) \tag{2.5}$$

The last step in Equation 2.5 is obtained by algebraic manipulation of the polished double-sided reflectance equation that relates the single side $T_{USS}(\lambda)$ and $R_{USS}(\lambda)$, to the double-sided quantity $R_{UDS}(\lambda)$ [33-34].

2.3.1: Single-surface Optical Scatter Results

Using the preceding estimations, total BDS, $\Sigma_{PSS}(\lambda)$, single-side reflectance, $R_{PSS}(\lambda)$, and single-side transmittance, $T_{PSS}(\lambda)$, was calculated and shown in Figure 2.4. For all samples, scatter is present for shorter wavelengths (MWIR), and decays exponentially as wavelengths increase (LWIR). Some qualitative comparisons are evident. The surface of sample A has fine and sparse nano-roughness, inducing almost uniform low scatter across the wavebands. Consequently, the transmittance of ZnSe:A is enhanced in the MWIR, and some scattering losses in the LWIR. In contrast, sample ZnSe:D, with larger and wider features, shows strong scattering in the MWIR, which affects its transmittance considerably.

The previous analysis assumed that the loss of light from the specular direction was due to nanostructures causing surface scatter. The conjecture appears to be true for these materials based on previous knowledge of traditional optical diffractors and diffuse topological surfaces. The question remains: if light were scattered from the specular region, how was it distributed in angular space?

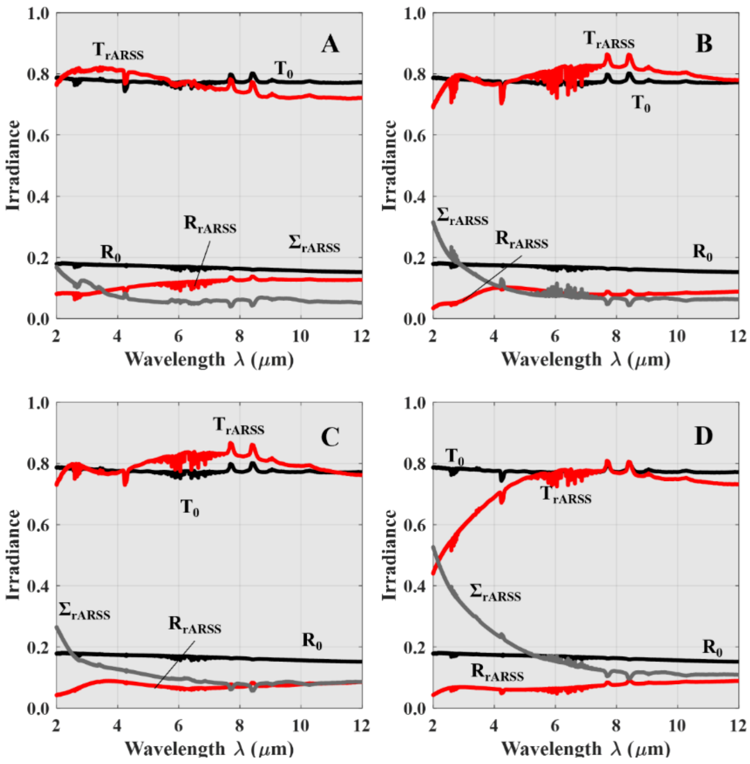

Figure 2.4. Calculated bi-directional scatter (Σ) (grey), single-surface reflectance (R), and single-surface transmittance (T) for each single surface processed ZnSe substrate (red), and the optically flat ZnSe window (black) using Equation 2.3-2.5. Light scatter from the optically flat substrate was negligible over the wavelength band of interest.

2.4: Measuring Wide-angle Reflected Scatter

The redistribution of light from the specular region is quantified by measuring wide-AOC intensities, and comparing the angular distribution of light from a processed substrate to the optically flat (unprocessed) substrate. During a reflection measurement, the incident beam is directed at the sample surface and reflected towards a movable collection mirror (Figure 2.2 right). The spectrophotometer collection mirror used in this study is limited to motion in the equatorial plane from 13° - 83° from the sample normal vector.

Depending on the optical system’s alignment, signature data associated with the background may exhibit biasing in one angular direction, causing an asymmetric pattern to form [20]. Verification of the spectrophotometer setup alignment was conducted by taking measurements at 25° and 30° AOI, sweeping AOC (15° - 60°) to determine the symmetry of the tool's signature intensity angular distribution. In those test cases, the clockwise and counterclockwise power distributions (with respect to specular reflection angle) were approximately equivalent, within the sensitivity of the instrument.

2.4.1: Directional Reflectance Results

Off-axis reflectance was measured as the collection mirror was swept from $\theta_c = 15°$ to 60°, keeping AOI fixed at 15°, and mirrored over the specular ray axis, to produce a complete directional view of the scattered light distribution. Polar representation of scattering data is useful to visualize the directionality of light within an optical system. Logarithmic-scale intensity distinguishes between the reflectivity of the main and side lobes of the directional diagrams, which can have four or more orders of magnitude difference. Directional diagrams of reflectance distributions at 4 µm and 10 µm are presented in Figures 2.5-2.6. The wavelengths shown were chosen as representative cases of scatter in the MWIR (4 µm) and LWIR (10 µm).

The angle of collection (θ_c) can be scaled in a semi-logarithmic format, similar to conventional scattering formatting used by Harvey [20, 25, 34-35]. Using the parameter $\beta = \sin(\theta_c)$, scattering data can be compared over multiple AOI for wide AOC, due to the shift invariance of radiometric radiance. The reflectance ratio presented here may not be considered radiance in a strict mathematical sense; however, plotting as a function of β allows for efficient examination of the axial, narrow, and wide-angle scatter distribution,

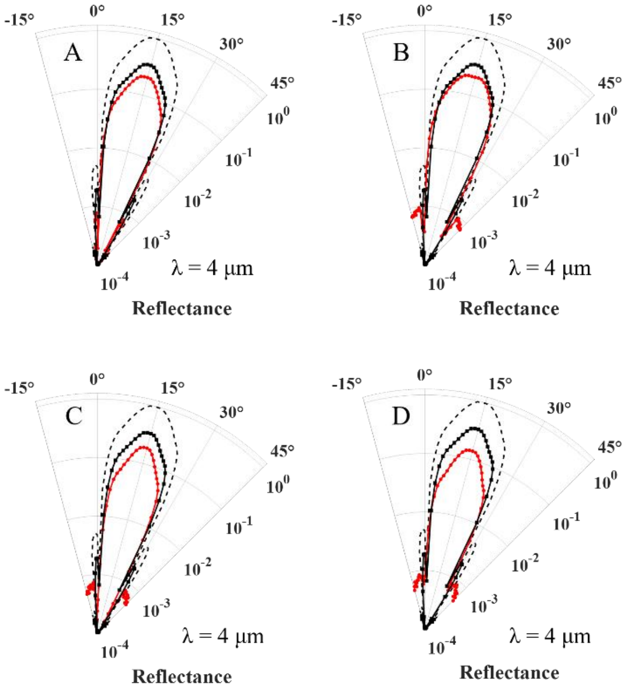

Figure 2.5. Measured reflected directional intensity distributions at 4 μm wavelength, including scattered light outside of the directional cone (+3°< θ_c <+27°). The processed ZnSe surface (red circles) is compared to its unprocessed counterpart (black squares) and the mirror signature (dashed line).

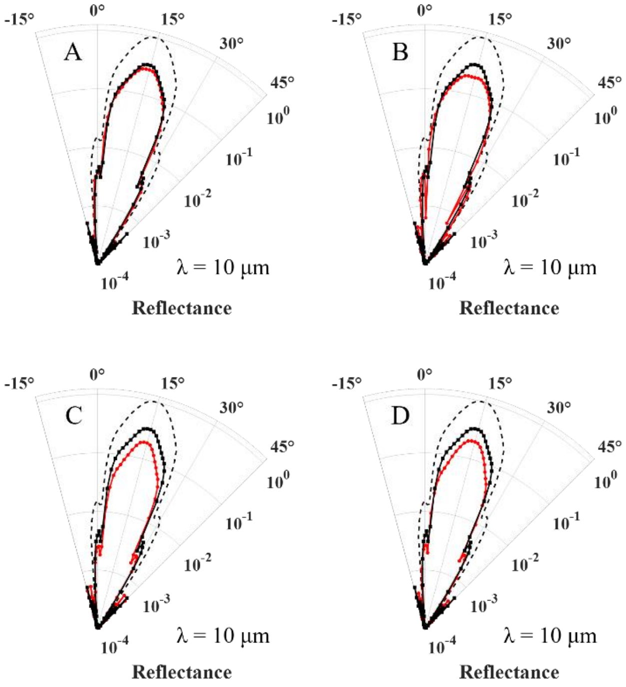

Figure 2.6. Measured reflected directional intensity distributions at 10 μm wavelength, including scattered light outside of the directional cone (+3°< θ_c <+27°). The processed ZnSesurface (red circles) is compared to its unprocessed counterpart (black squares) and the mirror signature (dashed line).

compared to the polar representation which can obfuscate wide-angle (>±15° from specular) low-intensity data near the polar origin (Figure 2.7-2.8).

Main and side lobes of the unprocessed sample measured scattering distribution are proportional to the measurement mirror performance (background), with a uniformly-reduced magnitude due to the lower Fresnel reflectivity of ZnSe. Scaled conformity of the angular reflectance distribution signifies that scatter due to the presence of particulate contamination is minimal for the optically flat window. Mirror and unprocessed sample main lobe angular extent remains constant for $0.26 < \beta < 0.45$ ($15° < \theta_c < 27° \pm 0.5°$) over the measured wavelength band, while side lobe intensity increases proportionally with wavelength, and its angular extent does not change appreciably (7° ± 0.5°).

Samples A, B, and D all exhibit broadening of the main lobe angular extent. Side lobes for samples B, C, and D are suppressed at 4.0 µm wavelength, and wide-angle scatter is an order of magnitude larger than the optically flat substrate. At 10 µm wavelength, sample B main lobe angular extent is broadened. Sample A performance matches the optically flat substrate in magnitude and shape, and samples B, C, and D have reduced main and side lobe values, while maintaining the general shape of the signature of the mirror.

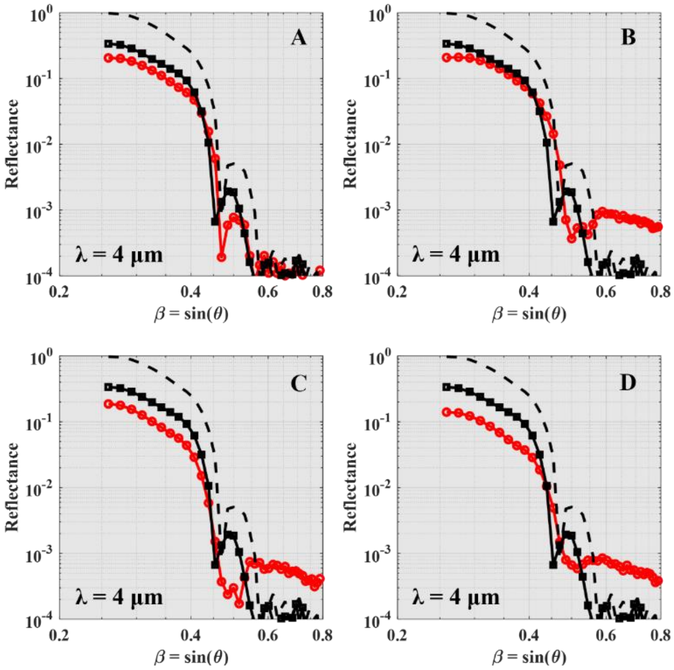

Figure 2.7. Measured reflected angular intensity distribution at 4.0 µm wavelength, from the rARSS substrates (red circles), the unprocessed ZnSe window (black squares), and the reference mirror (dashed line), presented as logarithmic reflectance functions of parameter $\beta = \sin(\theta_c)$.

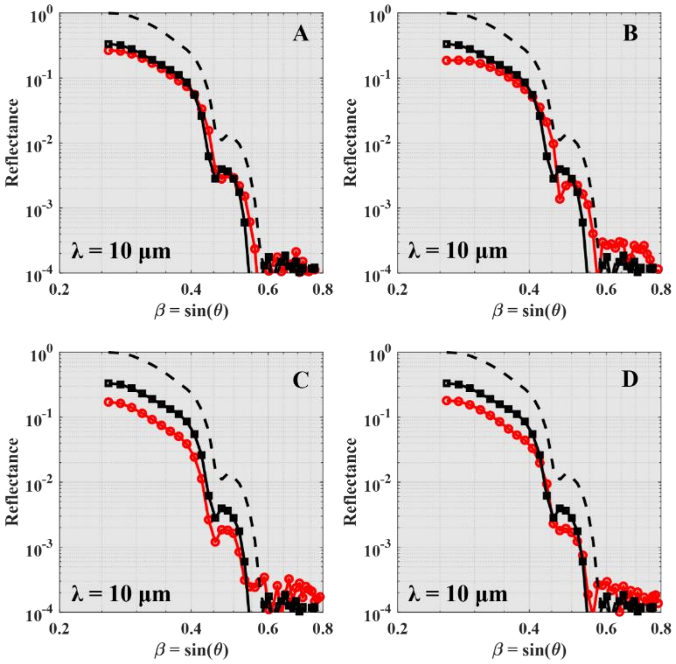

Figure 2.8. Measured reflected angular intensity distribution at 10 µm wavelength, from the rARSS substrates (red circles), the unprocessed ZnSe window (black squares), and the reference mirror (dashed line), presented as logarithmic reflectance functions of parameter $\beta = \sin(\theta_c)$.

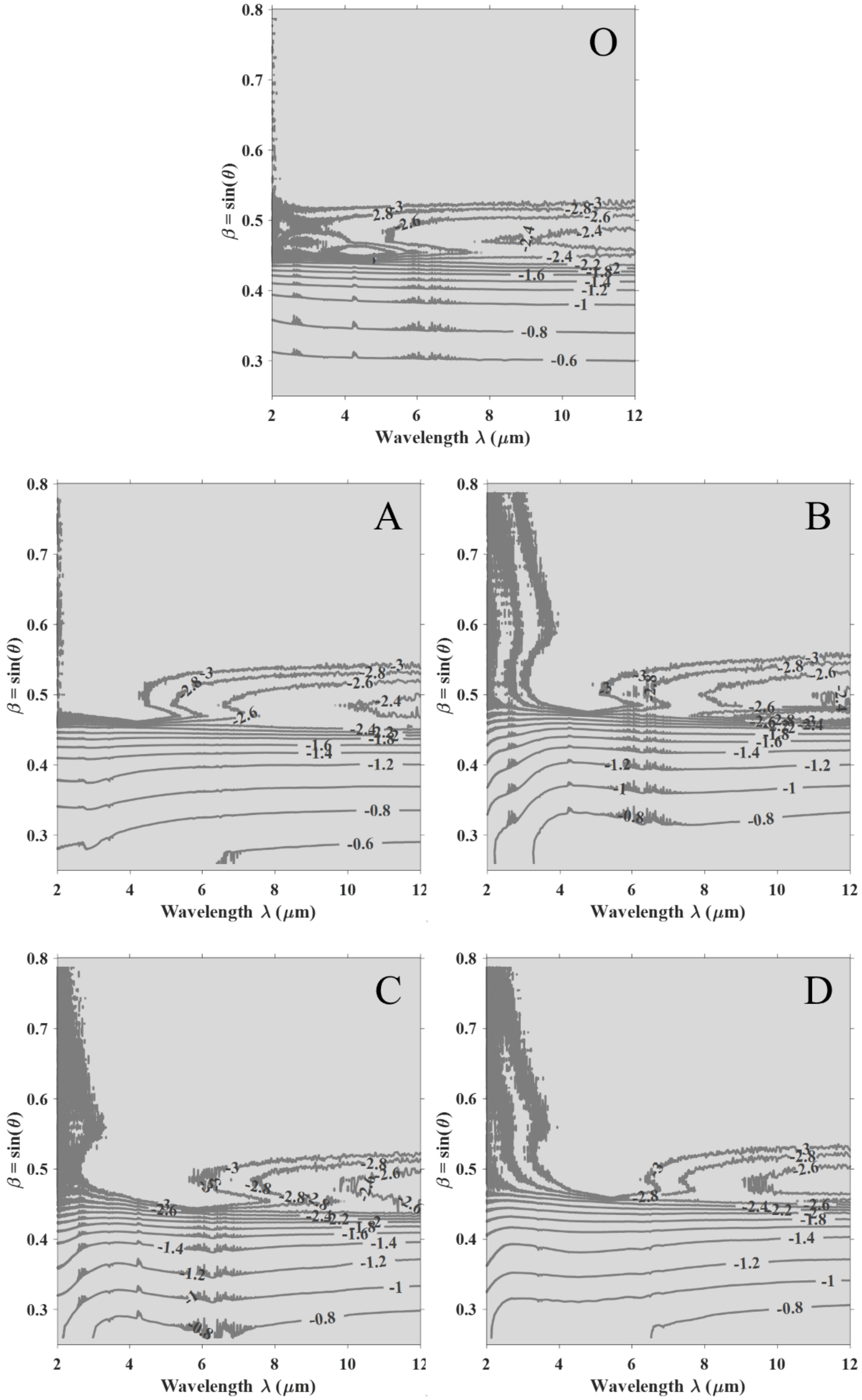

Figure 2.9. Processed samples (ZnSe:A–D) are characterized by comparing their reflectance distribution contour gradients to that of the optically flat sample (ZnSe:O).

Processed samples (ZnSe:A–D) are characterized by comparing their reflectance distribution contour gradients to that of the optically flat sample (ZnSe:O) (Figure 2.9). The spectral radiance maps show noticeable differences in performance for each sample at shorter wavelengths (2.0 to 5.0 μm) for all AOCs. Sample ZnSe:A exhibits a side-lobe reduced magnitude while samples B, C, and D all have a homogenization of the scatter distribution outside of the main lobe ($\beta>0.45$). Main lobes of all samples measured decrease as the angular extent widens and the $\beta=0.45$ boundary diffuses. For samples B, C, and D, scatter at higher angles in the MWIR is an order of magnitude larger than samples O and A. Longer wavelength measurements (5.0 to 12 μm) of all samples resemble the optically flat sample with reduced magnitude values. Contrast between main and side lobes of processed samples diminishes for samples A, C, and D, whereas sample B has a clearly defined separation between lobes at longer wavelengths.

2.5: Discussion of Spectral Results

Collected radiance distribution characteristic shape is due to the angular dependence of the reflected area-solid angle product $dA_s d\Omega_s$. Due to the elongation of the incident beam finite cross-section in one direction $dA_s /\cos\theta_i$, the signature of the tool (single surface mirror) appears to be similar to a directional but diffuse dipole radiator. For transparent substrates, the double reflection will extend the apparent radiator length, due to overlapping front-to-back reflected elliptical spots, accentuating the radiator's characteristic shape.

Globar IR-sources generally emit as blackbodies; therefore, uncertainty in the spectrophotometer normalization occurs when the background and measured data approaches three orders of magnitude difference, at longer wavelengths and large angles of collection. This agrees with the elevated “noise” on our LWIR band measurements for $\beta > 0.55$, compared to the MWIR measurements.

Comparison of relative scattering trends between samples is important, in the context of rationalizing the performance of an optical window due to the presence of roughness. Figures 2.5-2.8 show that a surface with shallow and sparse nano-roughness (ZnSe:A) has better MWIR anti-reflective performance than a shallow and dense surface (ZnSe:B), although the measured specular reflectance is lower for B compared to A (Figure 2.3).

For similar nano-roughness packing density, shallow (ZnSe:B) to deeper features (ZnSe:C) is not mitigating the MWIR wide-angle scatter losses. In the LWIR, nano-roughness heights do not provide higher transmission enhancement like other gradiant phase effects. ZnSe:D and ZnSe:B have average feature depth of the order of 0.1λ and ZnSe:C is deeper at 0.25λ, yet B and C have very similar spectral responses strictly on-axis (Figure. 2.3). ZnSe:B and ZnSe:C have almost identical nanostructure density, although their depths are dissimilar, seems to control the specular reflectance suppression. Given specular reflectivity and random surface depth measurements only, the results indicate that the axial transmission of random AR nano-surfaces cannot be accurately determined.

2.6: Conclusions

Chapter 2 focused on the characterization of nanostructured surfaces using spectrophotometry. This method quantified the performance of randomly nanostructured AR surfaces on optical windows, using single-sided-surface directional scatter reflectance and transmission measurements, removing normalization inconsistencies from measurements limited to nanostructured surface specular reflection alone.

The analysis determines the surface-induced Fresnel reflectivity reduction, including additional bidirectional scatter, by leveraging axial transmission and specular reflection measurements, of both the nanostructured surface and the optically flat equivalent material substrate, to remove the “backside” contribution of the transparent substrate and accurately determine the scatter due to the nano-structured surface alone. Structured surfaces presented had measurable specular losses due to scatter in the MWIR while also enhancing the axial transmission throughput of the material.

Addition of surface nano-scale features on an optical surface provides suppression of Fresnel reflectivity in, and at narrow-angle to, the specular direction, and measurable off-axis redistribution of light into the wide-angle region. As the wavelength of light increases compared to the size of the surface features, the suppression of the directional radiation is less prominent, while the side lobes maintain comparable values to the optically flat substrate. This trend is evident when examining the magnitude of scattering at single wavelengths or angles of collection; however, this does not uniformly scale with light scatter from short to long wavelengths. We show these results, presenting reflectance measurements as a function of the directional parameter β and the incident wavelength, for a selected set of sample surfaces.

Suppression of the specular direction intensity does not imply an absolute enhancement of axial transmission through a nano-structured window; rather, an increase on the main- and side-lobe directional irradiance and angular spread is observed. MWIR scattering reflection distributions show an increase in specular scatter for all processed samples (Figure 2.5). In the LWIR, processed sample scattering distributions are closer to the values expected from an optically flat sample, with some reduction in the main and side lobe magnitudes. Wide-angle scatter (> ±20° from specular) is reduced to our measuring tool’s noise level, signifying the feature sizes are too small to cause diffractive effects.

Measurements of the reflected angular intensity distribution of each processed substrate show the redistribution of light outside the specular direction, aligning with expectations based on the calculated bi-directional scatter (Figure 2.3). In the MWIR and LWIR, Fresnel reflectivity is shown to be suppressed in the specular region, because light is redistributed from that specular region. As the wavelength of incident light increases, the effects of scattering are less pronounced, yet measurable in the narrow axial direction regime. Further quantitative measurements of the distribution of scattered energy may give insight into structured surface diffractive effects and is explored in Chapter 3: Scatterometry.

CHAPTER 3: SCATTEROMETRY

3.1 Introduction

Chapter 2 focused on the specular (paraxial) performance of nanostructured optics. The goal was to quantify spectral transmission enhancement and reflection suppression, by direct measurements. In some cases, the axial transmission enhancement did not coincide with an equal suppression of the specular reflection, indicating that light was redistributed from the paraxial region to wider angles. By measuring the off-specular reflection, we were able to qualitatively discern differences between scatter caused by optically flat or nanostructured surfaces over the MWIR to LWIR. Due to restrictions in the reflection test setup, namely the solid angle extent and angular resolution of the collection mirror (described in Figure 2.2), it is difficult to resolve finer details in the distribution of scatter. This "convolution problem" causes blurring of high-resolution angular scatter features by oversampling the angular distribution with a large aperture as the collection aperture scans across the measurement plane.

3.2: Scatterometry Methodology

To better evaluate non-paraxial scatter and resolve high resolution features of the scatter distribution, a fixed incidence angle setup with high angular resolution and wide-angle detection was utilized. The CASI ("Complete Angle Scatter Instrument", Scatterworks Inc., Tucson, AZ) consists of a polarized-laser source, six degrees-of-freedom sample stage, and rotating detector arm, capable of 360 degrees angle of collection radiance detection over the equatorial plane (Figure 3.1). CASI has variable apertures and electronic gain-switching for enhanced sensitivity, making it able to distinguish finely detailed scatter distributions at large AOC.

To calibrate the instrument, light from the source is directed through the optic axis of the system, passing through a beam chopper, coarse and fine spatial filters, and a polarizer, into a focusing mirror directed towards the detector plane. The mirror and detector are adjusted until the resulting measured scatter distribution (without sample) is symmetric. In the process, the total power of the incident beam is recorded and stored for later use in converting the measured intensity to a bidirectional scattering distribution function (BSDF). CASI has two inaccessible angular ranges (Figure 3.1 right, blue shaded regions), due to obstruction from the sample holder and the detector arm as it sweeps across the hemisphere, blocking the source.

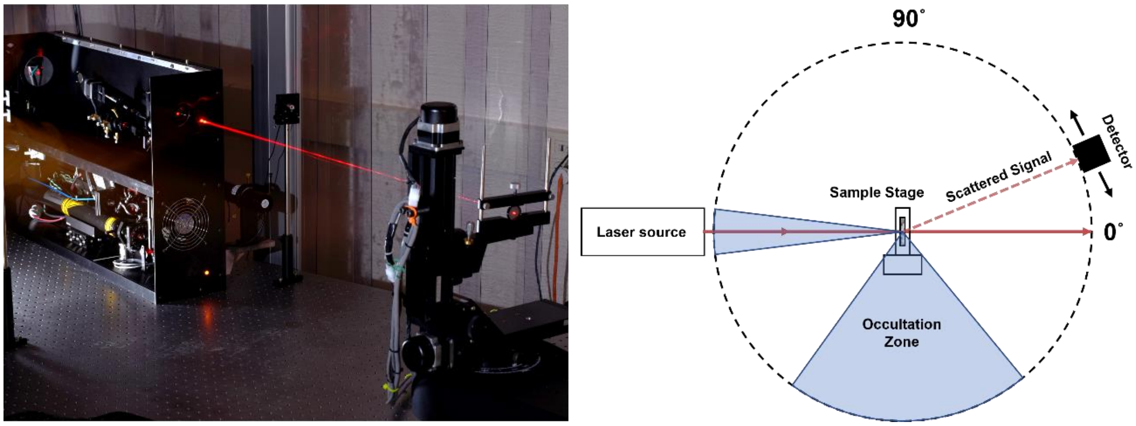

Figure 3.1. (Left) Photograph of CASI scatterometer setup with visible HeNe laser source. The sample is visible on the right edge of the photograph; the detector arm is beyond the image. (Right) Diagram of the CASI scatterometer layout. A laser source is directed towards the sample located at the center of rotation of the setup, with detector capable of measuring radiance over the equatorial plane of the unit sphere. The detector aperture size is adjusted for specific angular ranges as the detector scans across the hemisphere.

Using the CASI we can measure the *BSDF*, defined as the scattered radiance (*L*) per incident irradiance (*E*):

$$BSDF(\theta_i, \phi_i, \theta_s, \phi_s) = \frac{L(\theta_i, \phi_i, \theta_s, \phi_s)}{E(\theta_i, \phi_i)} = \frac{\Delta P(\theta_s, \phi_s)/(\Delta\omega \Delta A cos\theta_s)}{P_0(\theta_i, \phi_i)/\Delta A} \tag{3.1}$$

where θ_i, φ_i, θ_s, φ_s, define the incident (*i*) and scattering (*s*) polar (θ) and azimuthal (φ) angles, ω is the solid angle of the detector aperture, and ΔA is the area element of the illuminated scattering surface. *ΔP* denotes the radiant power collected by the detector while P_0 is the incident radiant power illuminating the area element [20]. Scatterometry trades the wavelength selectivity of spectrophotometry for optical sensitivity. Measurements give empirical data for single-wavelength angular spread (distribution) and the amount of light scattered after incidence at a surface, both in reflection and transmission.

FS substrates were measured via 405 nm UV confocal imaging microscopy (LEXT 5000, Olympus, Shinjuku City, Tokyo, Japan) at 100x magnification, and surface roughness parameters were obtained by analyzing the surface using the accompanying software. Figure 3.2 includes images of the substrates used in this study: 20-10 scratch-dig, optical-quality double-sided polished FS wafer (polished), a similar optical-quality unpolished (ground) FS sample, a random nanostructured FS (rARSS).

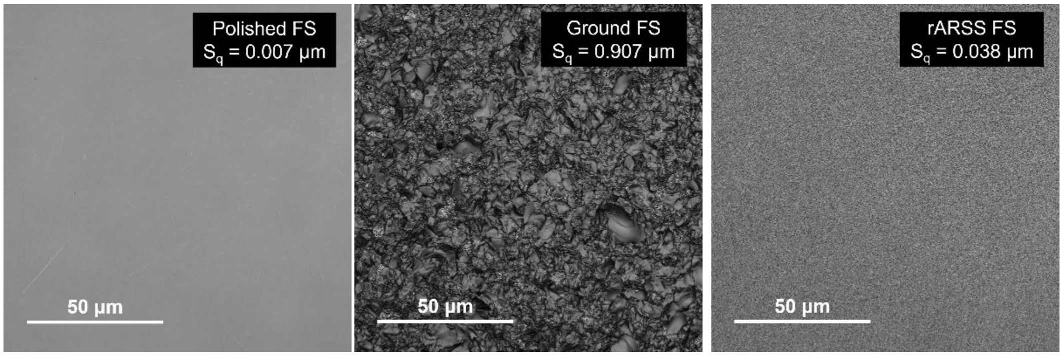

Figure 3.2. FS substrates of different roughness scales were measured using confocal microscopy taken with 405 nm UV laser illumination. (Left to right): optical quality FS flat, ground FS, and rARSS added FS surfaces. Samples with nanostructures were processed using random gold masking and etch method explained in Chapter 1. Statistical distributions of surface features (lateral spacing and depth of features) conventionally determine the spectral response of the interface.

3.2.1: Diffuse Scatter Measurements

For a micro-scattering surface (i.e., ground FS glass at visible wavelengths), we can explore the methodology of measuring optical scatter. Bidirectional transmission distribution function (BTDF) was measured for a ground FS substrate using a CASI scatterometer, with a vertically polarized, 633 nm wavelength, HeNe laser at 0°, 15°, 25°, 30° 45°, 56°, and 70° AOI, sweeping AOC from -90° to +90° around the specular direction. After the sample is placed and its area vector is parallel and centered to the instrument's optic axis, the detector sweeps across the hemisphere, and the accompanying software package numerically processes the BTDF. Measured scatter distributions at selected AOI are presented in Figure 3.3.

At first glance, scatter data gives the observer an idea of where and the amount of light is scattered into the hemisphere. Formalisms used in the literature can elucidate finer details of the surface scatter behavior. BTDF is proportional to radiant intensity (*I*) by multiplication with a cosine term. This satisfies the physical requirement that a null should be present at the perpendicular AOC due to angular dependence (Figure 3.4).

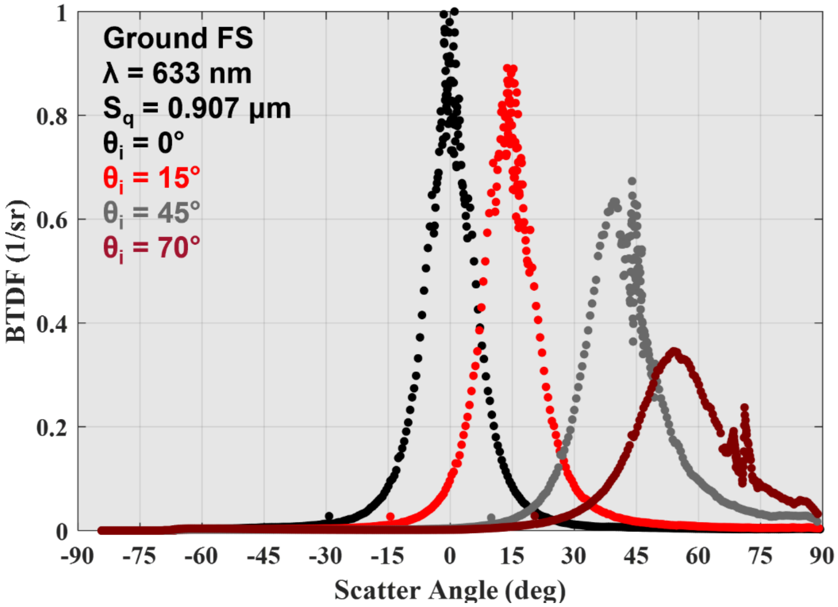

Figure 3.3. Measured BTDF of ground glass obtained using the CASI.

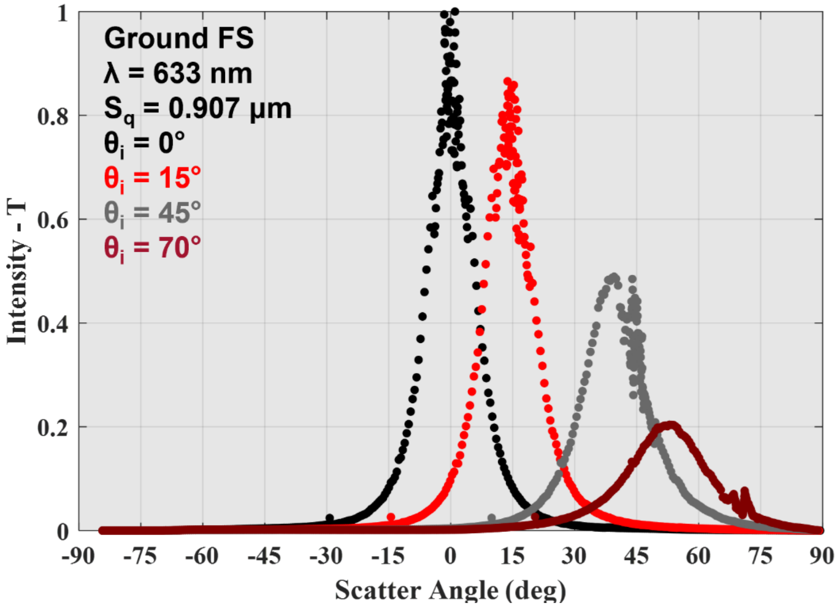

Figure 3.4. Scaling BTDF by cosine of the scatter angle produces a radiant intensity distribution. Due to the cosine dependence, the distribution approaches zero at large (>85°) angles of collection.

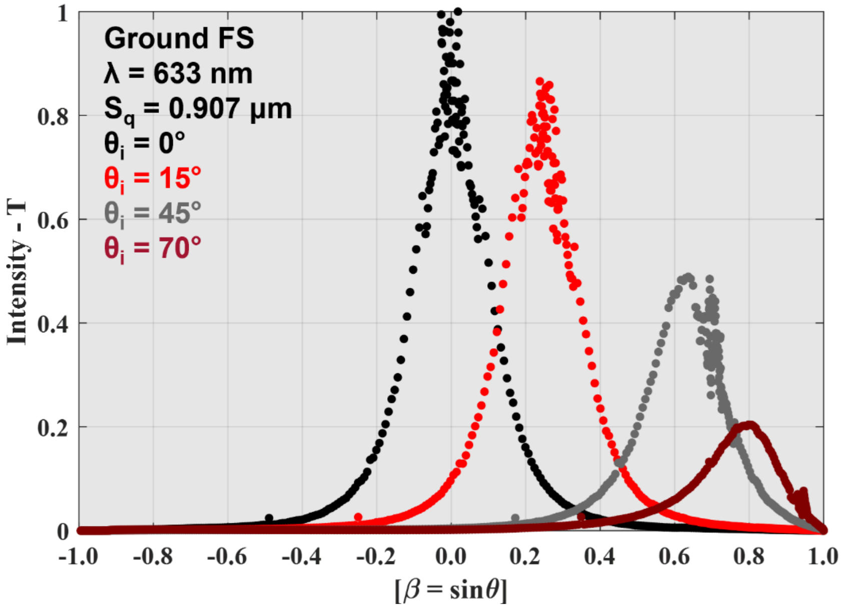

Figure 3.5. Beta-projection intensity. Scatter distribution is projected into cosine space by taking the sine of the collection angle ($\beta = \sin\theta_s$).

The sine of the collection angle ($\beta = \sin\theta_s$) projects the scatter distribution onto the unit circle in cosine space, for convenient viewing of diffracted light (Figure 3.5). This beta-projection enhances the view of near specular scatter where many fine-details generally preside, while wide angle effects that are uniform (in the case of highly diffuse surfaces) and less distinct comparatively [20].

Scatter distributions are dependent on radiometric radiance (*L*), therefore they are shift-invariant with respect to AOI. Plotting the intensity as a function of β-β_0 allows for efficient comparison of the scatter response due to high spatial frequency effects as AOI increases. For experimental scatter measurements of diffuse glass, scattered intensity peak shifts from the axial direction (propagation wavevector direction), as the angle of incidence increases (Figure 3.6).

Shifting the distribution by the angle of BTDF peak value (θ_p) verifies shift-invariance of the diffuse portion the scatter distribution. independent of incidence angle (Figure 3.7). The peak value of the BTDF diminishes with increasing AOI, and the location of the peak is shifted towards the surface normal facing the detector hemisphere (antiparallel to the incident light propagation vector).

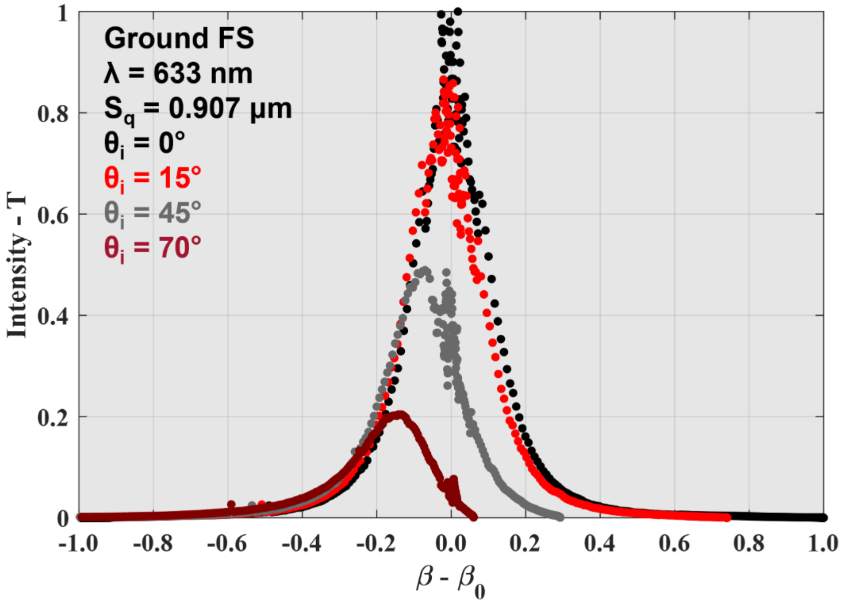

Figure 3.6. Near shift-invariance of the scatter distributions is visualized using shifted coordinates (β-β_0) based on the incidence (β_0 = sinθ_i) and collection (β = sinθ_s) angles.

Full width at half max (FWHM) of the distribution can be readily compared by removing fluctuations around the specular region due to the system signature (±5°). Values of the diffuse region angular FWHM are listed in Table 3.1. All distributions have similar FWHM values, with an average width of 17.6° ± 2.0°.

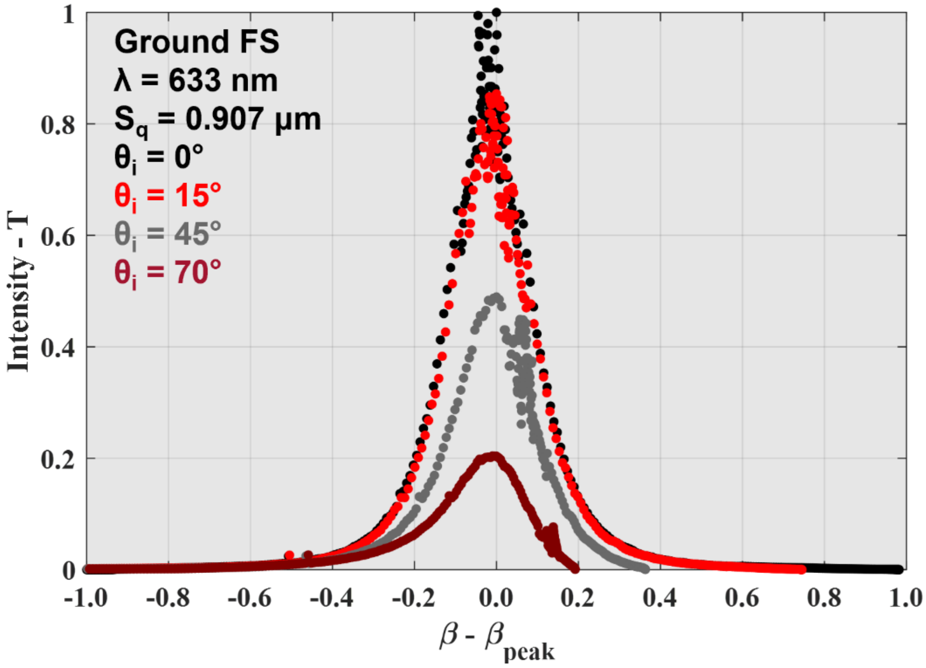

Figure 3.7. Shift of the distribution, by the BTDF peak value per AOI, shows the light transverse profile FWHM to be similar in value. The distributions have an average width of 17.6° ± 2.0°.

Table 3.1. Angular shift of the maximum BSDF value and angular FWHM of measured scatter distributions.

AOI (°)	AOC Peak (°)	FWHM (°)
0°	1.03	15.2
15°	14.78	14.8
25°	25.44	19.6
30°	29.19	18.5
45°	39.54	17.2
56°	47.19	19.1
70°	53.88	19.1

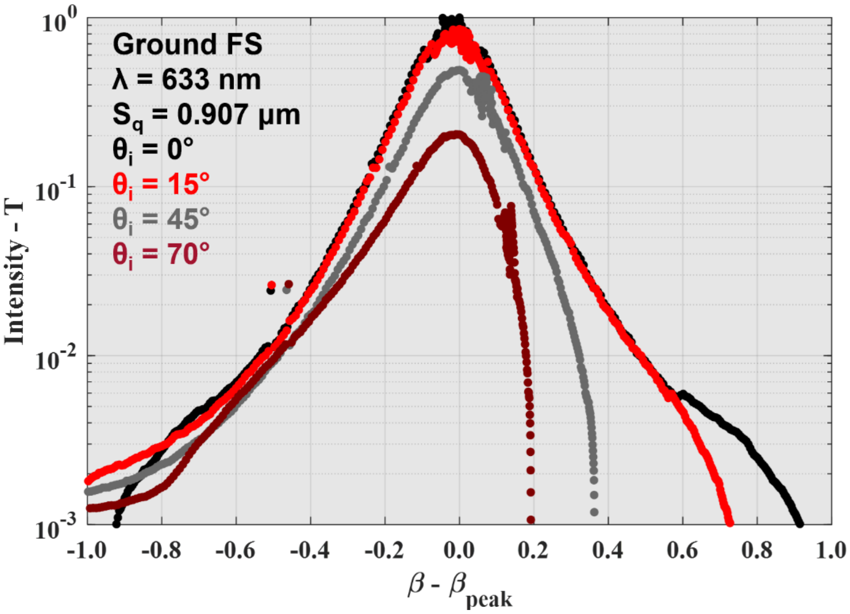

Figure 3.8. Logarithmic scaling of the diffuse scatter distribution reveals the wide-angle scatter is non-negligible.

Most authors plot the BSDF as a log-scale on the ordinate, since one can better distinguish between the paraxial radiation main lobe and side lobe “shoulders” of the BSDF, which can have nine or more orders of magnitude difference in scale. Random diffuse surfaces are generally (and conventionally) described by Gaussian-distribution statistics. Plotting measured transverse light-scatter from these surfaces in a linear scale shows similarity to Gaussian-profile distributions; however, logarithmic scaling of the measured distribution reveals it is not exactly Gaussian. The wings of the scatter distribution, while minimal, are not negligible (Figure 3.8).

This data agrees well with that shown in the literature and has been compared to empirical fits from other groups studying scatter (Figure 3.9). Harvey reports the scatter from diffuse ground surfaces to follow the following trend for the peak BSDF value per incident angle:

$$\theta_p = -6.0 * 10^{-5}\theta_i^3 + 2.4 * 10^{-3}\theta_i^2 + 0.8692\theta_i + 0.2999 \tag{3.2}$$

and the experimental BTDF at normal incidence:

$$BTDF = \gamma_0 K \left[0.7632e^{-\left(\frac{\pi(\beta-\beta_0)}{0.26724}\right)^2} + 0.2368e^{-\left(\frac{\pi(\beta-\beta_0)}{0.61566}\right)^2}\right] \tag{3.3}$$

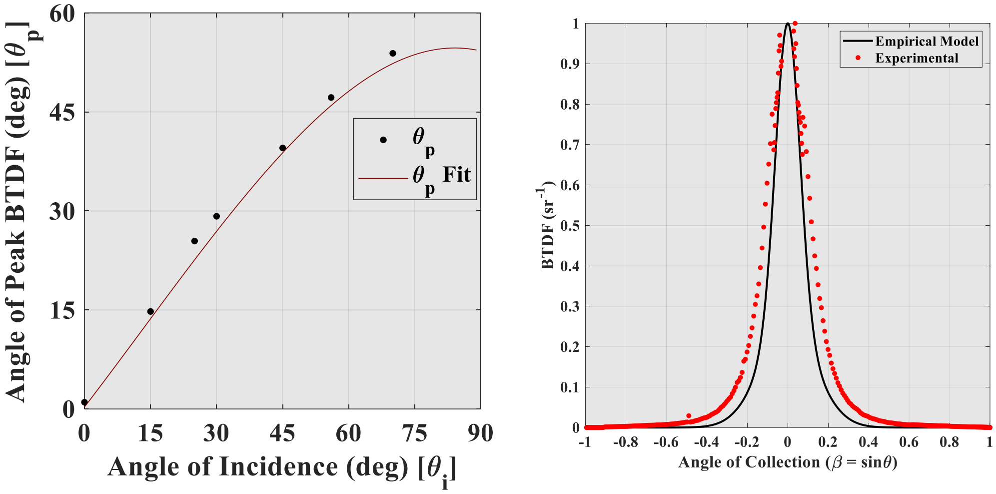

Figure 3.9. Curve fit of the BSDF peak value vs. AOI (left). Fitted BSDF distribution at normal incidence calculated using empirical fit from the literature (right) [20].

Differences in our measured data and the empirical fit from Harvey are due to us measuring samples with slightly different surface roughness characteristics.

3.2.2: Nanostructured Surface Scatter in the Visible

Following the assessment of the tool alignment and scatter conventions using ground glass diffusers, we measured scatter from nanostructured substrates for comparison to their optically flat counterparts.

The optical quality double-sided polished fused silica (FS) substrates were processed with random anti-reflective nanostructures for enhanced transmission over the visible wavelength band. Random nanostructuring of the surfaces was achieved using a random gold-masking method described in Chapter 1 [10].

The first part of the study measured BSDF with a vertically polarized, 633 nm, HeNe laser at 0, 15°, and 50° angle of incidence (AOI), sweeping angle of collection (AOC) from

-90° to +90° around the azimuthal direction. For transmissive scatter the nanostructured sample is compared to scatter from a polished FS substrate, while reflection data is also compared to conventional (Au and dielectric) optical mirrors. Sample spectra over the visible wavelength band are presented alongside scatter data for visualization of axial performance of the nanostructured sample (Figure 3.10 top).

We observed that at normal and 15° AOI, BTDF is bounded along the paraxial region between ±0.1°, while wide-angle scatter has increased for all rough samples (Figure 3.10 middle). Applying a change of coordinates to directional cosine space and plotting the BTDF as a function of shifted angle (β-β_0), the paraxial region between samples can be contrasted (Figure 3.10 bottom). It is noted that the error in the BTDF distributions at non-normal incidence is due to a reflected spot from the detector.

Similarly, bidirectional reflection distribution function (BRDF) was measured for mechanically roughened samples and compared to commercially available mirrors (Figure 3.11). Data was collected at 15° AOI, due to occultation of the specular region by the detector at normal incidence, and converted to radiant intensity, through multiplication of the scatter distribution with the sample’s projected illumination area. Wide-angle scatter of the rough samples is increased by three orders of magnitude, compared to the optically flat substrate, six orders compared to the polished mirrors, and two orders in the paraxial region. For the rARSS samples, the reflected specular peak was suppressed by 50% compared to their optically flat counterpart.

Optical interfaces with surface features on the order of the probing wavelength dimension will diffract light as it passes though the surface, diffusing it into a wider solid angle than an optically flat sample. When both surfaces are roughened, light scatters from the front surface, then scatters a second time at the back surface. To confirm this, we compared single- and double-sided processed nano-roughened samples (Figure 3.12).

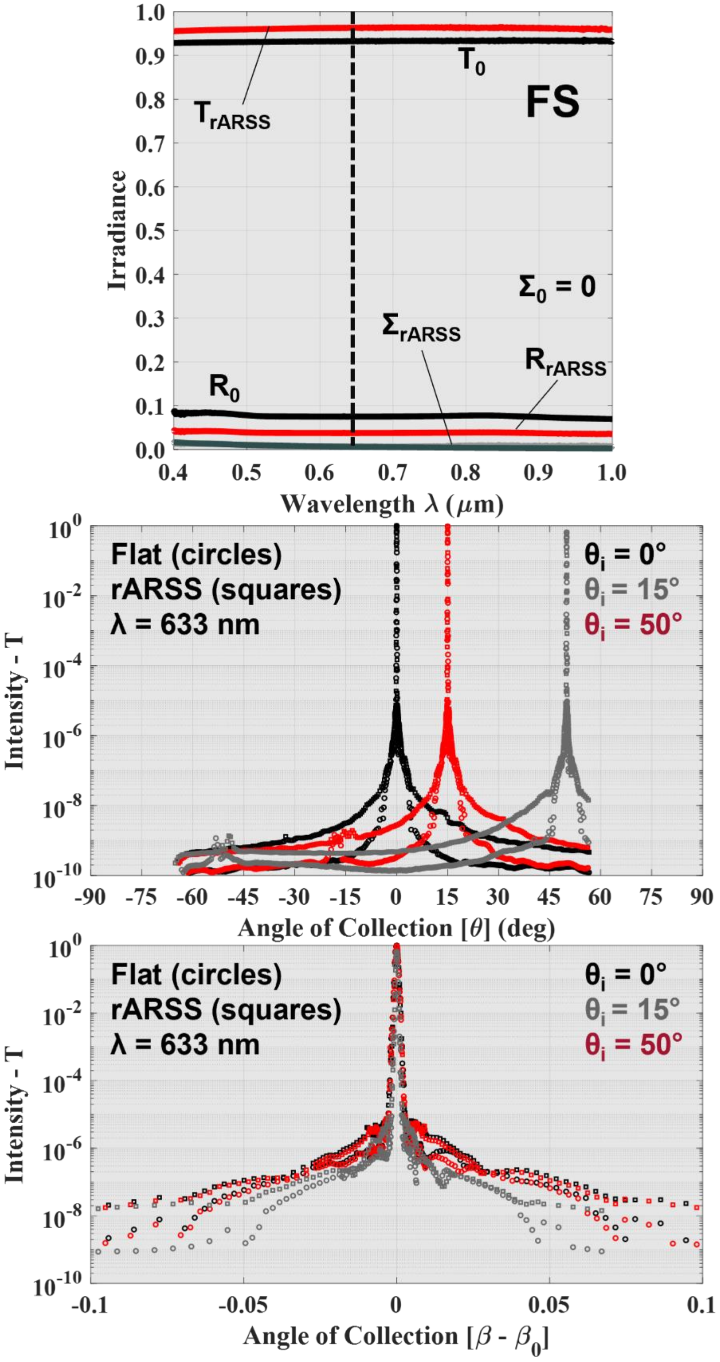

Figure 3.10. Single rARSS sample has an enhancement of 3.5% at the scatter wavelength of interest (top). BTDF of the rARSS sample (solid line) compared to an optical flat (points) at normal, 15°, and 50° AOI. rARSS sample has enhanced trasnmission and narrow paraxial scatter, compared to the polished surface, but with increased wide angle scatter (middle). Limiting the abscissa and converting the collection angle to shifted-beta shows the shift-invariance of measured scatter (bottom).

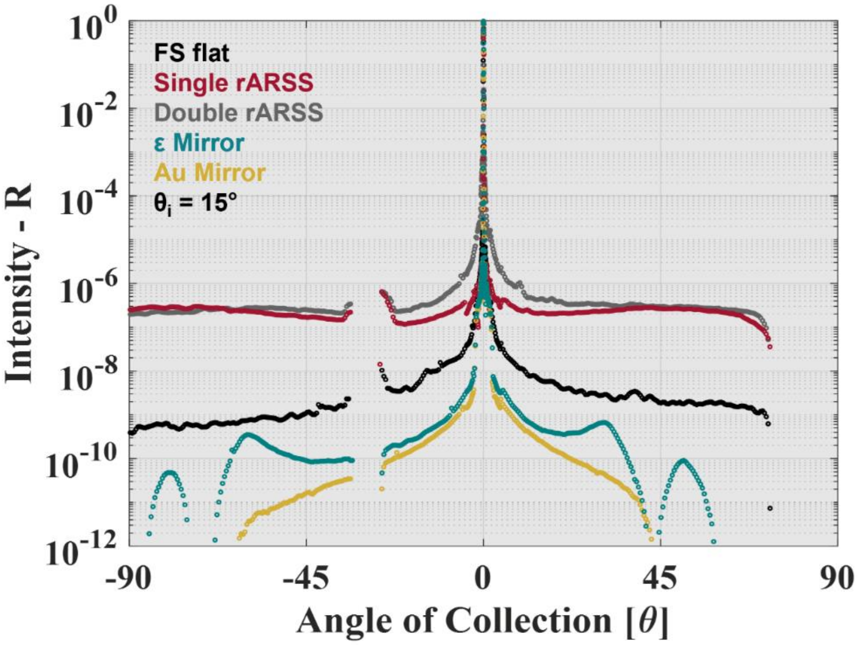

Figure 3.11. BRDF of selected rARSS samples compared to optical flat, gold mirror, and dielectric mirror. Compared to the optical flat, the rARSS wide angle scatter is increased by three orders of magnitude, while it has increased by two orders of magnitude in the paraxial region. For the rARSS samples, the specular peak was suppressed by 50% compared to their optically flat counterpart.

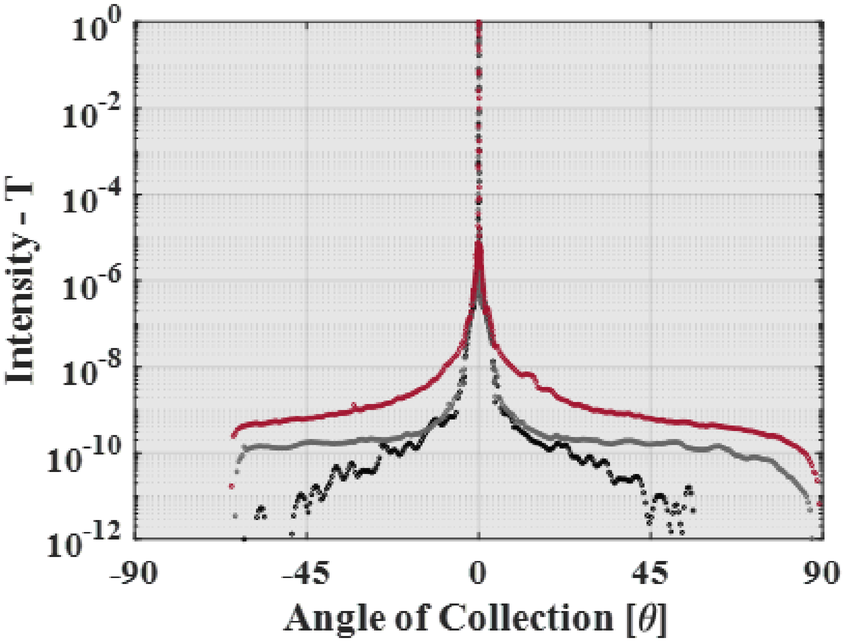

Figure 3.12. Comparison of single-surface processed (grey) nano-roughened ARSS samples to their double-sided processed (red) ARSS counterpart and optical flat (black). The amount of scatter increases with added surface roughness and is the higher for the double-sided roughened sample.

Processed ARSS samples were produced using identical fabrication methods for each substrate side, so that the final surface spatial feature distributions and sizes were identical. Samples with only one structured side were placed on the CASI holder, such that the structured-surface normal vector was antiparallel to the incident light wavevector (facing the detector) to help isolate scatter induced by the scattering interface to round-trip inside the substrate bulk before it transmits through. Figure 3.12 shows a comparison of the single-surface processed nanorough scatter distribution to scatter from an optically flat fused silica wafer. The amount of scatter is larger for the double-sided ARSS processed sample.

3.3: Surface Scatter in the Mid-wave Infrared

The second part of the study seeks to examine scatter from structured IR materials in the MWIR wavelength band. To do this, we measured BTDF using a vertically polarized, 3.39 µm, IR HeNe laser at 0°, 15°, 30°, 45°, and 70° AOI, sweeping AOC from -90° to +90° around the specular direction. For transmissive scatter, the nanostructured sample is compared to scatter from an optical-quality polished surface counterpart. Nanostructured IR samples were prepared by Nanohmics Inc.(Austin, TX), using the “thermodot” method introduced in Chapter 2. Transmission and reflection spectra are included alongside scatterometer data for the nanostructured samples, using the methodology outlined in Chapter 2. Fabrication parameters were optimized to achieve maximum possible transmission enhancement in the MWIR and were characterized using optical profilometry (Figure 3.13) and spectrophotometry.

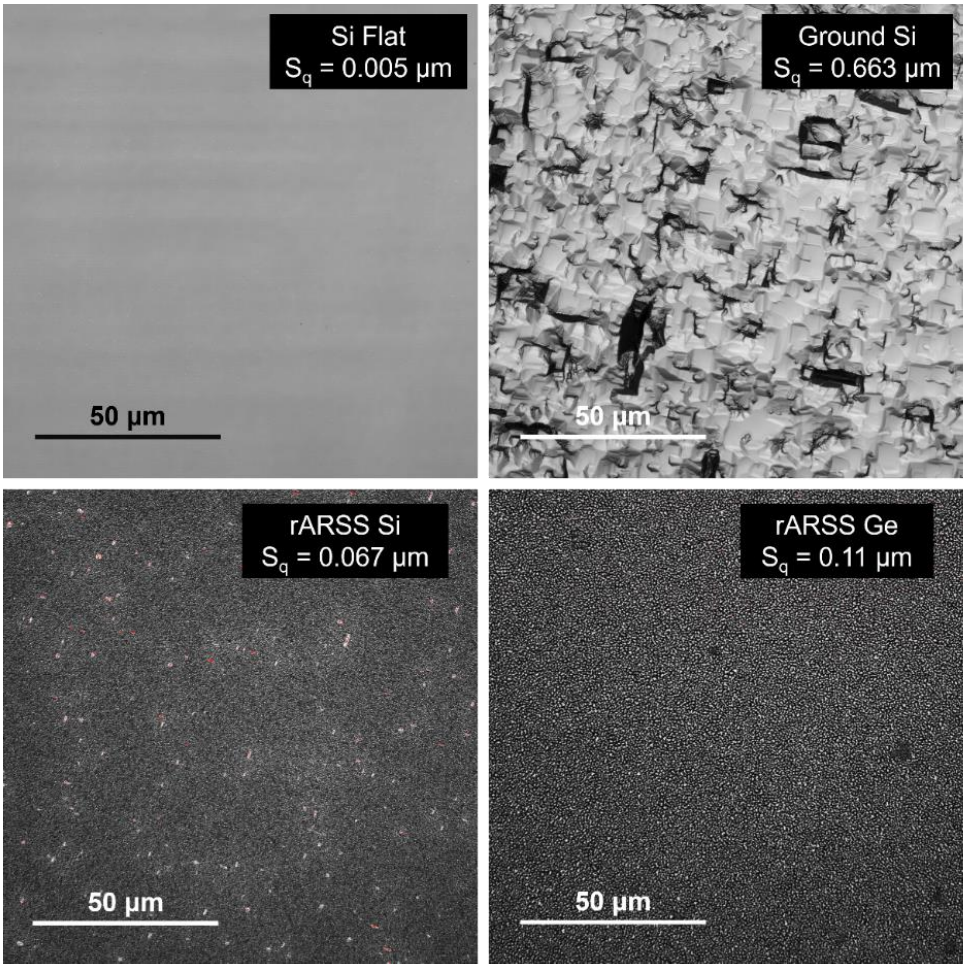

Figure 3.13. LEXT confocal images of infrared windows with different surface feature size scales, measured with 405 nm laser illumination.

Measured BTDF for each sample is plotted using the conventions listed above, for comparison of surface roughness scatter effects at selected AOI (Figures 3.14 and 3.15). The measured data was normalized to the instrument axial transmission signature at the test wavelength. Due to limitations in the setup, data was not distinguishable from noise at values $<10^{-9}$ sr^{-1}.

3.3.1: Diffuse Surface Infrared Scatter

Fused silica and Si ground glass BTDF measurements provide a baseline for the scattering characteristics of a surface with features comparable to the incident wavelength (Figure 3.14). Figure 3.15 compares flat and nanostructured surface BTDF at each AOI.

Both ground glass substrates scattered light off the axial direction. The mechanically ground FS average feature height was comparable to the probing wavelength and resulted in paraxial broadening of the radiance. Ground Si features were approximately 10-times smaller than the probing wavelength and produced more uniform wide-angle scatter than ground FS. Based on the literature, ground substrates were expected to diffuse light significantly in the visible regime [25]. MWIR wavelengths are on the order of five to eight-times larger than visible light, therefore the relevant roughness will change the light diffraction profile beyond the interface. The specular peak is much greater than the surrounding shoulders, unlike the BTDF measurements shown in Figure 3.3. BTDF wide-angle scatter peak shifts its angular position away from the specular as AOI increases, similar to trends seen in Figure 3.9.

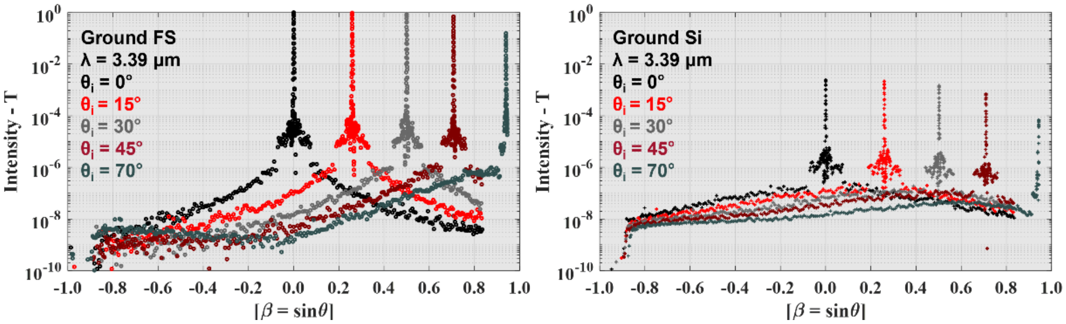

Figure 3.14. BTDF of ground glass samples normal (black), 15° (red), 30° (gray), 45° (dark red), and 70° (teal) AOI. Fused Silica (left) and Si (right) ground glass BTDF provide a baseline for the scattering characteristics of a surface with features comparable to the incident wavelength. Ground Si, which has a peak depth comparable to the incident wavelength, scatter distribution values span five orders of magnitude compared to nine orders difference between peak and side angle scatter values for ground FS.

3.3.2: Nanostructured Surface Infrared Scatter

Each rARSS sample exhibits reflectivity suppression over the measured wavelength band. The rARSS enhanced Si has transmission enhancement in the MWIR band, whereas rARSS Ge does not exhibit enhancement until the LWIR. All samples have non-negligible loss due to scattering, with rARSS Ge having the most prominent scattering edge at shorter wavelengths. Si has scatter losses over the entire measured wavelength band. Due to additional scatter, the overall enhancement of each sample's transmission is less than optimal theoretical values. Calculation of energy loss due to scatter is required to quantify the performance of rARSS for fabrication process optimization; however, it does not predict where light is scattered after incidence on the surface, which is important to understand the mechanism with which the structured surfaces will impact optical system performance.

Spectral data shows rARSS Ge scattered significantly more in the MWIR than polished Ge (Figure 3.15 top left), and is replicated in the wide-angle BTDF data (Figure 3.15 top right) which has scatter on the order of 10^{-7} compared to the flat sample's wide-angle scatter (Figure 3.13 top middle), which is below the noise floor of the measurement. Axially, flat and rARSS Ge differences were negligible. rARSS Si axial transmission and wide-angle scatter is unperturbed compared to flat Si (Figure 3.15 bottom left). Wide-angle scatter of rARSS Si is expected based on the calculated TIS shown in Figure 3.15 bottom-left, but is nearly unresolvable in transmission mode (Figure 3.15 bottom right).

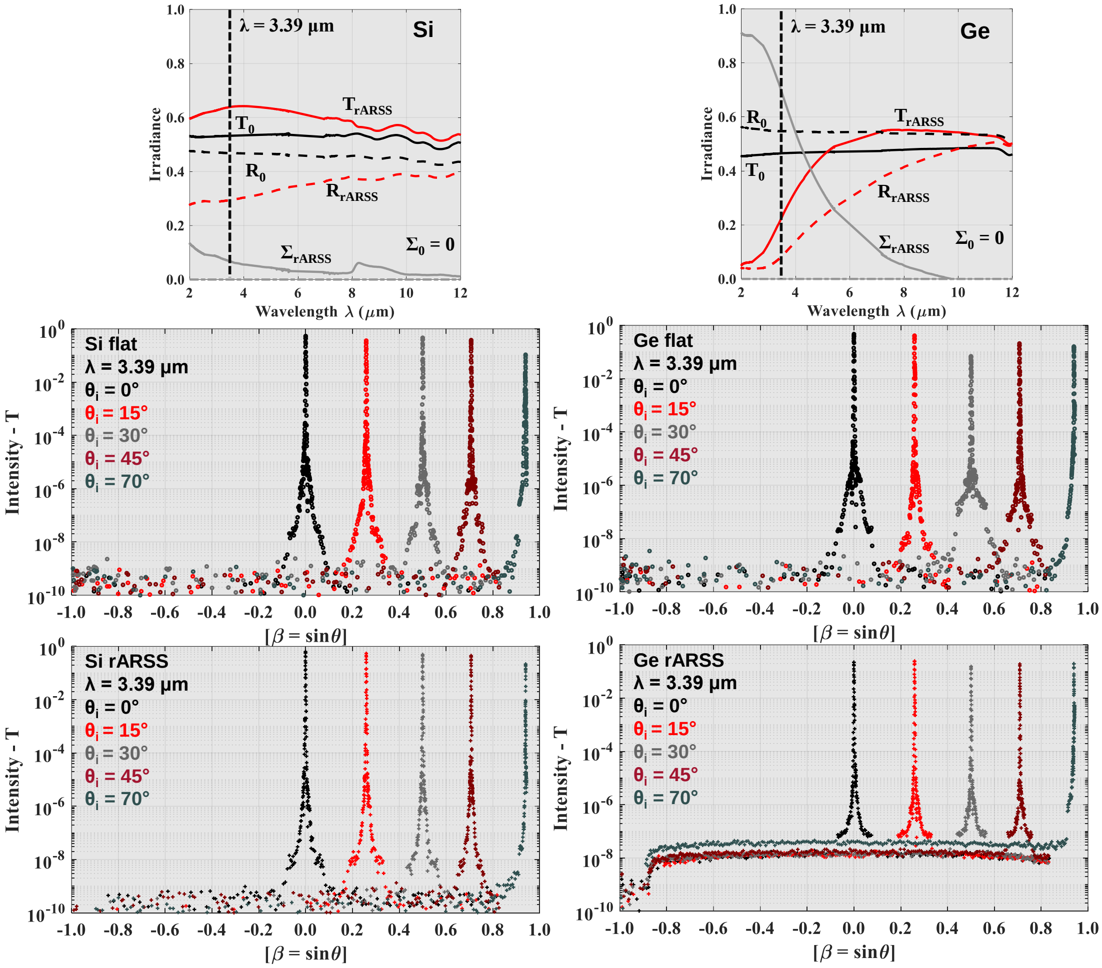

Figure 3.15. Spectra of the flat and processed rARSS samples (top) and their BTDF at wavelength labeled in the spectral graphs. Optical flat (middle row) and rARSS (bottom row) BTDF at normal (black), 15° (red), 30° (gray), 45° (dark red), and 70° (teal) AOI are presented. rARSS samples had enhanced transmission and narrowed paraxial scatter than the flat. Ge rARSS (bottom right) substrates have increased wide angle scatter while Si rARSS (bottom left) scatter is nearly unresolvable by the setup.

3.4: Discussion of Scatterometry Measurements

Uncertainty in BSDF measurements presents a difficulty in obtaining absolute scatter data [24]. These uncertainties can arise from many different sources, including incident flux variations, detector noise, and non-linear responsivity, background noise fluctuations, and sample/detector plane misalignment. Generally, measurements are compared with respect to relative behavior, rather than absolute values, which can have up to an order of magnitude variance under adverse conditions.

Proper alignment of the CASI considers the effects of guiding light source energy through many optical components, such as spatial filtering through a circular pinhole before focusing, that will have an impact in the quality of the CASI system signature. Any deviation from the expected output, such as biasing to one hemisphere or nonuniformity from the expected distribution, is accounted for in the measurement, and careful alignment is conducted to minimize the impact of misalignment. Azimuthal and polar misalignment stems from manual alignment of the sample by its retroreflection. Any tilt of the sample displaces the beam from its intended detection plane and offsets the central lobe of the BSDF. Offset of the detector to compensate for the displacement is possible but can present issues if the detector plane is not parallel to the incoming wave vector.

Detector nonlinearity and background noise can be an issue when taking low-power BSDF measurements. For example, liquid-nitrogen-cooled detector responsivity can vary as the detector begins to heat up, leading to unresolvable low power signals. Similarly, a hot room can produce thermal background (noise) that overcomes low power IR sources. Taking note of the instrument signature can provide insight into the outcome of a scattering distribution measurement.

The BSDF can span nine or more orders of magnitude due to the detector's variable gain settings and aperture solid angle that ranges from 10^{-4} to 10^{-8} sr (BSDF $\propto 1/\omega$); if the error is within an order of the normalized BTDF peak value, radiant power is discriminated in the paraxial and wide-angle region. Meaningful comparisons of scattering profiles between flat samples and rough samples are possible through qualitative observations. For rough surfaces, the wide-angle scatter is differentiated from the polished samples by an increase in its magnitude. However, this is not the case for comparing scatter between rough samples, where the surface feature distributions are similar, but not equal, and the wide-angle scatter increase is nearly equal.

Comparison of relative scattering trends between samples is important, in the context of rationalizing the performance of an optical window due to the presence of roughness. In cases of randomly roughened optical window surfaces, modeling of the absolute scattering performance is difficult, due to the limits of the statistical parameters with which we define the random surface. The conventionally used rms-roughness (S_q) measure is useful to qualify nanostructured surfaces due to the Gaussian distribution of transverse features; however, extending the rms-measure as a single quality parameter can mask distinct surface scattering effects, when the surface feature size distribution is of the order of the incident wavelength.

rARSS peak BSDF value is shift-invariant to oblique AOI (>70°), unlike diffuse ground glass samples presented here and in Harvey's work [35]. Scatter effects depend largely on the roughness size scale compared to the incident wavelength of light, and relevant spatial frequencies on the sample's surface determine if the incident light diffracts. Although the nanorough surface features diffract light, most of the light propagates paraxially, unlike ground glass samples whose features will act like a collection of random weak gratings. This may be due to the subwavelength structures producing evanescent orders which recouple into the zero order, much like a grating component does.

3.5: Conclusions

In this chapter scatterometry was used to measure the surface scatter performance of samples with varying magnitudes, ranging from optically flat to diffuse microrough (mechanically ground) over the equatorial plane of incidence, using a directional scatter instrument. The nanostructured surfaces have lateral cross-sectional features which are on average dimension within one order of magnitude to the incident wavelength, a scale that requires measurement of directional scatter, to determine the incident irradiance re-distribution beyond the optical surfaces, in both the forward and backward direction.

For rARSS, intensity is scattered into wide AOC, and simultaneously the transmitted paraxial intensity distribution is confined, leading to an enhancement of the window's transmission. While rARSS is useful for reducing reflected light, multiplicative scatter present in samples with roughened front and back interfaces may give rise to issues in image resolution or contrast for imaging systems with many optical components, especially at ultra-high sensitivity systems.

Relevant spatial frequencies near the incident radiation wavelength value result in observable diffraction effects, which distribute light into wide-angles from the axial direction, whereas mid-spatial frequencies are responsible for axial scatter effects. Spectral measurements can provide insight into axial or specular performance of a substrate; however, it is difficult to quantify the direction of the resulting scattered light. Band-limited scatterometry measurements can give insight into the mechanisms of light scatter and give quantitative data on where light is distributed after it is incident on an optical surface.

Off-axis specular performance in optics is examined using the conventional general fundamentals of optical scatter. Residual surface roughness, subsurface scatter from coatings, particulate scatter and bulk scatter due to index fluctuations, all need to be considered when characterizing the transmissive or reflective performance of an optical component [20]. While scatter can be detrimental to the performance of an optical system, it can also be used to preferentially suppress physical properties of optical interfaces by selectively adding features to produce a controlled scattering effect.

Chapter 4 explores the Generalized Harvey Shack surface scatter theory, using the statistical properties of the surface obtained through profilometry. Results shown in Chapter 3 are compared to modeled results based on a linear systems approach of scaler diffraction theory. The theory is applied to optically flat, micro-rough, and nanorough surfaces, to access diffractive scatter for different feature size scales.

CHAPTER 4: MODELING OPTICAL SCATTER

4.1: Introduction

The Generalized Harvey-Shack (GHS) surface scatter theory is a linear-systems transfer function approach that computes the angular redistribution of light after reflection or transmission from a statistically "rough" interface [20,34-36]. Using GHS one may obtain light scatter distributions from a rough interface within the far field approximation, by simply taking a Fourier transform of a complex pupil function, which is described by statistical quantities.

4.1.1: The Generalized Harvey-Shack Surface Scatter Theory

GHS defines the surface transfer function (STF_s) as:

$$STF_s(\hat{x},\hat{y},\gamma_i,\gamma_s) = e^{-\left(2\pi\hat{\sigma}(n_i\gamma_i - n_s\gamma_s)\right)^2\left(1-\frac{ACV_S(\hat{x},\hat{y})}{\sigma_S^2}\right)}, \tag{4.1}$$

where n_i and n_s describe the incident and scattering medium index of refraction, $\hat{x}$ and $\hat{y}$ are wavelength-normalized spatial coordinates of the surface, σ_s and $\hat{\sigma}$ are the rms roughness of the surface and its wavelength-normalized value, ACV_s is the autocovariance of the surface height profile, and:

$$\gamma_i = cos\,\theta_i \text{ and } \gamma_s = cos\,\theta_s = \sqrt{1-\alpha_s^2-\beta_s^2}, \tag{4.2}$$

are direction cosines, with θ_i and θ_s are the incident and scattering angles respectively.

The STF_s can be separated to its specular and diffuse components, and Fourier-transformed to obtain an *ASF*, which is the angular distribution of light in cosine space, given by:

$$ASF(\alpha_s,\beta_s) = \boldsymbol{F}\left\{STF_S(\hat{x},\hat{y},\gamma_i,\gamma_s)e^{-j2\pi\alpha_o\hat{x}}\right\}\Big|_{\alpha=\alpha_s,\beta=\beta_s}, \tag{4.3}$$

where α_s and β_s represent cosine space coordinates and $\alpha_o = \sin\theta_o$, where θ_o is the specular angle that varies depending on the incidence angle as well as the desired hemisphere for calculating the scatter distribution.

In the case of reflection, the law of reflection can be applied such that: $\theta_o = -\theta_i$. For transmission through a single interface, Snell's law is applied to account for refraction of the beam at the interface, therefore $\theta_o = \arcsin(n_i \sin\theta_i / n_s)$. Radiant intensity is obtained by multiplication of the final *ASF* distribution with the cosine of the collection angle.

4.1.2: Surface Feature Descriptions

Of particular importance for the GHS theory is the *ACV* and *PSD* of the surface, which describe the spatial distribution of surface features. A height map profile of a surface, obtained via profilometric methods, can be used to calculate a *PSD* by taking the 2D-Fourier transform of the surface height profile. Likewise, *ACV* is obtained by taking a normalized 2D-autocorrelation of the surface profile. Mathematically, the *ACV* and *PSD* are a Fourier transform pair:

$$ACV(x, y) = \boldsymbol{F}\{PSD(f_x, f_y)\}. \tag{4.4}$$

For high-resolution maps of surface height profile measurements, a Fourier transform (or serial multiplication) algorithm can be computationally intensive; alternatively, characteristic equations which take into account the statistics of a structured surface can provide a suitable approximation for calculations. It has been shown that random rough surfaces generally have Gaussian distributions of scaled features and can be approximately characterized by the surface root-mean-square roughness parameter S_q, referred to as σ_s above [19]. If a surface is well defined by Gaussian statistics, the *ACV* and

PSD can be modeled by a characteristic Gaussian equation that incorporates those measured experimental surface roughness parameters such that:

$$ACV_S(\hat{x},\hat{y}) = \sigma_S^2 e^{-\frac{(\hat{x}^2+\hat{y}^2)}{\hat{\ell}_c^2}}, \tag{4.5}$$

where $\hat{l}_c$ is the wavelength-scaled autocorrelation length of the surface. The analytical Fourier transform of Equation 5, yields:

$$PSD\left(f_x, f_y\right) = \pi\sigma_S^2\ell_c^2 e^{-\pi^2\ell_c^2\left(f_x^2+f_y^2\right)} \tag{4.6}$$

These approximate forms are useful for describing the surface but may not fully encompass the surface feature distribution, due to bandlimited measurements and other approximations used in roughness parameter numerical analysis, therefore it can be useful to obtain surface roughness information from multiple measurement sources [29,35].

The methods of scatter measurement are inherently limited based on the wavelength of light used to probe the surface as well as the incident angle of light, which causes a projection of the surface features to the incident beam profile. The relevant, or bandlimited, roughness of the surfaces with respect to those experimental parameters is:

$$\sigma_{rel}(\lambda,\theta_i) = \sqrt{\int_{\left(f_o-\frac{1}{\lambda}\right)}^{\left(f_o+\frac{1}{\lambda}\right)} \int_{-\sqrt{\frac{1}{\lambda^2}-(f_x-f_o)^2}}^{+\sqrt{\frac{1}{\lambda^2}-(f_x-f_o)^2}} PSD\left(f_x,f_y\right) df_x df_y}, \tag{4.7}$$

where λ is the wavelength of light incident at the surface, f_x and f_y are spatial frequency coordinates of the surface, and $f_o = \sin\theta_o/\lambda$ is the shifted central coordinate of the bandlimited portion of the PSD. For spatial frequencies greater than $1/\lambda$, scattered light becomes evanescent, therefore irrelevant to the angular distribution of propagating light.

4.1.3: Recoupling of Evanescent Energy

When light falls outside of the unit circle in cosine space, the angular light distribution must be renormalized to account for losses due to evanescence, and the recoupling of energy into lower diffraction orders. To do this, we take the ratio of all the light within the scatter hemisphere and the light contained within defined cosine space,

$$K_{\{T,R\}} = \frac{\{T,R\}}{\int_{-1}^{+1}\int_{-\sqrt{1-\alpha^2}}^{+\sqrt{1-\alpha^2}} ASF(\alpha,\beta)\,d\beta\, d\alpha} \tag{4.8}$$

where T and R represent the power (intensity) transmission and reflection coefficients whose formulas can be found elsewhere [33-34]. The numerator in Equation 4.8 is equal to unity when considering conservation of energy of the system (for perfect reflection or transmission); however, when considering lossy metals, dielectrics, or semiconductors, the inherent material losses at an optical interface will cause the reflected or transmitted light within the hemisphere to be less than unity. Therefore, the theoretical total percentage of light in the numerator must be material dependent and therefore can be approximated by the Fresnel equations.

Information on the GHS is widely available in the literature and this implementation was verified using data and results published by Harvey and others [20,36-37]. At a minimum, calculation of the surface scatter distribution requires measurement of the surface height profile, which can be used to calculate the PSD, ACV, and surface roughness parameters. In other words, it is necessary to know the morphology of the surface to understand how it scatters light.

4.2: Surface Profile Characterization

Nanostructured surfaces were imaged using a SEM, at 10kV and 50,00x/20,00x for FS/Si, respectively, to view the top-down distribution of transverse features (voids and islands). Two sets of granulometry results were obtained from the micrographs, one for islands and another for voids, by clustering pixels to octagons of scaled diameters (granules) and counting the feature populations by size (Figure 4.1). rARSS transverse granules in FS samples ranged from 2-60 nm, with a maximum diameter of 40 nm for both voids and islands. Si rARSS voids were ~50% larger than islands, with a maximum diameter of 170 nm for voids and 110 nm for islands. Based on these granulometric histograms, FS rARSS features are fine and dense due to the existence of equal number of similarly sized islands and voids. Si rARSS can be classified as fine and sparse, as there are a greater number of voids than islands, and the voids are statistically larger in diameter compared to the islands. All transverse features for rARSS were subwavelength (<λ/10) for the spectral regions of interest.

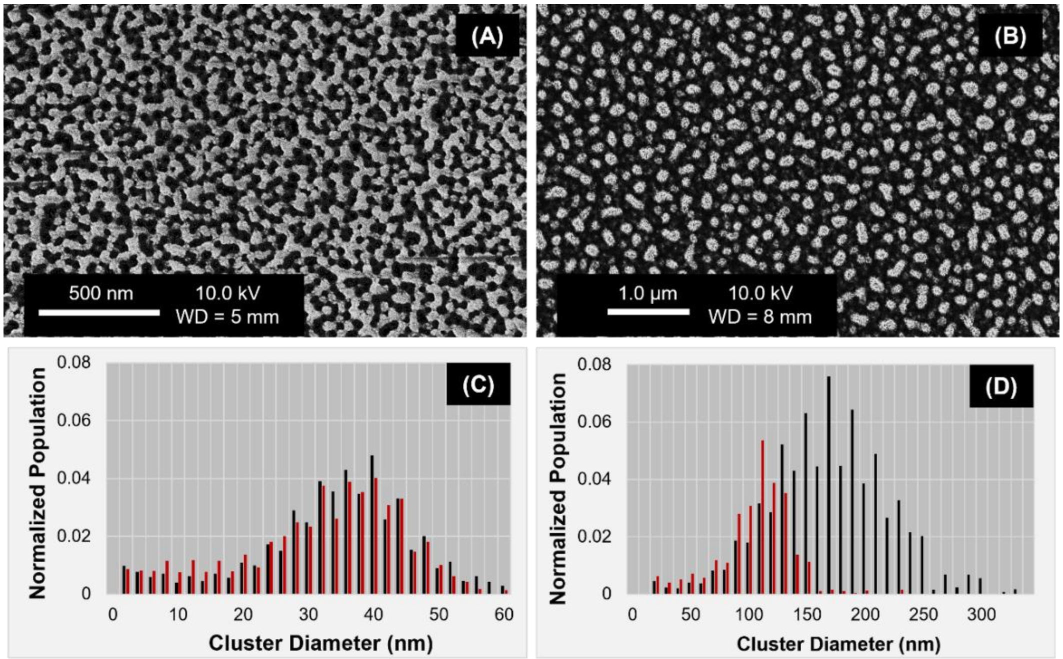

Figure 4.1. SEM micrographs of rARSS in: (A) – fused silica and, (B) – silicon. The corresponding granulometric normalized (to the measured areas) histograms are shown as (C) and (D). The red bars indicate island distributions, and the black bars void distributions.

4.2.1: Optical Profilometry of Structured Surfaces

For the GHS surface scatter theory, it is necessary to obtain surface feature height data to use as input for the GHS calculation. Although SEMs discern transverse feature data, the field of view is small and is unable to generate meaningful height data. This is due to the limited viewing angles of the SEM, requiring approximation of the surface features, and uncertainty in height profile fidelity because surface features are destroyed by cleaving of the sample edge prior to imaging the facet. For these reasons, the surface height profile was measured using non-destructive optical profilometry.

Si and FS substrates with varying magnitudes of surface roughness were imaged via confocal microscopy (LEXT 5000, Olympus, Shinjuku City, Tokyo, Japan) at 100x magnification, and surface roughness parameters were obtained by analyzing the surface using the instrument software and verified with in-house calculations. Figure 4.2 includes images of six representative substrates (three FS, three Si, one of each roughness type) used in this study: optical-quality double-sided mechanically polished wafer (polished), a similar optical-quality single-sided mechanically ground substrate, and a random nanostructured sample with both sides processed with rARSS (rARSS).

Samples shown in Figure 4.2 were analyzed via Olympus LEXT software to produce a compilation of surface conventional roughness parameters in Table 4.1. The roughness parameters of interest include peak-to-valley height (S_z), root mean square height (S_q), arithmetic average height (S_a), autocorrelation length (S_{al}), and texture aspect ratio (S_{tr}).

Table 4.1. Selected surface roughness parameters obtained from analysis of UV confocal microscope images.

Label	**Sample**	**S_q (μm)**	**S_a (μm)**	**S_z (μm)**	**S_{al} (μm)**	**S_{tr}**
A	Polished FS	0.005	0.004	0.059	9.313	0.588
B	Unpolished FS	0.907	0.724	6.748	5.828	0.914
C	rARSS FS	0.038	0.031	0.429	21.781	0.842
D	Polished Si	0.007	0.006	0.054	13.250	0.328
E	Unpolished Si	0.663	0.520	6.312	6.203	0.928
F	rARSS Si	0.067	0.051	1.050	21.375	0.810

Polished samples had measured feature height values <10 nm, consistent with optical-quality flatness specifications. Ground samples had an S_q 100-times larger than their polished counterpart, on the order a micron and comparable (>λ/10) in the wavelength band of interest. Comparatively, nanorough rARSS S_q were 10-30 times smaller than the ground substrates and were sufficiently smaller than the wavelength of interest to be considered subwavelength (<λ/10).

Ground and rARSS samples were isotropic (S_{tr} = 0.928 and 0.81 for Si; S_{tr} = 0.914 and 0.842 for FS; respectively). For these samples, uniformity can be attributed to the crystalline-like unpolished side of the Si and FS ground glass and the random-distribution mask used for fabricating the rARSS sample. Unusually, polished Si and FS samples S_{tr} values were not consistent for isotropic roughness samples (S_{tr} = 0.588 and 0.328, respectively). A low-valued S_{tr} may be due to leftover polishing lines present on the sample or environmental contamination. S_{tr} is a ratio of the direction of fastest decay of the S_{al} to the direction of slowest decay, therefore any abnormally large feature (dust) can skew the value. It is noted that the samples have a different surface roughness lateral distribution as well, as shown in Figure 4.1, but the specific values are not well represented by height and spatial surface roughness parameters. Surface roughness parameters were used as inputs for the GHS scatter theory where applicable (Equations 4.1, 4.5-4.6)

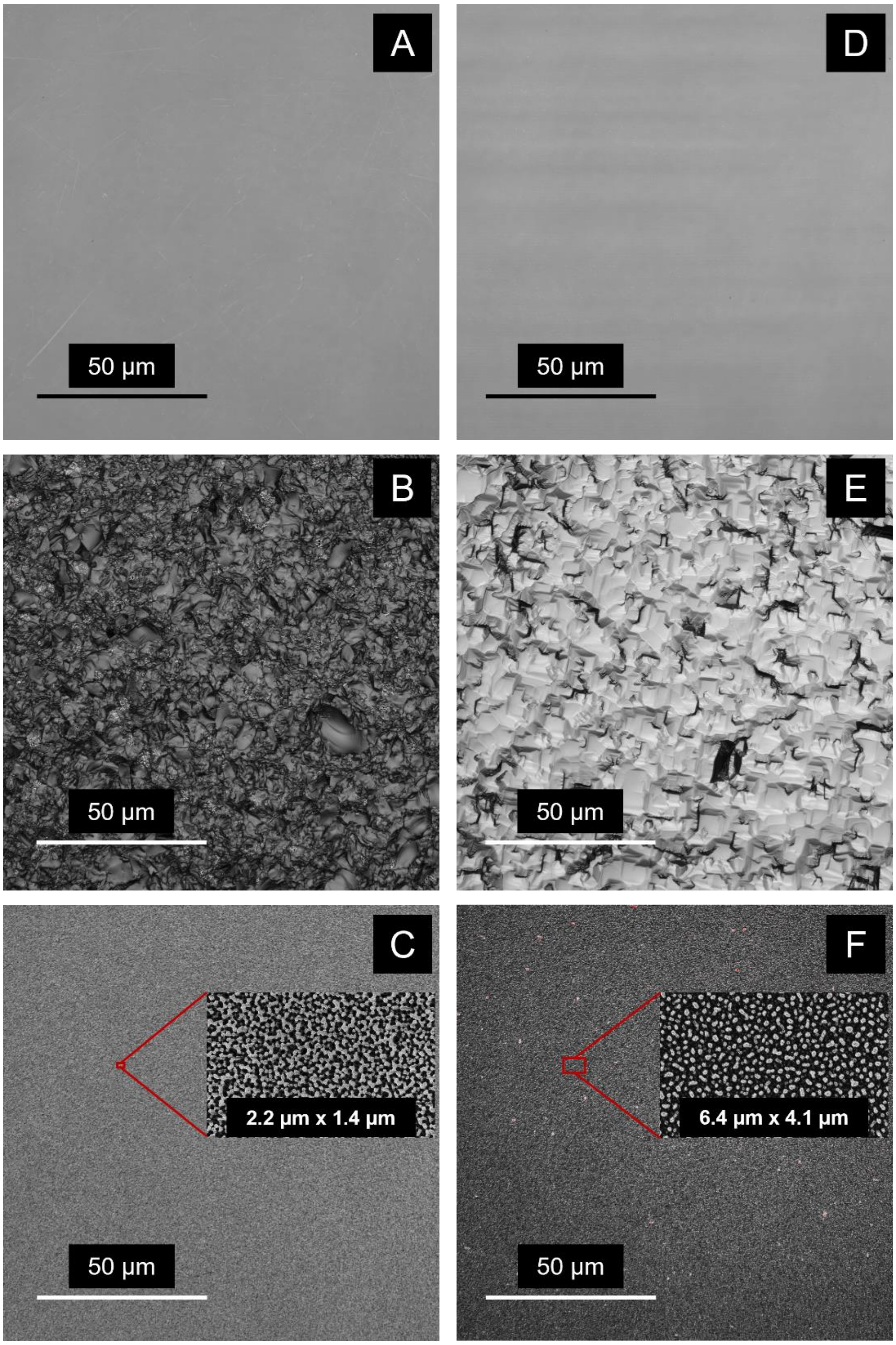

Figure 4.2. LEXT confocal images of polished FS (A), unpolished FS (B), rARSS FS (C), polished Si (D), unpolished Si (E), and rARSS Si (E) at 100x magnification. For reference, rARSS images (C and F) include inset of their respective SEM image shown in Figure 1. Images were processed using accompanying LEXT software to obtain selected surface roughness parameters shown in Table 4.1.

Experimental PSD was calculated by Fast Fourier transform (FFT) of the surface height map profile and Gaussian PSD were calculated by inserting surface roughness parameters into a characteristic Gaussian equation for random systems (Equation 4.6). PSD were then used to calculate the relevant roughness of the surface. Calculated PSD from experimental data and Gaussian two-parameter model are compared to assess applicability of the approximation to the samples of interest (Figure 4.3). Polished samples experimental PSD exhibit inverse power law behavior, not at all in agreement with the Gaussian model for a smooth surface. Low-frequency PSD for ground glass looks more Gaussian-like but the high spatial features follow inverse power behavior. rARSS PSD has a low spatial Gaussian lobe with Lorentzian shoulder extending to the high spatial regime. The cutoff frequency ($f_0 = 1/\lambda$) indicates the wavelength band stop for examining optical surface scatter effects and is used as a filter to calculate the relevant roughness of the surface (Equation 4.7).

Autocorrelation of the surface height map profile via explicit serial multiplication of the height data was used to obtain the surface ACV (Figure 4.4). ACV output array size was truncated to the 4096 x 4096 central square of the array to remove padding due to shift multiplication process. Gaussian ACV was produced by inserting surface roughness parameters into a characteristic Gaussian equation for randomly rough surfaces (Equation 4.5). Polished and ground samples experimental ACV array slices, taken in the $y = 0$ µm plane, and Gaussian ACV have similar distributions with peak value of approximately the variance of the surface height profile. rARSS ACV distributions exhibit a strong delta-like central peak, with Lorentzian function shoulders. The calculated ACV dictates the form of the surface transfer function (Equation 4.1); therefore, we can expect the rARSS samples to scatter most of the light axially, with some light being distributed into wide angle scatter.

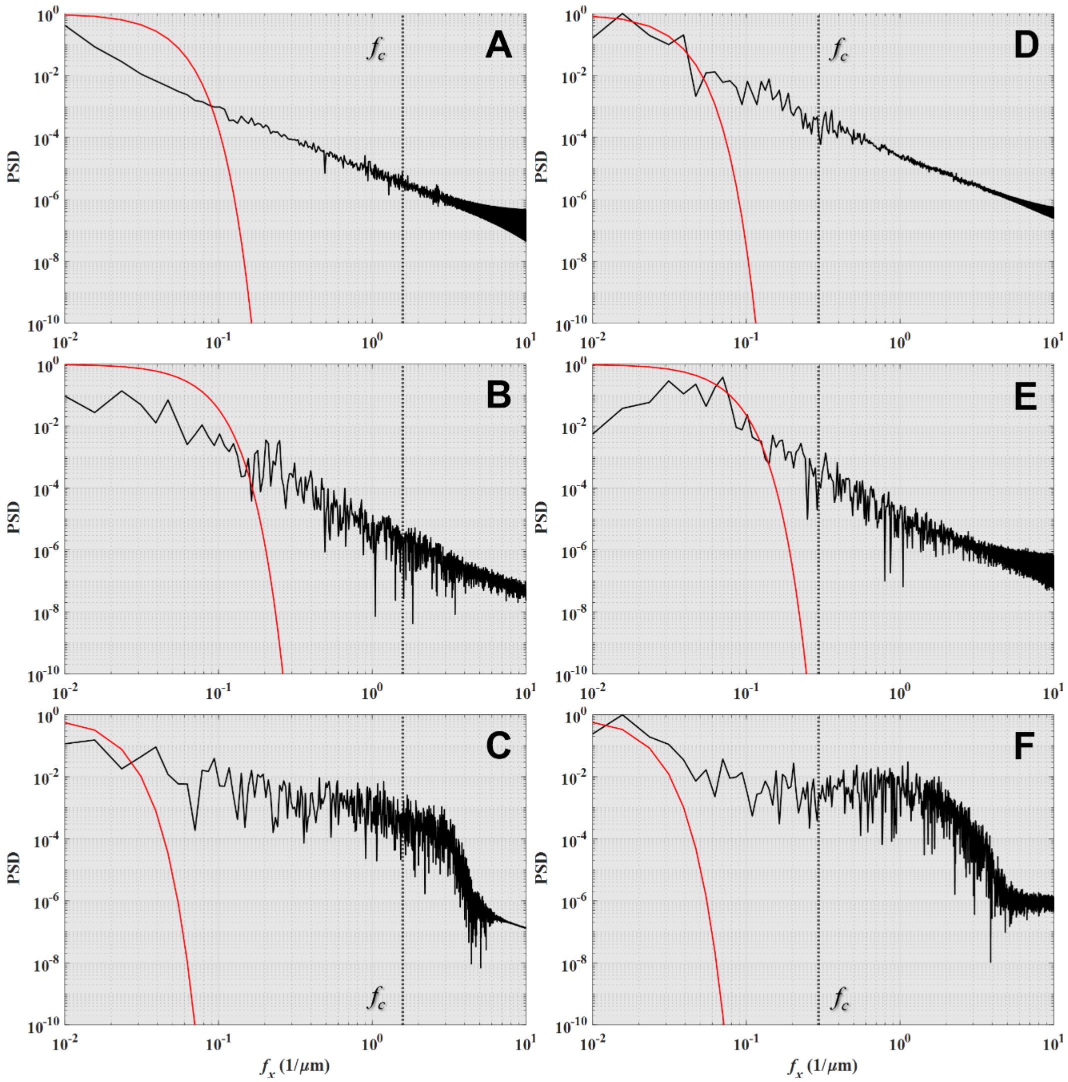

Figure 4.3. Polished FS (A), unpolished FS (B), rARSS FS (C), polished Si (D), unpolished Si (E), and rARSS Si (F) experimental PSD (black) was calculated by FFT of the surface height map profile and Gaussian PSD (red) was calculated by inserting surface roughness parameters into a characteristic Gaussian equation (PDF) for random systems. PSD cutoff frequency (vertical black dotted line) at normal incidence for the experimental wavelength of interest is shown for visualization of limits for calculation of the relevant roughness of the surface.

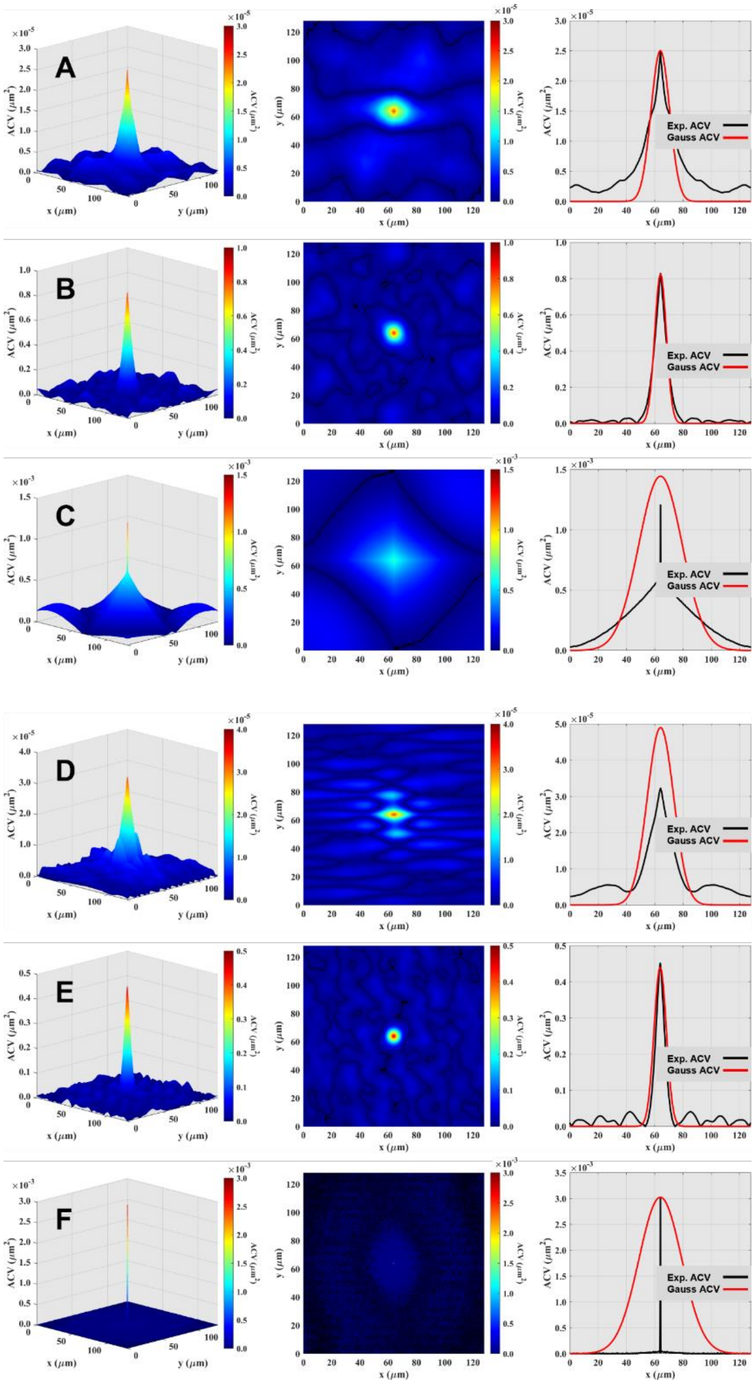

Figure 4.4. Polished FS (A), unpolished FS (B), rARSS FS (C), polished Si (D), unpolished Si (E), and rARSS Si (F) experimental ACV was calculated via serial multiplication of the measured surface height map profile. (Left) Three-dimensional output of ACV calculation. (Middle) Top-down visualization of experimental ACV. (Right) Comparison of experimental ACV (black) array slice taken in the y = 0 µm plane and Gaussian ACV (red).

4.3: Spectral Scatter Characterization

FS spectral data was obtained by averaging (n = 200) spectra over the visible to near-infrared (NIR) (400-1000 nm) wavelength band at 20.0 cm^{-1} resolution. Si spectral data was obtained by averaging (n = 100) spectra over the NIR to MWIR (2-6 µm) wavelength band at 4.0 cm^{-1} resolution. Substrates of interest have normal dispersion over the measurement bands, therefore $T(\lambda) + R(\lambda) + \Sigma(\lambda) \cong 1$. Atmospheric absorption in the IR contributes to losses in those specific bands and the effect is compounded when using experimental spectral data to calculate TIS.

Based on the measurements and spectral analysis conducted in Chapter 2, rARSS samples were known to have transmission enhancement at normal incidence, as well as an increase in off-axis scatter (Figure 4.5). In the case of FS, the maximum transmission ($T = 0.988$ at $\lambda = 500$ nm) with negligible specular reflection. TIS calculated from measured data indicates some light falls out of the specular region ($\Sigma = 0.012$ at $\lambda = 500$ nm), still within the tolerances of the spectrophotometer. Similarly, rARSS Si exhibits transmission enhancement ($T = 0.81$ at $\lambda = 3.5$ µm) as well as an increase in off-axis scatter ($\Sigma = 0.11$ at $\lambda = 3.5$ µm).

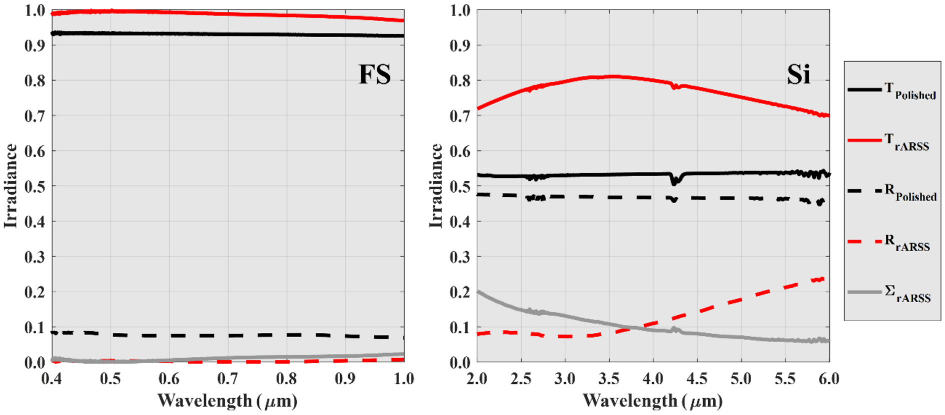

Figure 4.5. FS (left) and Si (right) of polished and nanoroughened rARSS samples normal incidence axial transmission ($T(\lambda)$), 15° AOI specular reflection ($R(\lambda)$), and calculated TIS ($\Sigma(\lambda)$).

To compare, theoretical TIS is calculated at normal incidence using the sample S_q and wavelength band of interest and normalized to the maximum TIS calculated from experimental spectra (Figure 4.6). Reflective TIS is defined as

$$TIS \approx \left(\frac{4\pi cos\theta\sigma}{\lambda}\right)^2 \tag{4.9}$$

where σ is the rms roughness of the surface, θ is the AOI of light, and λ is the incident wavelength of light.

Experimental TIS has larger values at shorter wavelengths, decaying with increasing wavelength, consistent with the decaying exponential behavior used for the theoretical TIS. However, there is a slight discrepancy between the slopes of the TIS curves. TIS calculated from measured spectra uses both transmission and reflection data, while the theoretical model only considers reflected scatter. For dielectric materials, it can be expected there is scatter on both the reflection and transmission side of the interface. Transmissive materials with surface scatter should experience a greater "loss" of light from the axial (specular) direction during measurements compared to purely reflective materials, leading to an increase in calculated TIS from measured data.

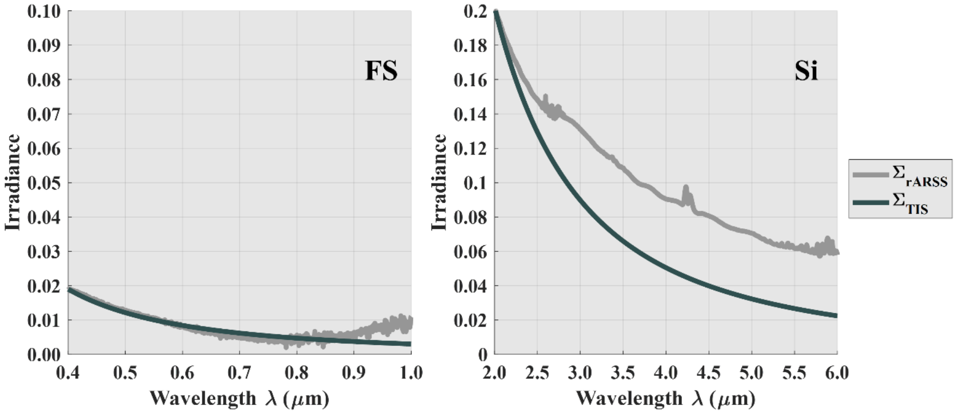

Figure 4.6. Experimental TIS (grey) is compared to theoretical TIS (teal) for two rARSS samples. (Left) Theoretical TIS for rARSS FS matches the trend of experimental TIS for shorter wavelengths. (Right) Theoretical and experimental TIS follow similar 1/e^2 trends, but with mismatched slopes.

4.4: Modeled Scatter using the Generalized Harvey-Shack Theory

GHS theory was implemented in MATLAB and data gathered from analysis of the images in Figure 4.2 was used as inputs for calculation of the *ASF* for each sample. Algorithmic implementation of the theory involves generous use of the MATLAB FFT function, which is used to transform the measured surface height map profile into a PSD or ACV (depending on calculation method), and the *STF* into the *ASF*.

After importing measured height map profile data and user defining input variables including S_q and S_{al} surface roughness parameters, AOI, incident wavelength, and material properties, the GHS routine is initialized and an *ASF* is calculated. Scatter distribution volumetric intensity (total transmission or reflection over 2π sr) was normalized to the material Fresnel transmission coefficient at normal incidence for comparison. *ASF* and *BSDF* are converted to radiant intensity and compared to assess the Gaussian two-parameter model of scatter with measured scatter data.

As we recall from Chapter 3, the BSDF was measured using a polarized-laser scatterometer (CASI, Scatterworks, Tucson, AZ). *BSDF* is commonly used to quantify scattered light distributions resulting from light incident on roughened surfaces. It is defined in radiometric terms as the scattered radiance (L) per incident irradiance (E):

$$BSDF = \frac{L(\theta_s, \varphi_s, \theta_i, \varphi_i)}{E(\theta_i, \varphi_i)} = \left. \frac{\Delta P(\theta_s, \varphi_s)}{\Delta\omega \Delta A \cos\theta_s} \middle/ \frac{P(\theta_i, \varphi_i)}{\Delta A} \right. \tag{4.10}$$

where θ_i, φ_i, θ_s, φ_s, define the incident and scattering angles, ω is the detector solid angle, ΔA is the area element of the scattering surface, ΔP denotes the radiant power collected by the detector, and P is the incident radiant power illuminating the area element [21].

Radiometrically, measured *BSDF* (Eq. 4.10) and calculated *ASF* (Eq. 4.3) are the same physical quantity [35]. Therefore, conversion of *BSDF* and *ASF* to radiant intensity requires multiplication of the *BSDF* and the sample's projected area with respect to the detector as it sweeps across the hemisphere. Although *BSDF* is dependent on the incident irradiance, the power and area of the incident spot does not change during a single AOI measurement, therefore measured *BSDF* is scaled by a cosine term to obtain normalized intensity. All samples shown in Figure 4.2 were measured using the CASI scatterometer in transmission mode to obtain bidirectional transmission distribution function (BTDF) data at varying angles of incidence.

The GHS-theory computer code was benchmarked using standard diffusers to determine fidelity of the code implementation. Ground samples were tested using the ACV and PSD calculated from experimental height map data and a characteristic equation representing a Gaussian distribution of the data (Figure 4.7-4.8). The specular component was omitted for ground samples, and the distributions were normalized for better comparison of off-axis scatter distribution. For ground FS at moderate angles of incidence, the theory fits well for Gaussian parameter model of the height distribution and the raw experimental height data (Figure 4.7). For predicted Gaussian scatter data, the angle of collection for the peak intensity shifts away from experimental scatter data as angle of incidence increases. Scatter distribution full width is approximately equal in all cases, signaling good agreement of the theory with measured results.

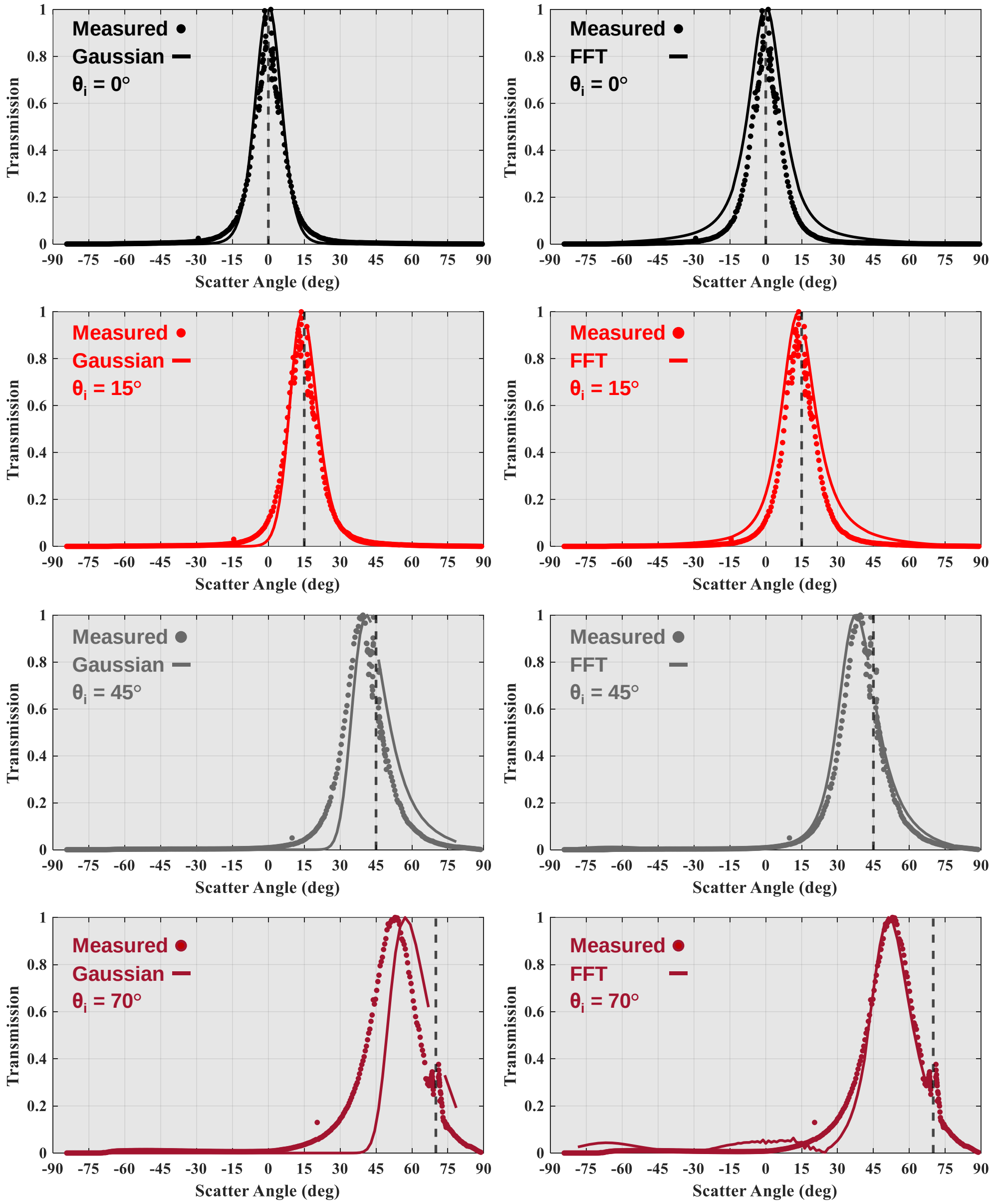

Figure 4.7. Calculated ASF (solid line) using a Gaussian model of the surface ACV (left) and experimentally derived ACV (right) is compared to measured BTDF (points) at 633 nm for ground FS samples at normal (black), 15° (red), and 50°(grey) AOI. The specular (axial) transmitted angle is notated by a vertical dotted line. Specular peak is suppressed for experimental data and scatter distributions were normalized for comparison of measured and simulated data.

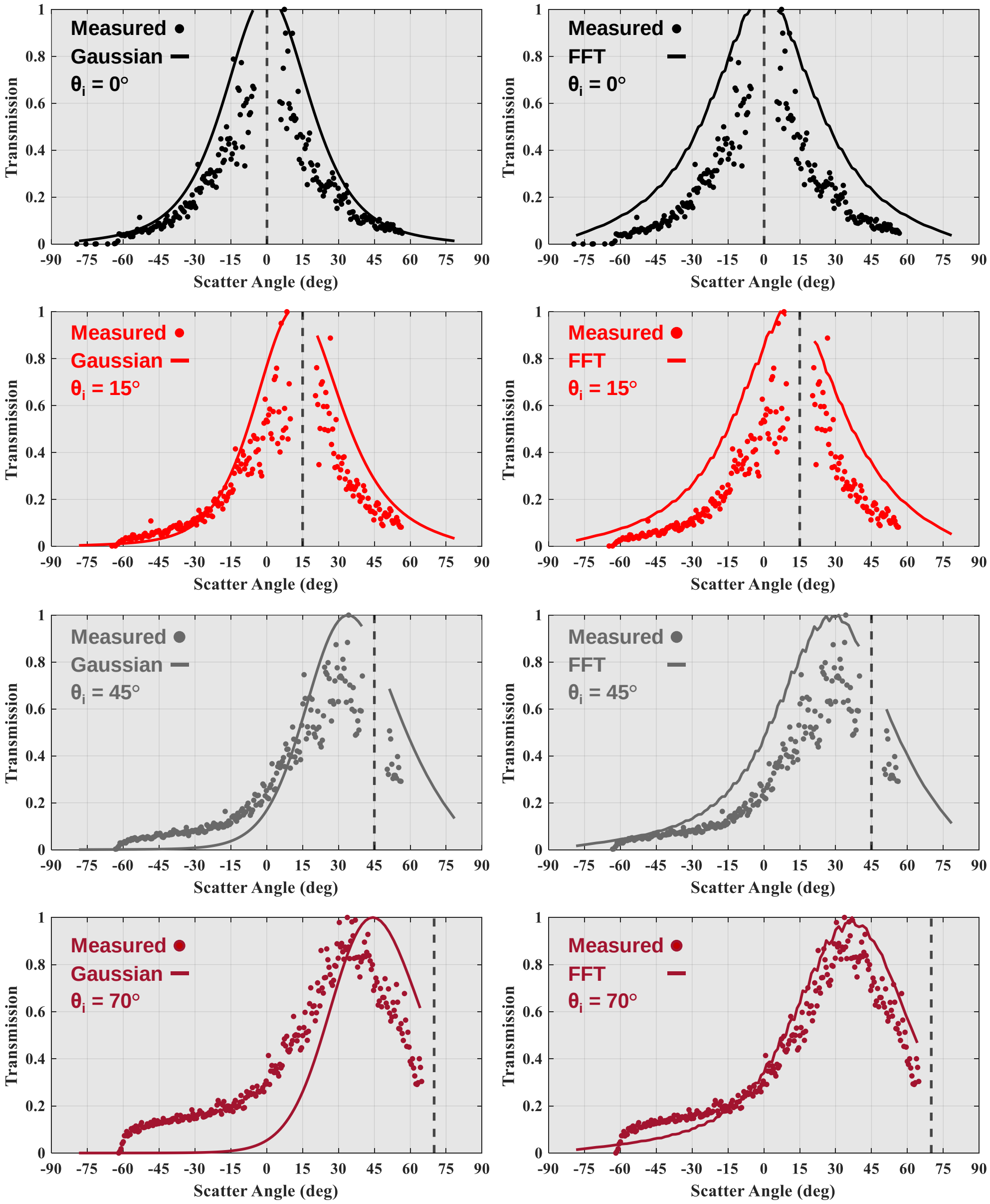

Figure 4.8. Calculated ASF (solid line) using a Gaussian model of the surface ACV (left) and experimentally derived ACV (right) is compared to measured BTDF (points) at 633 nm for ground Si samples at normal (black), 15° (red), and 50°(grey) AOI. The specular (axial) transmitted angle is notated by a vertical dotted line. Specular peak is suppressed for experimental data and scatter distributions were normalized for comparison of measured and simulated data.

Similar trends are seen with ground Si data; however, ground silicon, with a roughness of ~λ/5, has a much stronger specular component in the measured data which causes discrepancy with the theoretical scatter distribution (Figure 4.8). Ground sample features were approximately 1.5-times larger for FS and 5-times smaller for Si than the probing wavelength of the scatterometer. As such, those features were expected to diffract visible light, but not necessarily IR, as noted for Si measurements. Ground-Si experimental diffuse scatter distribution appears to be Gaussian-shaped, but the specular peak is much greater than the surrounding shoulders. Ground-Si *BTDF* diffuse scatter peak value shifts its angular position away from the specular as AOI increases, like data seen in the literature for diffuse surfaces [38].

Polished substrates are expected to have very little wide-angle scatter with a strong specular response; therefore, they are useful for accessing code fidelity for the opposite roughness regime. For both the Gaussian parameter model and experimental height data for a flat FS surface, GHS theory predicts a highly specular scatter distribution, but with some discrepancies in the order of magnitude of the scatter distribution (Figure 4.9). The GHS correctly predicts the location and shape of the distribution; however, it is unable to match the contrast of the specular peak to the wide-angle scatter. For the polished Si, the Gaussian parameter model predicts no scatter off axis while the experimental height data traces the shape and relative magnitude of the measured data (Figure 4.10). Again, the specular peak and wide-angle contrast for the calculated data does not match measured data.

Polished Si roughness was well below the bandlimit to generate appreciable amounts of scatter. The specular component of the calculated scatter distribution contains most of the transmitted energy, like experimental results that have strong specular response, but do not have the same contrast seen in the measured data. Experimental scatter instruments are limited by source beam divergence and other optical components (e.g., mirrors, apertures) which affect the signature of the instrument, and exhibit as a broadened specular beam compared to theoretical data.

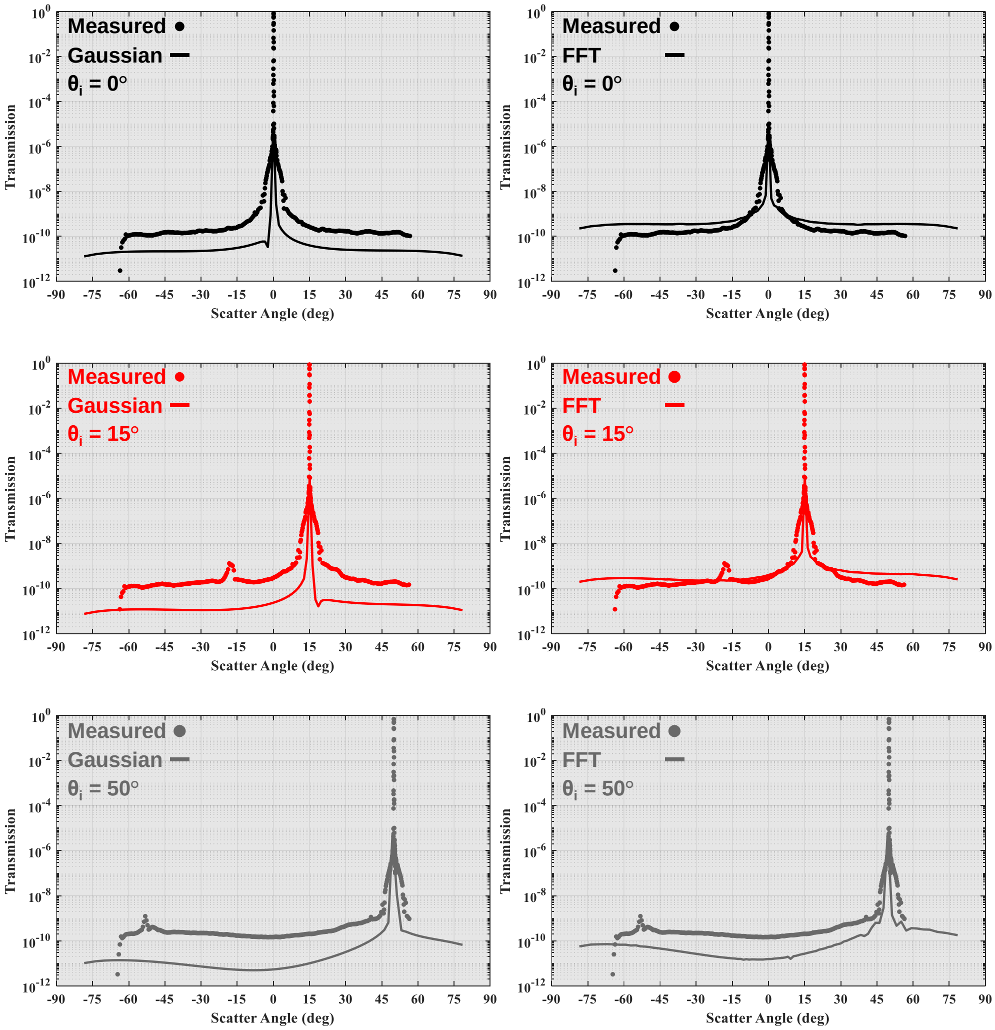

Figure 4.9. Calculated ASF (solid line) using a Gaussian model of the surface ACV (left) and experimentally derived ACV (right) is compared to measured BTDF (points) at 633 nm for polished FS samples at normal (black), 15° (red), and 50°(grey) AOI.

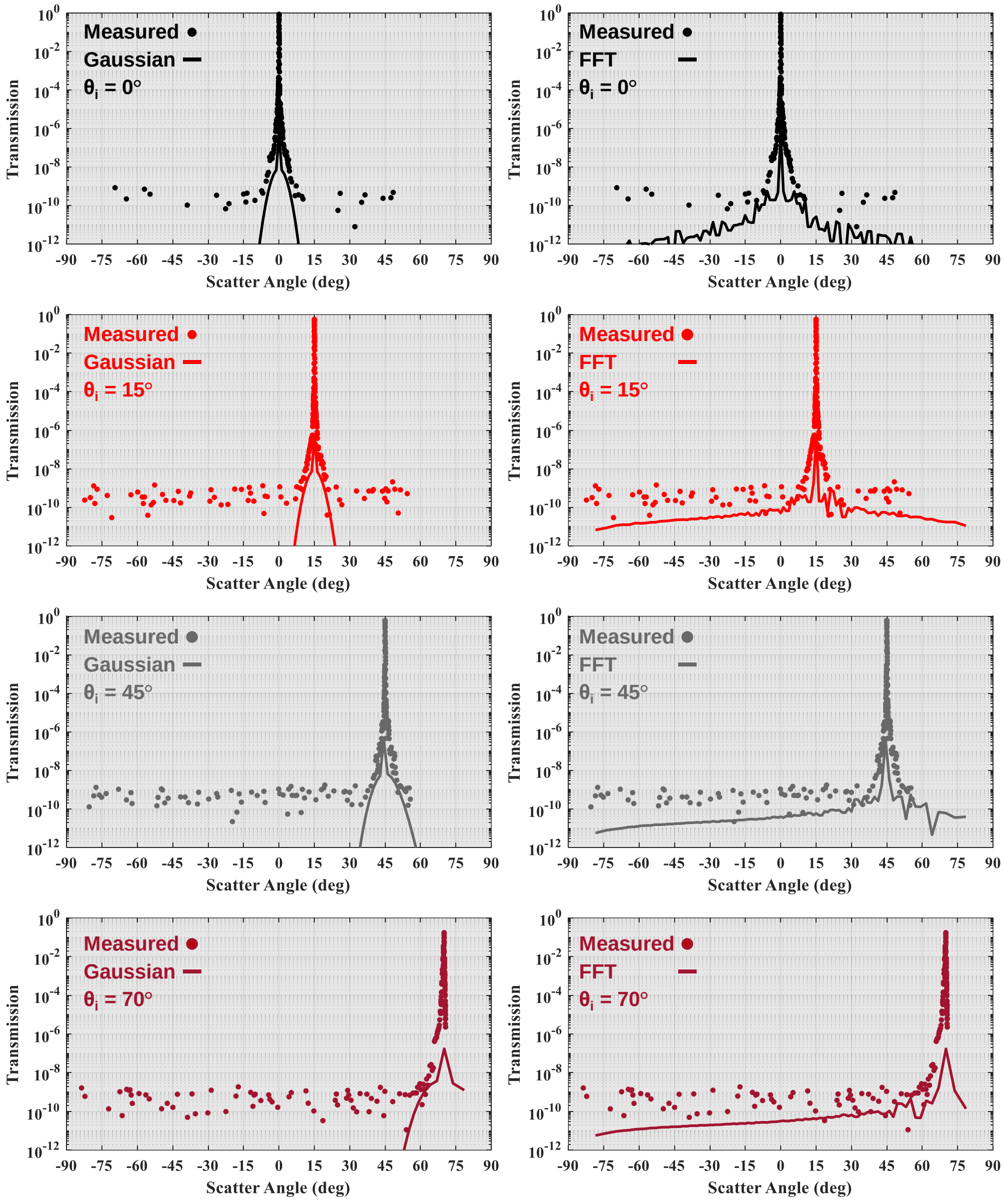

Figure 4.10. Calculated ASF (solid line) using a Gaussian model of the surface ACV (left) and experimentally derived ACV (right) is compared to measured BTDF (points) at 3.39 μm for polished Si samples at normal (black), 15° (red), 45° (grey), and 70° (dark red) AOI.

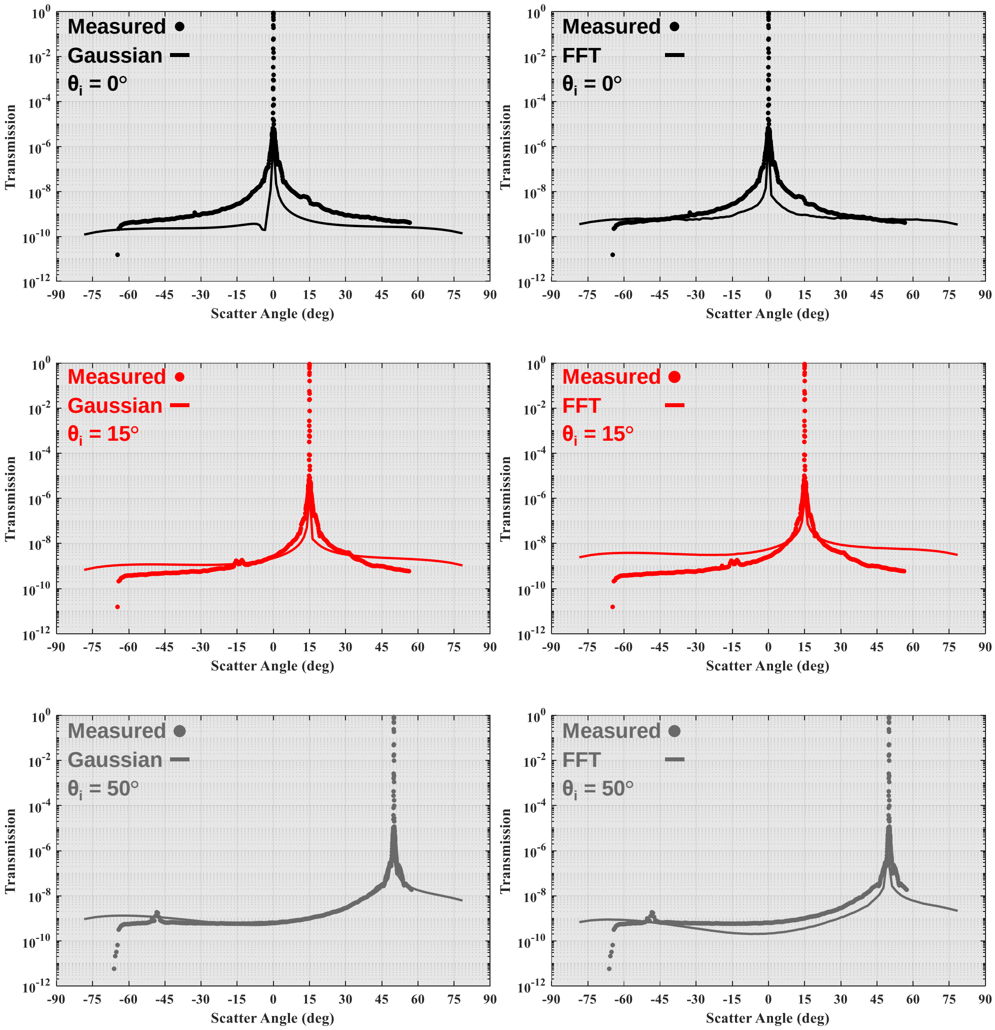

Figure 4.11. Calculated ASF (solid line) using a Gaussian model of the surface ACV (left) and experimentally derived ACV (right) is compared to measured BTDF (points) at 633 nm for nanostructured FS samples at normal (black), 15° (red), and 50°(grey) AOI.

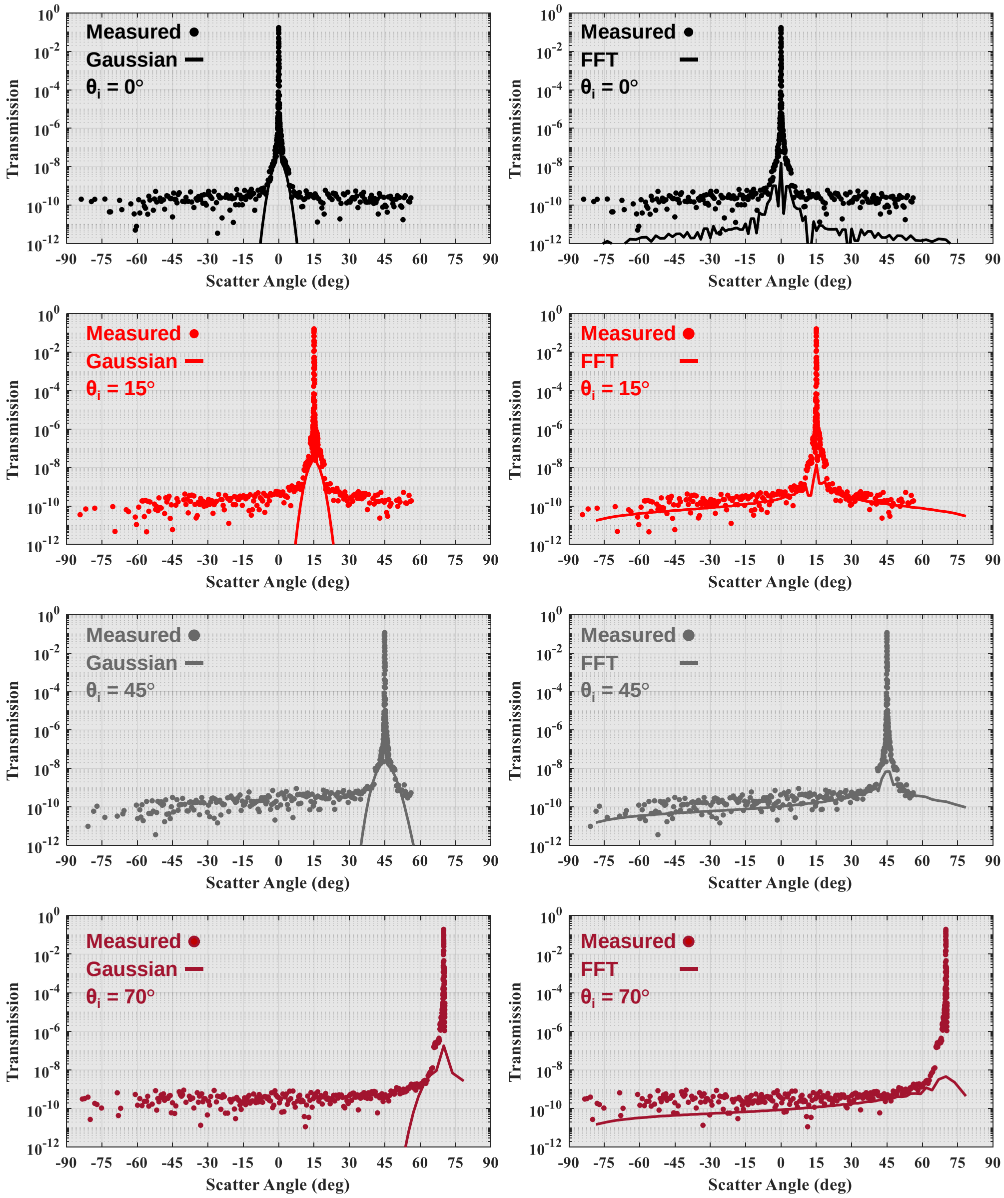

Figure 4.12. Calculated ASF (solid line) using a Gaussian model of the surface ACV (left) and experimentally derived ACV (right) is compared to measured BTDF (points) at 3.39 μm for nanostructured Si samples at normal (black), 15° (red), 45° (grey), and 70° (dark red) AOI.

4.5: Conclusions

rARSS samples axial transmission and wide-angle scatter is greater compared to their polished counterpart. rARSS also exhibits shift invariance with respect to AOI, with a narrowing of the axial scatter distribution as AOI increases. rARSS-FS calculated scatter using Gaussian two-parameter model and experimental height data agree with measured scatter data, with slight discrepancies in the specular beam width due to the assumption of a delta response in the axial direction (Figure 4.11). rARSS-Si Gaussian distributions do not match experimental data and fail to predict the diffuse scatter from the surface, as well as, the specular response (Figure 4.12). Scatter data using experimental height measurements traces the shape of the diffuse scatter, but does not indicate any strong specular response, suggesting the surfaces are purely diffuse, which is not observed in spectral nor scatter measurements. Although the contrast between specular and diffuse regions is less than expected, the axial transmission region contains most of the transmitted power, consistent with the antireflectivity of rARSS spectral measurements.

Approximating *ACV* and *PSD* as Gaussian distributions assumes the surface roughness to be globally and rotationally isotropic. For the *Str* values shown in Table 4.1, ground samples are the most isotropic sample but the nanorough samples are also mostly isotropic. For most cases, it is a good assumption that the *ASF* is rotationally symmetric if the roughness is also isotropic. This can reduce the number of necessary computations significantly by simplifying the Fourier transform to a 1-D problem [39-41]. Rather than approximating the surface feature distribution to be Gaussian, the height profile can be leveraged to generate a PSD and ACV to then be used as inputs for the GHS theory. By using the raw height data, the resulting scatter is no longer assumed to be due to globally isotropic roughness, as expected due to non-unity *Str* values.

Implementation of the GHS surface scatter theory and its application to random antireflective nanostructured materials was achieved. Optical metrology and granulometry were used to obtain statistical roughness parameters and morphological histograms of the surface features (voids and islands distribution). The surface feature data was consistent with Gaussian statistics; however, Gaussian statistics model of the nanorough surfaces scatter was not in agreement with experimental data. Although the approximations were unsuccessful, there may be other characteristic equations which can be used to describe the surface feature distribution.

Additionally, surface height map profile data was utilized to generate the necessary inputs for the GHS, but it was inconsistent with measured data due to limitations in the theory for sufficiently small and dense surface features with a strong specular response among its more diffuse scatter behavior compared to optically flat components. It was shown that the theory can predict redirection of light from specular to diffuse region but was unable to predict enhancement of light throughput in the axial direction, therefore additional testing is necessary to improve consistency of GHS to predict scatter from surfaces with subwavelength features.

CHAPTER 5: CONCLUSIONS

5.1: Summary of Nanostructured Surface Spectral Characterization

Characterization of nanostructured surfaces using spectrophotometry is standard practice for determining the transmission and reflection properties of axially propagaing light. By leveraging multiple measurements of both polished and structured surfaces, the surface-induced Fresnel reflectivity reduction, including additional bidirectional scatter was calculated for the presence of the single structured surface alone. Structured surfaces presented had measurable specular losses due to scatter in the MWIR while also enhancing the axial transmission throughput of the material.

Suppression of the specular direction intensity does not imply an absolute enhancement of axial transmission through a nano-structured window; rather, an increase of the main- and side-lobe directional irradiance and angular spread is observed. Fresnel reflectivity of nanostructured AR surfaces is shown to be suppressed in the specular region, because light is redistributed from that specular region to wider angles and forward scattered to the transmission direction.

As the wavelength of light increases compared to the size of the surface features, the suppression of the directional radiation is less prominent, while the side lobes maintain comparable values to the optically flat substrate. This trend is evident when examining the magnitude of scattering at single wavelengths or angles of collection; however, this does not uniformly scale with light scatter from short to long wavelengths.

5.2: Summary of Experimental and Modeled Optical Scatter

To gain a better understanding of the wide-angle scatter effects of nanostructured surfaces, scatterometry was used to measure the surface scatter performance of samples with varying magnitudes, ranging from optically flat to diffuse microrough (mechanically ground) over the equatorial plane of incidence, using a directional scatter instrument.

Ground glass surfaces that have surface roughness on the order of the incident wavelength of light diffusely spread light into the hemisphere, with very little retention of specular reflection and axial transmission peaks. For rARSS, intensity is scattered into wide AOC, and simultaneously the transmitted paraxial intensity distribution is confined, leading to an enhancement of axial transmission. Scatter is impacted (multiplicatively) by index contrast of ambient and substrate (material dependence) and leads to an increase in wide angle scatter effects. Additionally, scatter measurements verified the angular shift invariance of the scatter distribution from random antireflective nanostructured surfaces.

The Generalized Harvey-Shack scatter model (GHS) was implemented for predicting transmissive scatter and tested the outputs for various roughness-scaled features Diffuse performance of optics was examined using statistical profilometric parameters as inputs for the Generalized Harvey-Shack surface scatter theory. The theory was applied to optically flat, micro-rough, and nanorough surfaces, to access diffractive scatter for different feature size scales.

Scatter data using experimental height measurements traces the shape of the diffuse scatter, but does not indicate any strong specular response, suggesting the surfaces are purely diffuse, which is not observed in spectral nor scatter measurements. Although the contrast between specular and diffuse regions is less than expected, the axial transmission region contains most of the transmitted power, consistent with the antireflectivity of rARSS spectral measurements.

The surface feature data was consistent with Gaussian statistics; however, Gaussian statistics approximation of the nanorough surfaces scatter was not in agreement with experimental scatter data. Although the Gaussian model was unsuccessful, there may be other characteristic equations which can be used to describe the surface feature distribution. Surface height map profile data was utilized to generate the necessary inputs for the GHS, but it was inconsistent with measured data due to limitations in the theory for sufficiently small and dense surface features with a strong specular response among its more diffuse scatter behavior compared to optically flat components. Additional testing is necessary to improve consistency of GHS to predict scatter from surfaces with subwavelength features.

For rARSS, reducing the surface to a collection of surface roughness parameters and maintaining fidelity of modeled surface scatter is not possible. It was shown that the theory can predict redirection of light from the specular to diffuse region but was unable to predict enhancement of light throughput in the axial direction.

REFERENCES

[1] C. Wilson, T. Hutchens, G. Sapkota, J. Case, M. Potter, L. Busse, J. Frantz, L. Shaw, J. Sanghera, M. Poutous, I. D. Aggarwal, "Laser damage of silica optical windows with random antireflective structured surfaces," Opt. Eng. 57(12) 121906 (2018)

[2] H. Lee, B. Vattiat, U. Subash, M. Poutous, "Integration/test of dual unit arrayed wide-angle camera system and its evaluation in the context of Extremely Large Telescopes," Proc. SPIE 12184, Ground-based and Airborne Instrumentation for Astronomy IX, 121848E (2022)

[3] J. Vossen and W. Kern, Thin Film Processes, 1st ed. Elsevier Inc (1978)

[4] K. Iizuka, Engineering Optics, 3rd ed. New York, Springer-Verlag (2008)

[5] F. Gonzalez and M. Gordon. "Bio-inspired, sub-wavelength surface structures for ultra-broadband, omni-directional antireflection in the mid and far IR," Opt. Exp., vol. 22, no. 11 (2014)

[6] D. Hobbs, B. MacLeod, and J. Riccobono, "Update on the development of high performance antireflecting surface relief micro-structures," SPIE Proc. vol. (2007)

[7] S. Chattopadhyay, Y. Huang, Y.J. Jen, A. Ganguly, K. Chen, and L. Chen, "Anti-reflecting and photonic nanostructures," Materials Science and Engineering: R: Reports, vol. 69 (2010)

[8] Z. Lin, G. Wang, J. Tian, L. Wang, D. Zhao, Z. Liu, and J. Han. "Broad-band anti-reflective pore-like sub-wavelength surface nanostructures on sapphire for optical windows," Nanotechnology, vol 29 (2018)

[9] L. E. Busse, C. M. Florea, J. A. Frantz, L. B. Shaw, I. D. Aggarwal, M. K. Poutous, R. Joshi, and J. S. Sanghera, "Anti-reflective surface structures for spinel ceramics and fused silica windows, lenses and optical fibers", Opt. Mat. Exp., vol. 4, no. 12 (2014)

[10] A. Peltier, G. Sapkota, J. R. Case, M. K. Poutous, "Polarization insensitive performance of randomly structured antireflecting planar surfaces", Opt. Eng. 57(3) 037109:1-8 (2018)

[11] D. Gonzalez, J. Meza-Galvan, D. Sharp, K. Vijayraghavan and M. Poutous. "Optical scattering measurements of random anti-reflective nanostructured surfaces in the mid- and long-wave IR." Proc. SPIE 11289 (2020)

[12] Praneeth Gadamsetti and Menelaos K. Poutous, "Numerical study of feature-distribution effects for anti-reflection structured surfaces on binary gratings," Appl. Opt. 62, 3398-3408 (2023)

[13] B. Zollars, S. Savoy, and Q. Xue, “Antireflective structures for Optics,” US Patent Application Publication, US2015/0103396-A1 (2015)

[14] D. Gonzalez, M. K. Poutous, "Bidirectional scattering distribution function of random antireflective nano-roughened surfaces," Proc. SPIE 11682, Optical Components and Materials XVIII, 1168215 (2021)

[15] K. Kunala, M. K. Poutous, "Random antireflective nanostructuring on binary near-wavelength period gratings," Opt. Eng. 57(8) 087106 (2018)

[16] M. Piralaee, A. Asgari, V. Siahpoush, Modeling and optimizing the performance of plasmonic solar cells using effective medium theory, Physics Letters A, Volume 381, Issue 5 (2017)

[17] M. G. Moharam and T. K. Gaylord, "Rigorous coupled-wave analysis of planar-grating diffraction," J. Opt. Soc. Am. 71, 811-818 (1981)

[18] R. Rumpf, A. Tal, and S. Kuebler, "Rigorous electromagnetic analysis of volumetrically complex media using the slice absorption method," J. Opt. Soc. Am. A 24, 3123-3134 (2007)

[19] C. Musolff, The Surface Texture Answer Book, Digital Metrology Solutions, Inc (2021)

[20] J. Harvey, Understanding Surface Scatter Phenomena: A Linear Systems Formulation, 1st ed. Bellingham, Washington: SPIE Press (2019)

[21] J. Stover, Optical Scattering: Measurement and Analysis, 3rd ed. Bellingham, Washington: SPIE Press (2019)

[22] K. Guenther, P. Wierer, and J. Bennett, "Surface roughness measurements of low-scatter mirrors and roughness standards," Appl. Opt. 23, 3820-3836 (1984)

[23] H. Ragheb and E. Hancock. “The Modified Beckmann–Kirchhoff Scattering Theory for Rough Surface Analysis.” Pattern Recognition, vol. 40, no. 7 (2007)

[24] T. Small, S. D. Butler, M. A. Marciniak, "Uncertainty analysis for CCD-augmented CASI® BRDF measurement system," Opt. Eng. 60(11) 114101 (2021)

[25] J. Harvey, C. Vernold, A. Krywonos, and P. Thompson. Diffracted radiance: a fundamental quantity in nonparaxial scalar diffraction theory. Applied Optics: Vol. 38, No. 31. (1999)

[26] D. A. Gonzalez, J. Meza-Galvan, D. Sharp, K. Vijayraghavan, and M. K. Poutous, “Narrow-angle scatter of reflectivity-suppressing nanostructured surfaces”, Opt. Eng. 59(10), 103106:1-13 (2020)

[27] E. Church and J. Zavada. “Residual Surface Roughness of Diamond-Turned Optics.” Applied Optics, vol. 14, no. 8 (1975)

[28] J, Goodman, Introduction to Fourier Optics, 3rd ed. Roberts and Company Publishers (2004)

[29] J. Merle Elson and J. Bennett, "Calculation of the power spectral density from surface profile data," Appl. Opt. 34, 201-208 (1995)

[30] P.M. Lonardo, A.A. Bruzzone, A.M. Lonardo, Analysis of Machined Surfaces through Diffraction Patterns and Neural Networks, CIRP Annals, Volume 44, Issue 1 (1995)

[31] R. Shack and J. Harvey, "An Investigation of the Relationship between Surface Microroughness and Radiant Energy Scattering ", Final Report, SAMSO Contract No. 404701 -75 -C -0106 (1976)

[32] E. Weisstein, "Wiener-Khinchin Theorem." From MathWorld--A Wolfram Web Resource. https://mathworld.wolfram.com/Wiener-KhinchinTheorem.html

[33] O. Heavens, “Application of matrix method for evaluating reflectance and transmittance: a) The single film,” in Optical Properties of Thin Solid Films. New York: Dover Publications (1991)

[34] E. Centurioni, "Generalized matrix method for calculation of internal light energy flux in mixed coherent and incoherent multilayers," Appl. Opt. 44, 7532-7539 (2005)

[35] A. Krywonos, J. Harvey, N. Choi, "Linear systems formulation of scattering theory for rough surfaces with arbitrary incident and scattering angles," J. Opt. Soc. Am. A 28, 1121-1138 (2011)

[36] J. Harvey, N. Choi, A. Krywonos, J. Grasa Marcen, "Calculating BRDFs from surface PSDs for moderately rough optical surfaces," Proc. SPIE 7426, Optical Manufacturing and Testing VIII, 74260I (2009)

[37] A. Krywonos. Predicting Surface Scatter Using a Linear Systems Formulation of Non-Paraxial Scalar Diffraction. ProQuest Dissertations Publishing (2006)

[38] K. O’Donnell and E. Mendez, "Experimental study of scattering from characterized random surfaces," J. Opt. Soc. Am. A 4, 1194-1205 (1987)

[39] J. Gaskill, Linear Systems, Fourier Transforms, and Optics. New York: John Wiley & Sons (1978)

[40] V. Johansen, "Preparing the generalized Harvey–Shack rough surface scattering method for use with the discrete ordinates method," J. Opt. Soc. Am. A 32, 186-194 (2015)

[41] K. Nattinger, “Experimental validation of the generalized Harvey-Shack surface scatter theory”, Proc. SPIE 11485, Reflection, Scattering, and Diffraction from Surfaces VII, 1148503 (2020)

APPENDIX A: PUBLICATIONS AND PRESENTATIONS

Peer-Reviewed Publications

[1] **David A. Gonzalez**, Karun Vijayraghavan, and M. K. Poutous. "Surface scatter from random nanostructured dielectric interfaces". (In preparation)

[2] Praneeth Gadamsetti, Marcus Testorf, **David A. Gonzalez**, P. Batoni, and M. K. Poutous, "Implementation of a superresolution far-field spot-generator with 1/5 the diffraction limit", Results in Optics, Volume 3, 2021, 100067, ISSN 2666-9501

[3] **David A. Gonzalez**, J. Meza-Galvan, D. Sharp, K. Vijayraghavan, and M. K. Poutous, "Narrow-angle scatter of reflectivity-suppressing nanostructured surfaces", Optical Engineering 59(10), 103106 (2020)

[4] **David A. Gonzalez,** Jesus Meza-Galvan, David Sharp, Karun Vijayraghavan, and Menelaos K. Poutous. "Bi-directional scatter and single-surface reflectivity of random anti-reflective nanostructured surfaces." *Proc. IEEE HONET-ICT*, (2019). (Presented at IEEE-HONET-ICT 2019, Reviewed). Paper 94(1570589282)

Conference Proceedings

[1] **David A. Gonzalez**, and Menelaos K. Poutous, "Predictive model comparisons to axially-transmissive optical scatter measurements for anti-reflective random nanostructured surfaces", (Accepted for presentation at 2024 SPIE Photonics West OPTO, Paper 12882-26)

[2] Subhasree Srenevas, **David A. Gonzalez**, and Menelaos K. Poutous, "Organizational disorder of nanostructured antireflective surfaces", (Accepted for presentation at 2024 SPIE Photonics West OPTO, Paper 12880-46)

[3] **David A. Gonzalez**, Karun Vijayraghavan, and Menelaos. K. Poutous, "Random nanostructured infrared window scatter analysis using the Harvey-Shack transfer function method", Proc. SPIE 12430, Quantum Sensing and Nano Electronics and Photonics XIX, 1243018 (15 March 2023)

[4] **David A. Gonzalez**, Karun Vijayraghavan, Praneeth Gadamsetti, and Menelaos. K. Poutous, "Optical surface absolute specular reflectance measurement using an infrared etalon and interferometer combination method", Proc. SPIE 12008, Photonic Instrumentation Engineering IX, 1200809 (5 March 2022)

[5] **David A. Gonzalez**, Karun Vijayraghavan, and Menelaos. K. Poutous, "MWIR scatter of antireflective nanostructured windows", Proc. SPIE 11997, Optical Components and Materials XIX, 1199702 (4 March 2022)

[6] **David. A. Gonzalez**, M. K. Poutous, “Bidirectional scattering distribution function of random antireflective nano-roughened surfaces”, Proc. SPIE 11682, Optical Components and Materials XVIII, 1168215 (5 March 2021)

[7] Karun Vijayraghavan, **David A. Gonzalez**, Jesus Meza-Galvan, M. K. Poutous, “Mid-wave and long-wave IR angular scatter of random anti-reflective nanostructured surfaces on ZnS, ZnSe, and GaAs”, Proc. SPIE 11388, Image Sensing Technologies: Materials, Devices, Systems, and Applications VII, 1138806 (27 April 2020)

[8] **David A. Gonzalez,** Jesus Meza-Galvan, David Sharp, Karun Vijayraghavan, Menelaos K. Poutous. “Optical scattering measurements of random anti-reflective nanostructured surfaces in the mid- and long-wave IR”, Proc. SPIE 11289, Photonic and Phononic Properties of Engineered Nanostructures X, 112891Q (26 February 2020)

APPENDIX B: EQUIPMENT SPECIFICATIONS

Instrument	**Manufacturer**	**Location**	**Parameter**	**Specification**			
Vertex 80 FTIR spectrometer	**Bruker**	**Billerica, MA, USA**	Wavelength band	Visible		Infrared	
			Source	Halogen lamp		Globar	
			Detector (bandwidth)	Si (400 nm – 1111 nm) (25000 cm^{-1} – 9000 cm^{-1})		DLaTGS (0.833 μm – 40.0 μm) (12000 cm^{-1} – 250 cm^{-1})	
			Beamsplitter	CaF_2 (200 nm – 2500 nm) (50000 cm^{-1} – 4000 cm^{-1})		KBr (1.0 μm – 26.3 μm) (10000 cm^{-1} – 380 cm^{-1})	
			Experimental bandwidth	400 nm – 1000 nm		2.0 μm – 12 μm	
			Experimental spectral resolution	20.0 cm^{-1}		2.0 cm^{-1}	
			Experimental averaging	n = 200 samples		n = 100 samples	
			Modality	Transmission	Reflection	Transmission	Reflection
			Spot size	3.6 mm	3.73 mm x 3.6 mm	3.6 mm	3.73 mm x 3.6 mm
			Angle of incidence/collection	0° AOI, 0° AOC,	15° AOI, 15°-60° AOC	0° AOI, 0° AOC,	15° AOI, 15°-60° AOC
			Angular resolution (reflection only)		1°		1°
Complete Angle Scatter Instrument (CASI) scatterometer	**Scatterworks**	**Gresham ,OR, USA**	Source (wavelength)	HeNe Laser (633 nm) & IR HeNe Laser (3.39 μm)			
			Aperture size	340 μm	1.2 mm	4.8 mm	1.2 cm
			Angular range (± around specular)	0.564°	0.564°-1.666°	1.666°-4.306°	4.306°-90°
			Angular resolution	0.013°	0.063°	0.185°	0.478°
LEXT OLS5000	**Olympus**	**Center Valley, PA, USA**	Wavelength	405 nm			
			Sampling	4096 x 4096			
			Objective	10x	20x	50x	100x
			Sampled area	1.28 mm	640 μm	256 μm	128 μm
			Numerical aperture	0.30	0.60	0.95	0.95
			Working distance	10.4 mm	1.0 mm	0.35 mm	0.35 mm
			Spatial resolution	312.5 nm	156.25 nm	62.5 nm	31.25 nm
			Diffraction limited resolution (Rayleigh criterion)	1647 nm	823.5 nm	520.1 nm	520.1 nm

APPENDIX C: ADDITIONAL DATA

Each of the following sets of data include spectrum for double-sided processed rARSS and polished (optically flat) counterpart, reflected spectral scatter, in both polar logarithmic (directional diagram) and cartesian logarithmic format, and full reflection spectra contour. CASI measured scatter data and comparison to modeled scatter distribution using the GHS scatter theory using experimental height map data is listed following individual sample spectral data. Following rARSS scatter data, additional reflection data for diamond-turned Al of various periodicity is shown. Lastly, Spectralon 0.99 diffuse reflectance standard is shown as a reference for a nearly perfect Lambertian scattering surface.

Table A.1. Profilometric data for IR rARSS samples. Selected surface roughness parameters were obtained from analysis of UV confocal microscope images.

Sample	**S_q (μm)**	**S_a (μm)**	**S_z (μm)**	**S_{al} (μm)**	**S_{tr}**
rARSS ZnSe	0.051	0.039	1.088	41.422	0.649
rARSS ZnS	0.055	0.042	1.095	41.75	0.654
rARSS GaAs	0.079	0.059	1.573	41.469	0.649
rARSS Ge	0.102	0.071	2.389	39.359	0.616

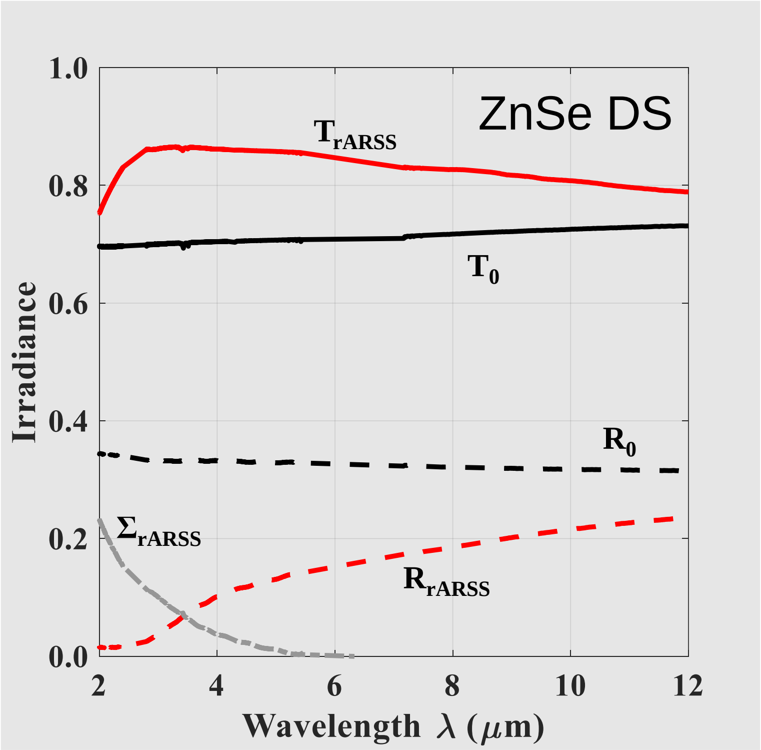

Figure A1. IR spectra for double-sided processed rARSS ZnSe and polished ZnSe.

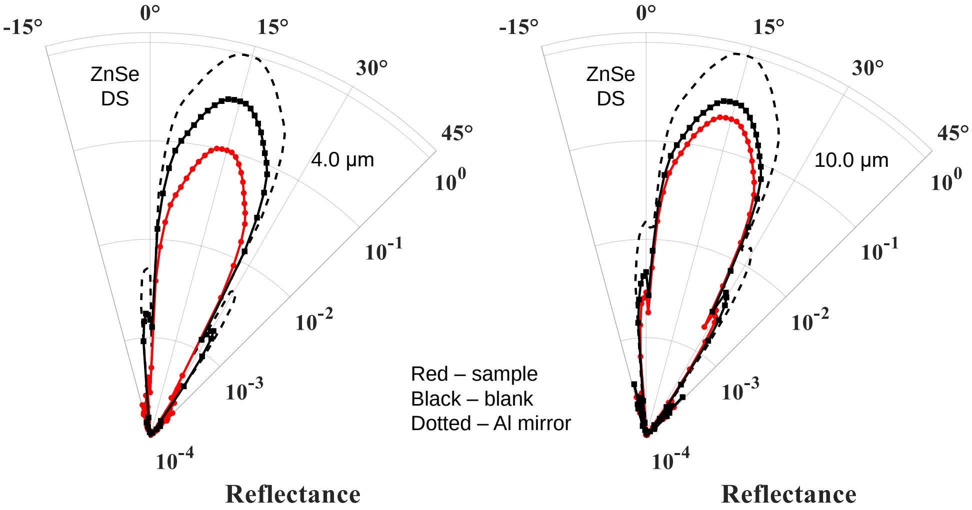

Figure A2. Directional diagram of ZnSe reflected scatter at 4 µm (right) and 10 µm (left). Al mirror (dotted), Polished (black), and rARSS (red) samples are compared.

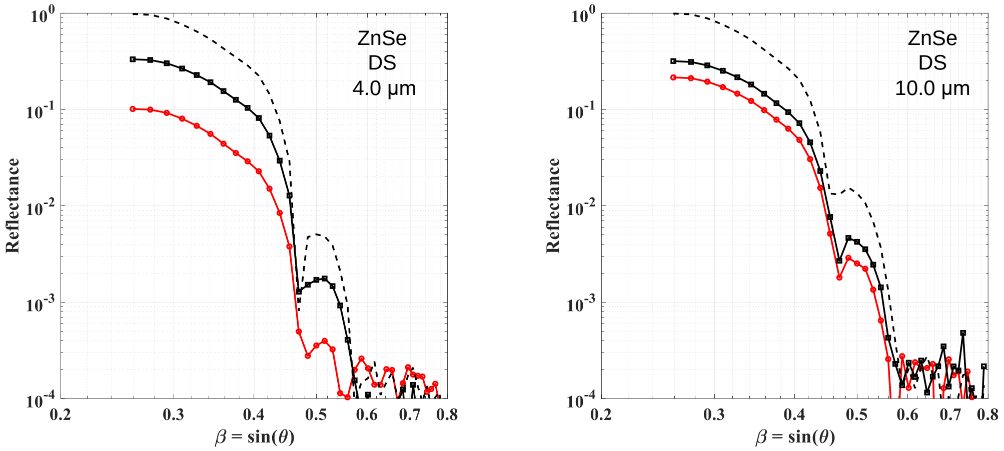

Figure A3. Logarithmic beta-projected reflectance distributions for ZnSe at 4 µm (left) and 10 µm (right).

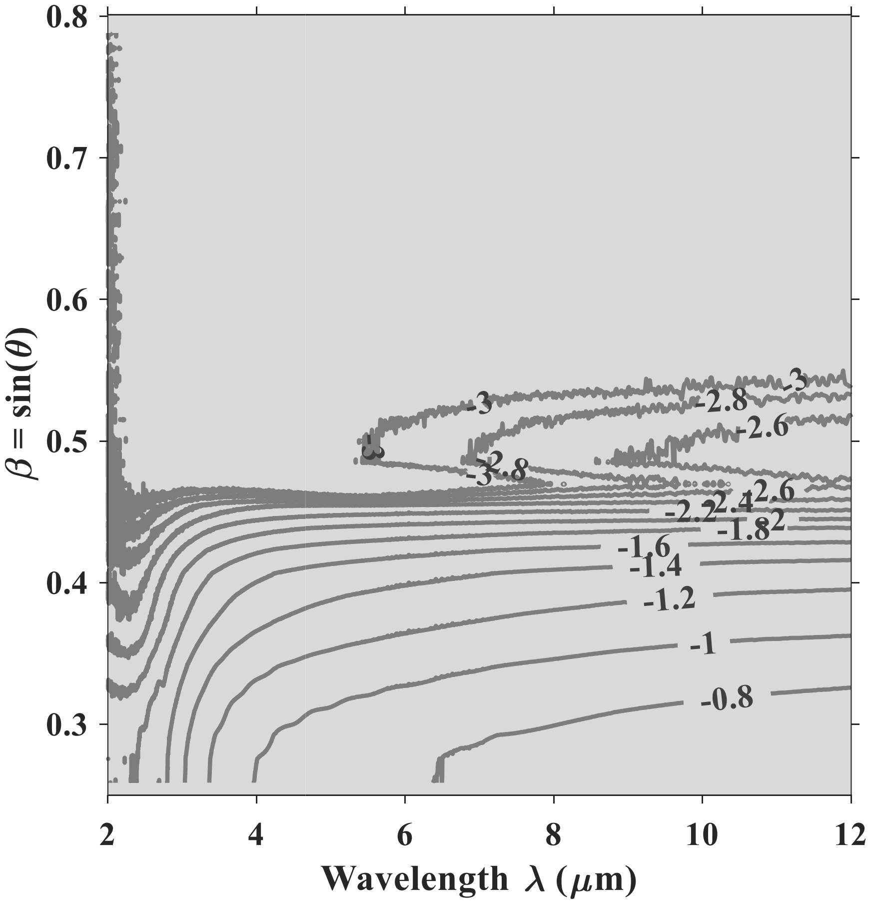

Figure A4. Reflection spectra contour map of double sided rARSS ZnSe.

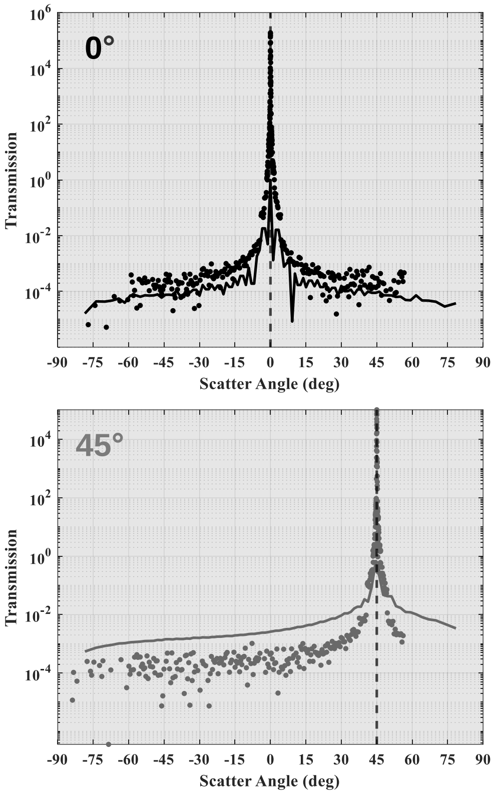

Figure A5. BTDF (points) and ASF (line) at 3.39 μm for nanostructured ZnSe at normal (black), 15° (red), 45°(grey), and 70° (dark red) AOI.

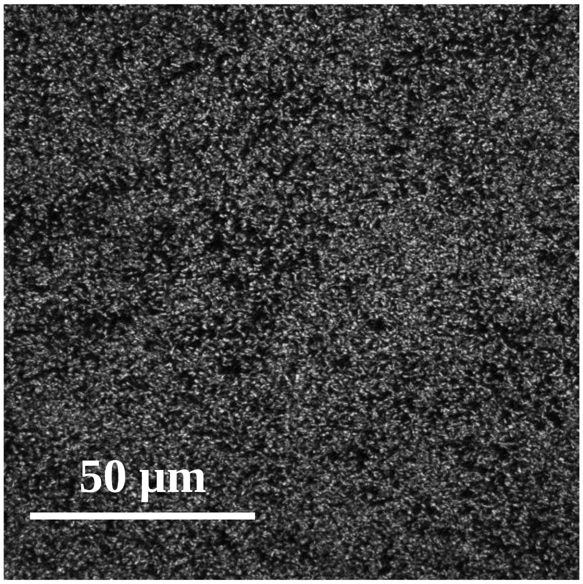

Figure A6. 100x magnification LEXT confocal image of nanostructured ZnSe.

Note: the first box covers all four panels.

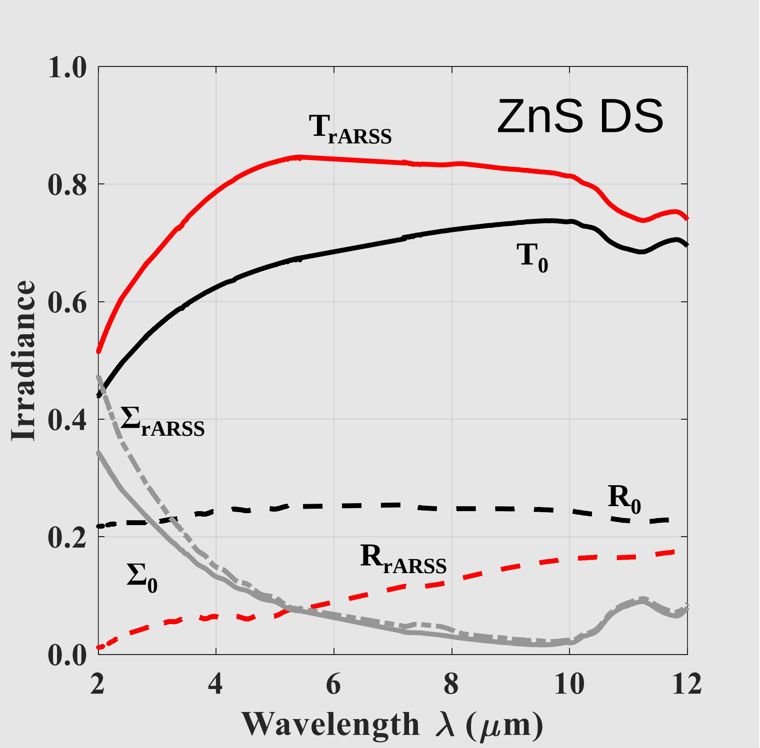

Figure A7. IR spectra for double-sided processed rARSS and polished ZnS.

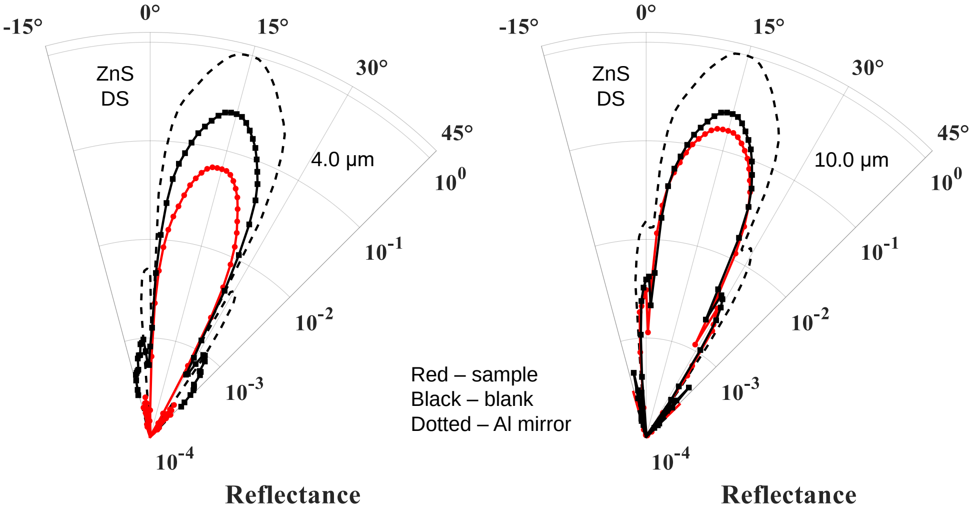

Figure A8. Directional diagram of ZnS reflected scatter at 4 µm (right) and 10 µm (left). Al mirror (dotted), Polished (black), and rARSS (red) samples are compared.

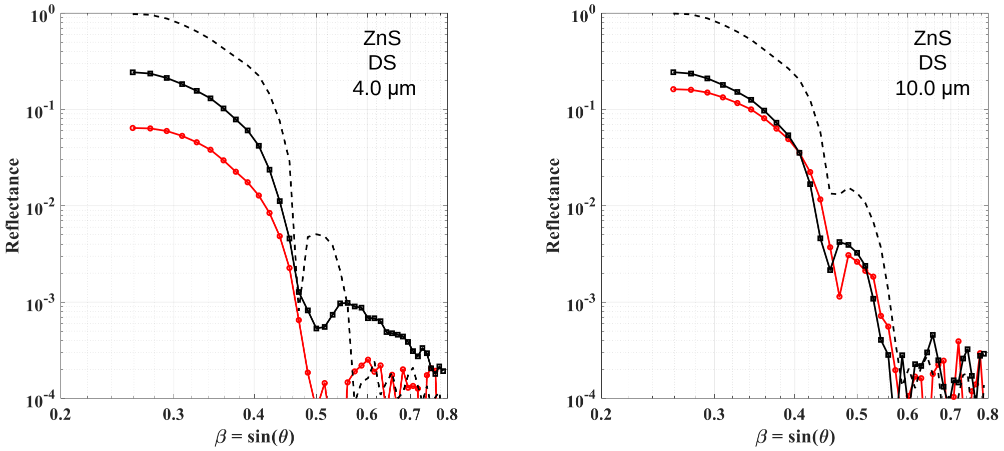

Figure A9. Logarithmic beta-projected reflectance distributions for ZnS at 4 μm (left) and 10 μm (right).

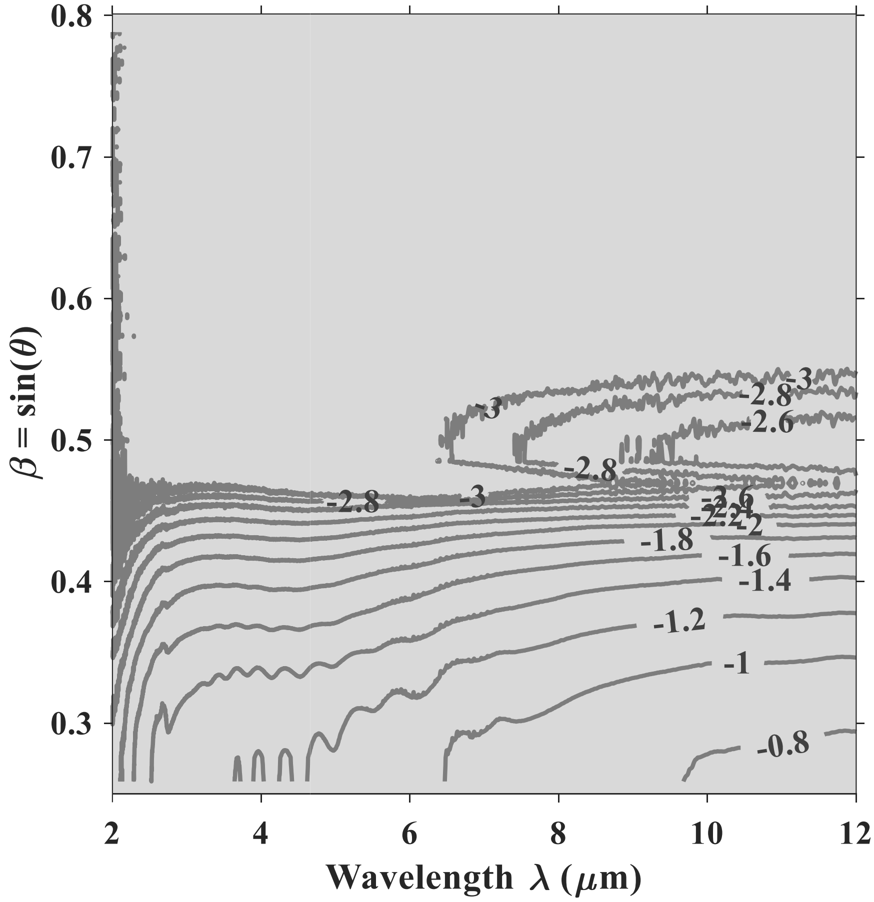

Figure A10. Reflection spectra contour map of double sided rARSS ZnS.

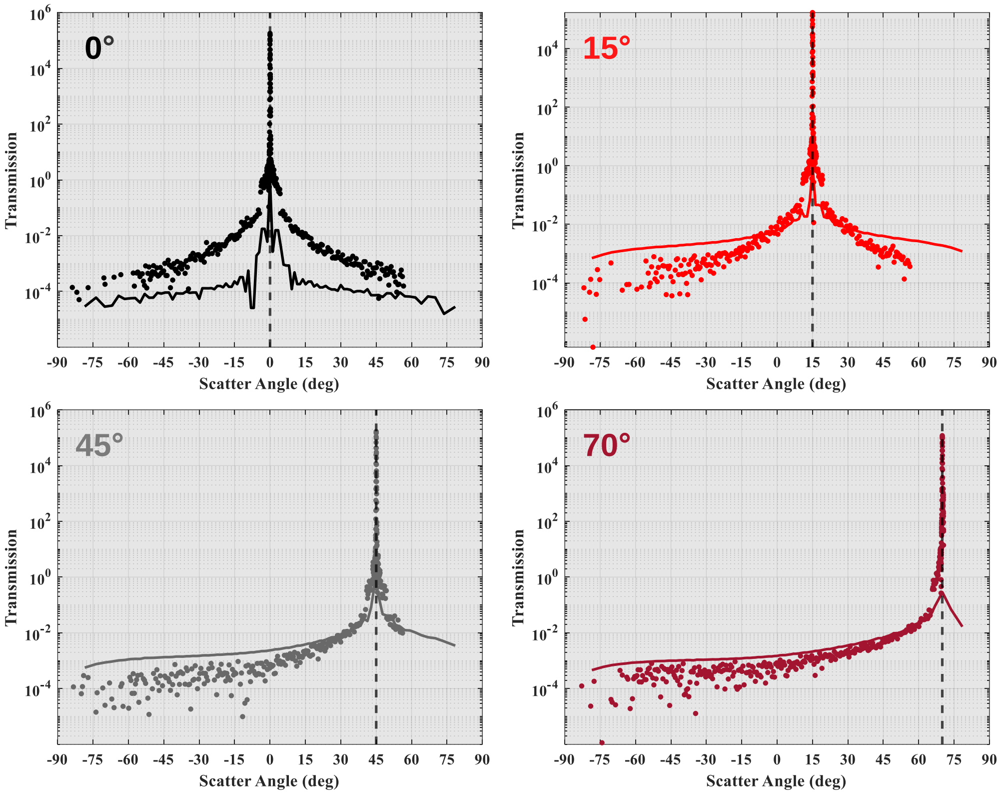

Figure A11. BTDF (points) and ASF (line) at 3.39 µm for nanostructured ZnS at normal (black), 15° (red), 45°(grey), and 70° (dark red) AOI.

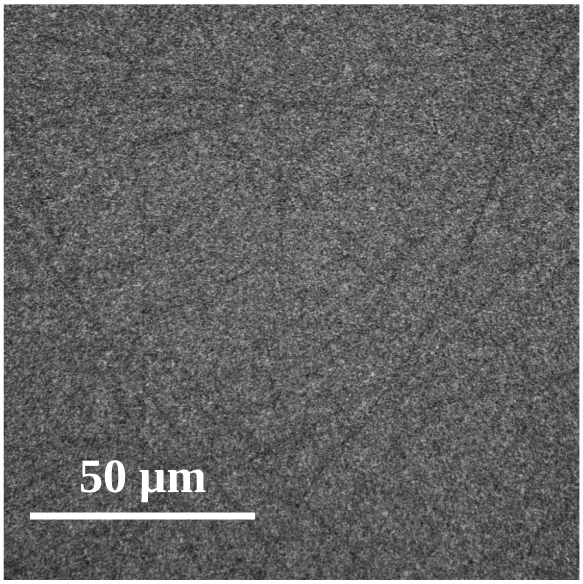

Figure A12. 100x magnification LEXT confocal image of nanostructured ZnS.

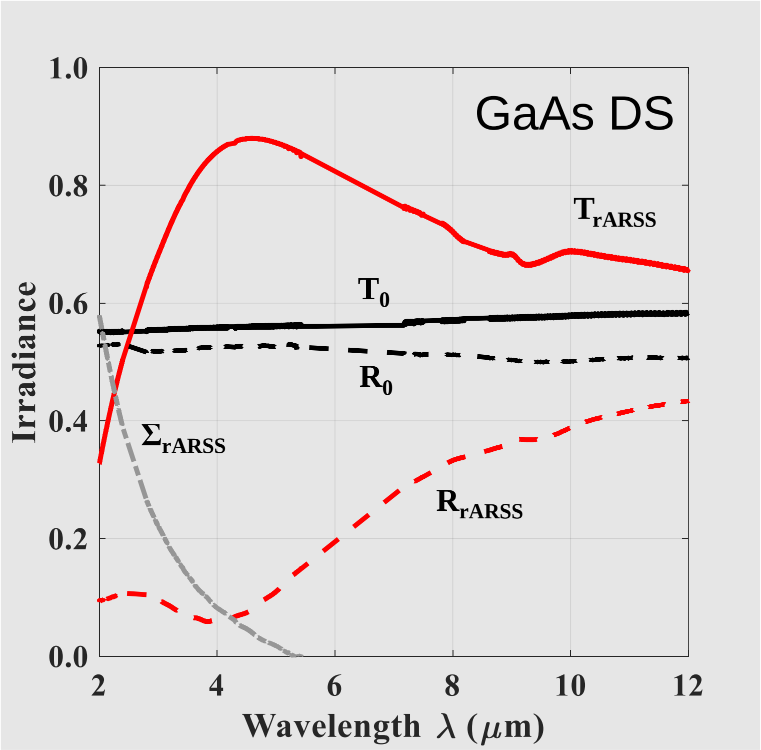

Figure A13. IR spectra for double-sided processed rARSS and polished GaAs.

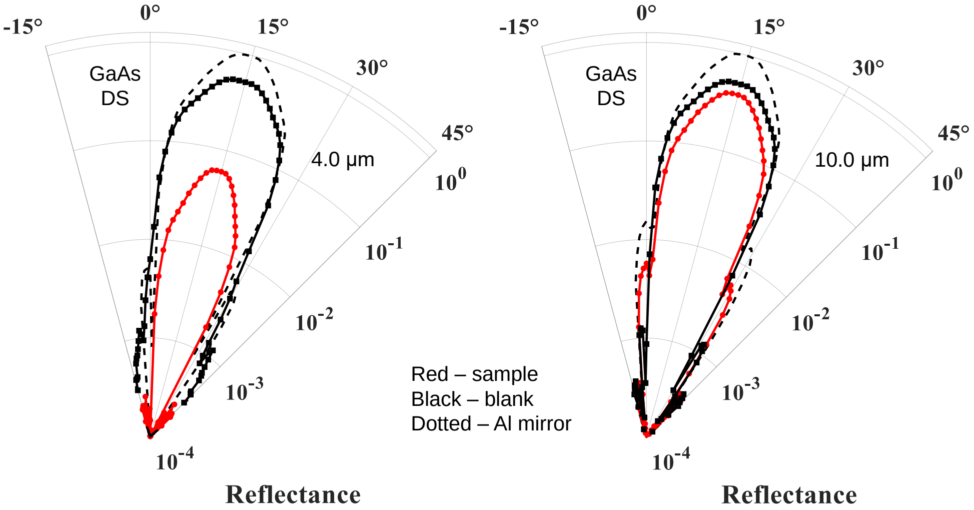

Figure A14. Directional diagram of GaAs reflected scatter at 4 μm (right) and 10 μm (left). Al mirror (dotted), Polished (black), and rARSS (red) samples are compared.

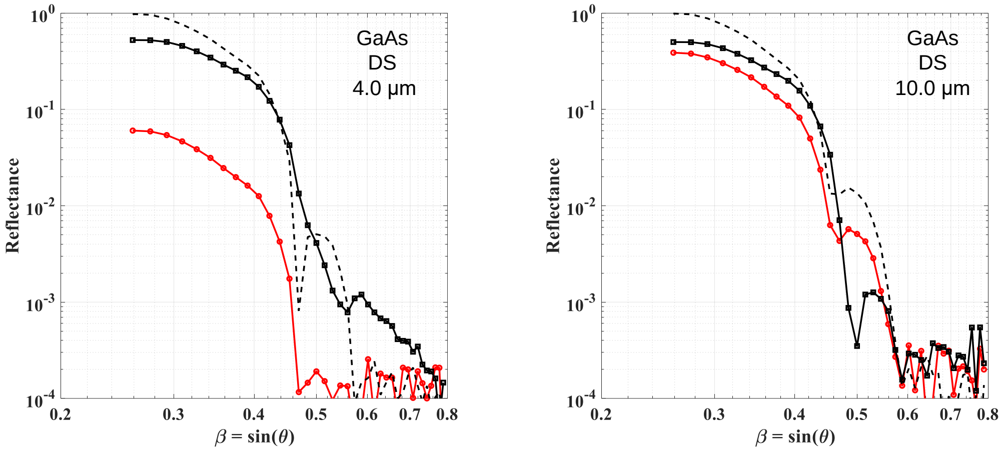

Figure A15. Logarithmic beta-projected reflectance distributions for GaAs at 4 μm (left) and 10 μm (right).

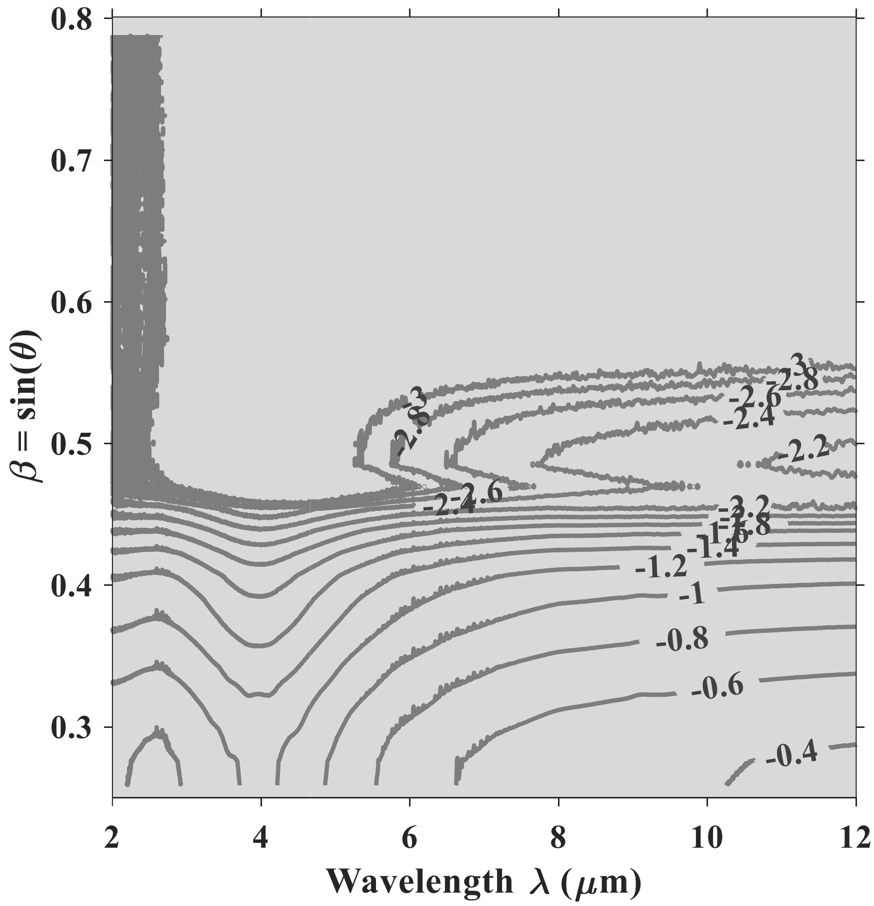

Figure A16. Reflection spectra contour map of double sided rARSS GaAs.

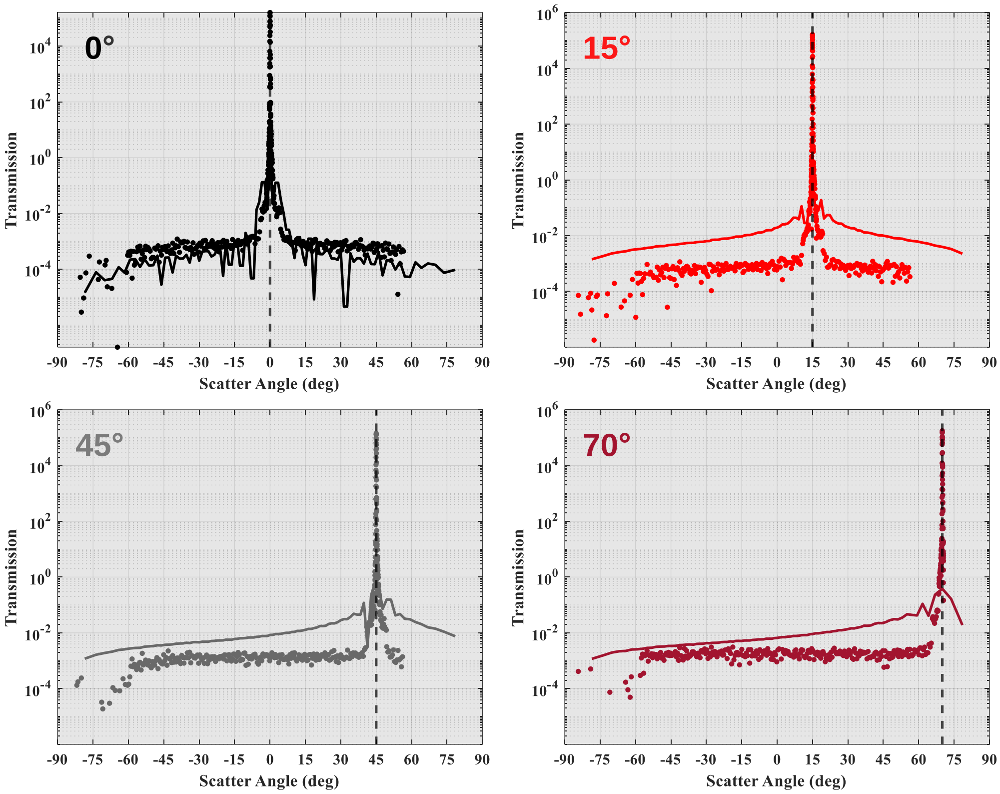

Figure A17. BTDF (points) and ASF (line) at 3.39 µm for nanostructured GaAs at normal (black), 15° (red), 45°(grey), and 70° (dark red) AOI.

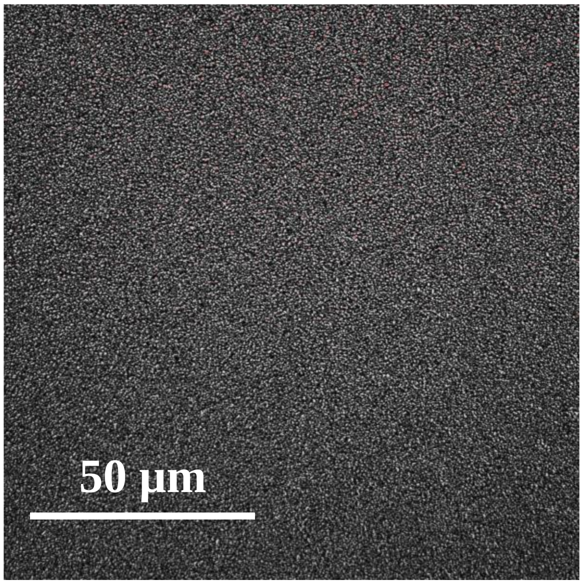

Figure A18. 100x magnification LEXT confocal image of nanostructured GaAs.

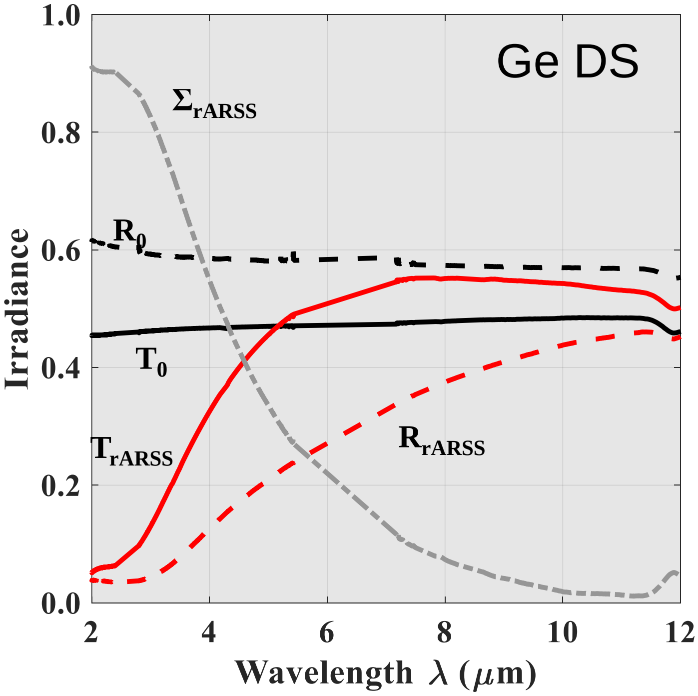

Figure A19. IR spectra for double-sided processed rARSS and polished Ge.

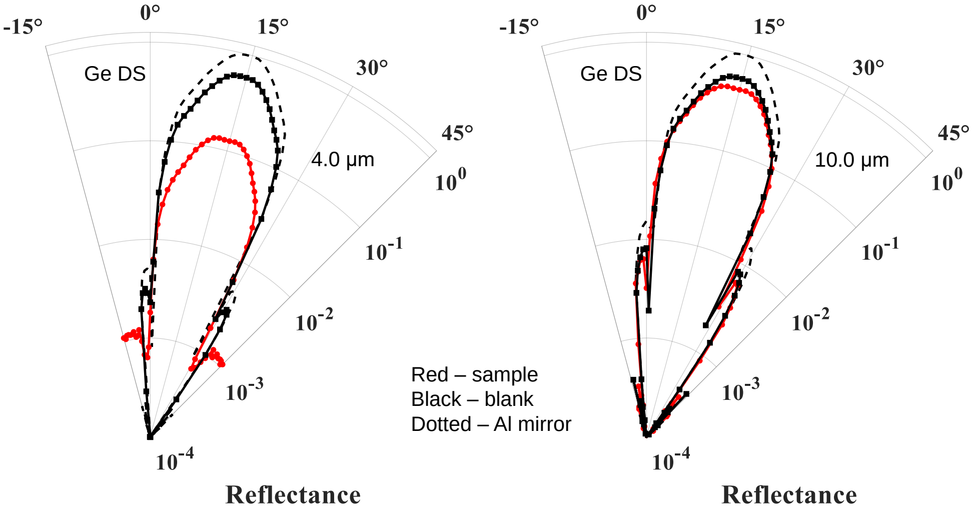

Figure A20. Directional diagram of Ge reflected scatter at 4 μm (right) and 10 μm (left). Al mirror (dotted), Polished (black), and rARSS (red) samples are compared.

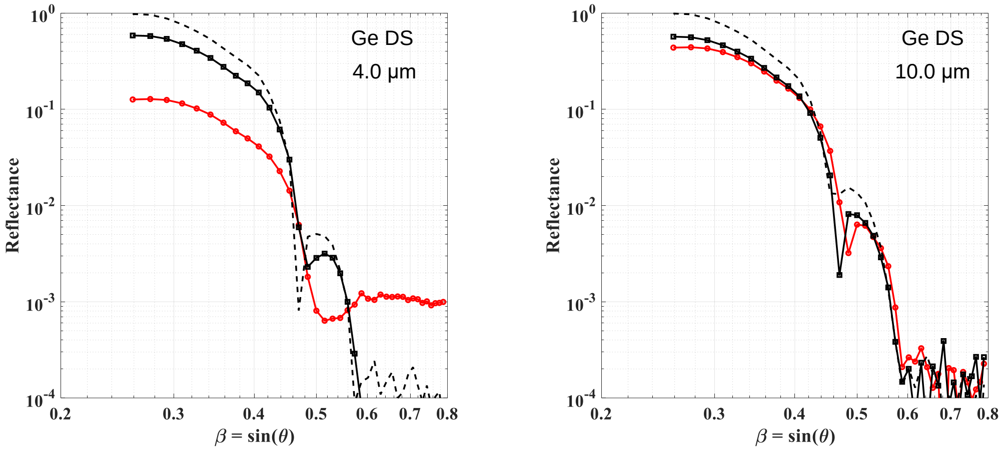

Figure A21. Logarithmic beta-projected reflectance distributions for Ge at 4 µm (left) and 10 µm (right).

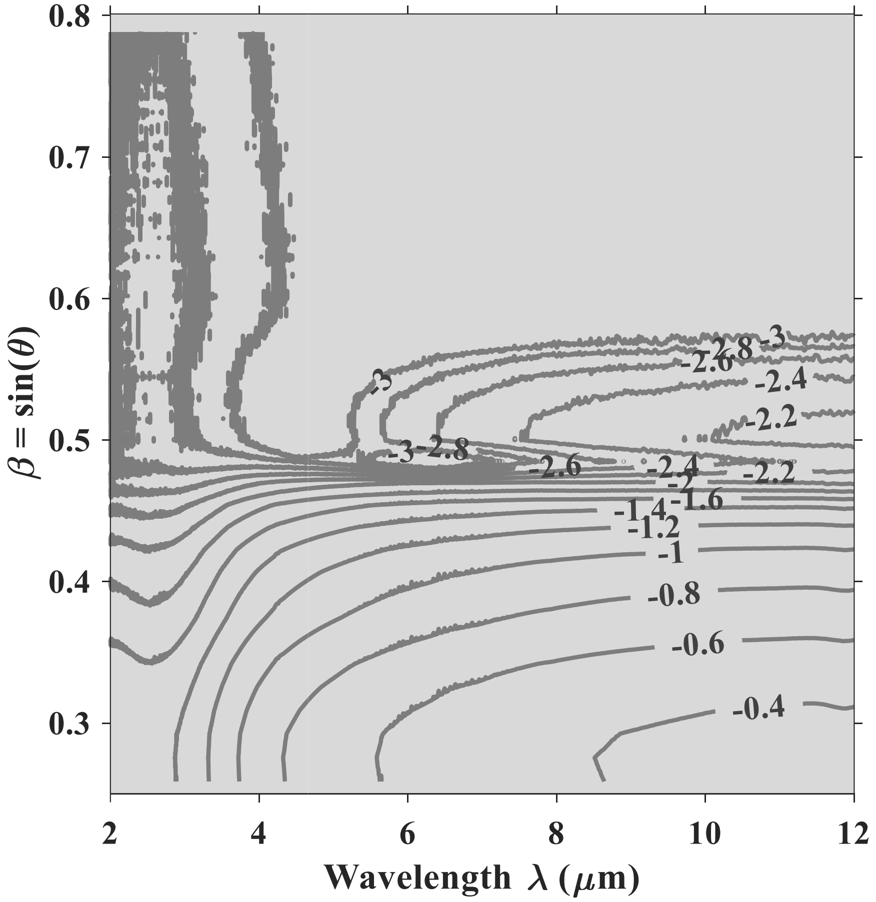

Figure A22. Reflection spectra contour map of double sided rARSS Ge.

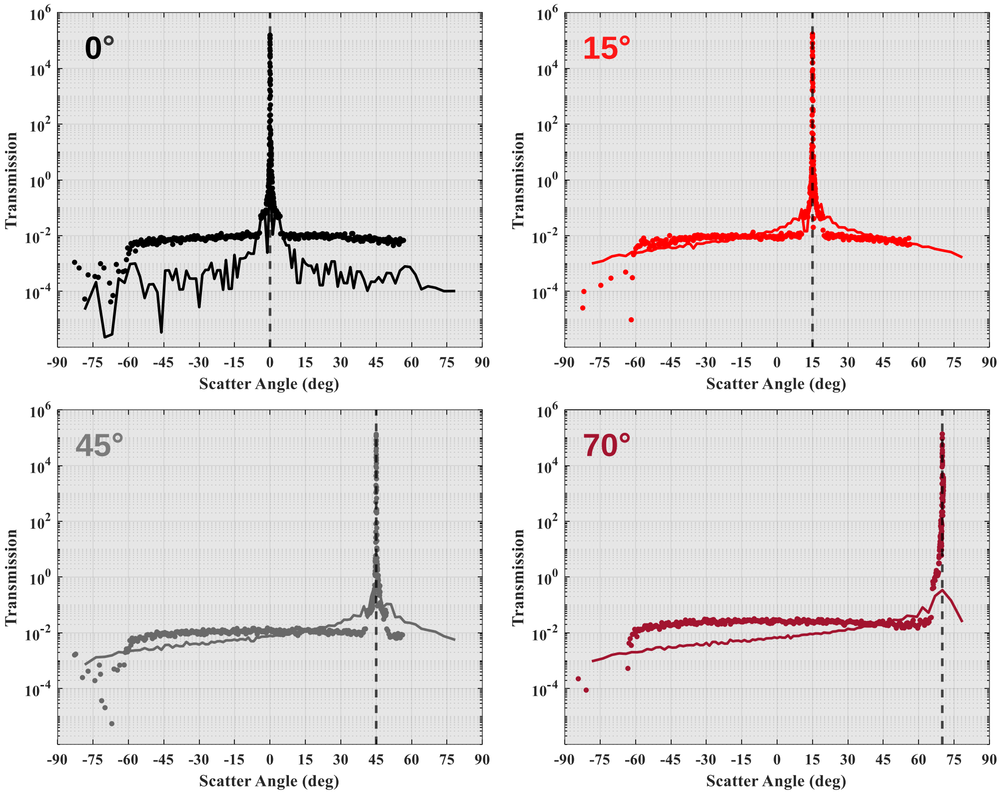

Figure A23. BTDF (points) and ASF (line) at 3.39 µm for nanostructured Ge at normal (black), 15° (red), 45°(grey), and 70° (dark red) AOI.

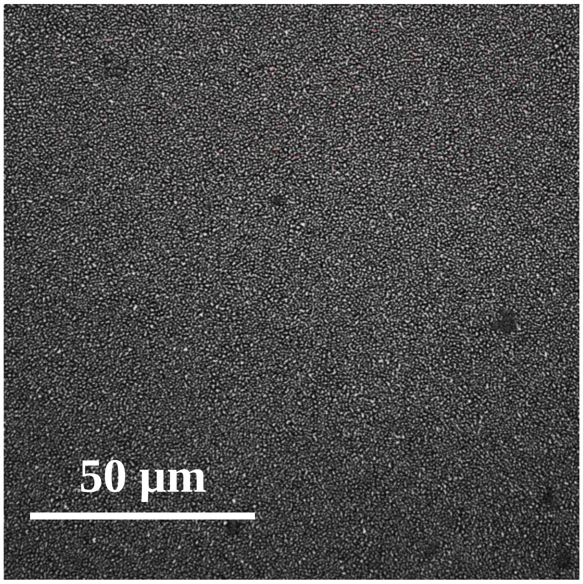

Figure A24. 100x magnification LEXT confocal image of nanostructured Ge.

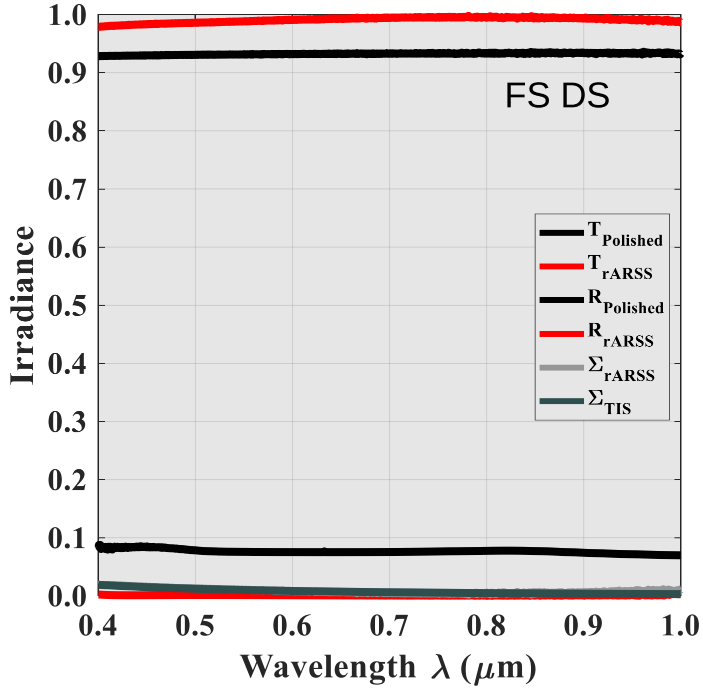

Figure A25. Visible spectra for double-sided processed rARSS and polished FS.

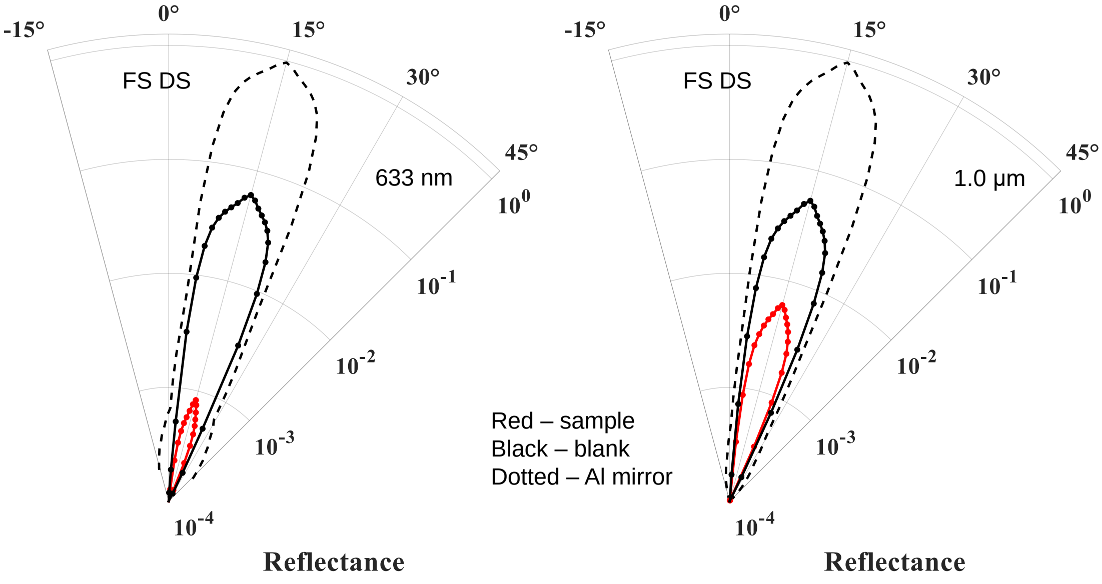

Figure A26. Directional diagram of FS reflected scatter at 633 nm (right) and 1000 nm (left). Al mirror (dotted), Polished (black), and rARSS (red) samples are compared.

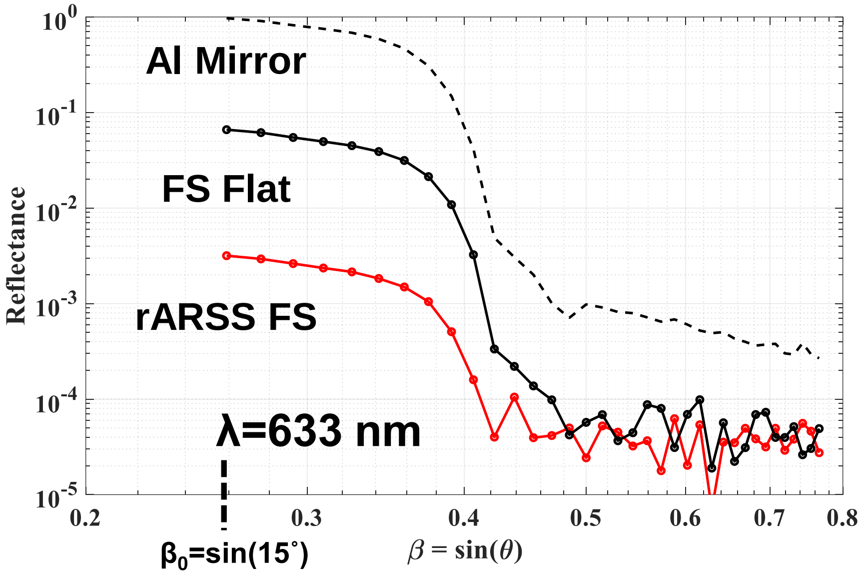

Figure A27. Logarithmic beta-projected reflectance distributions for FS at 633 nm.

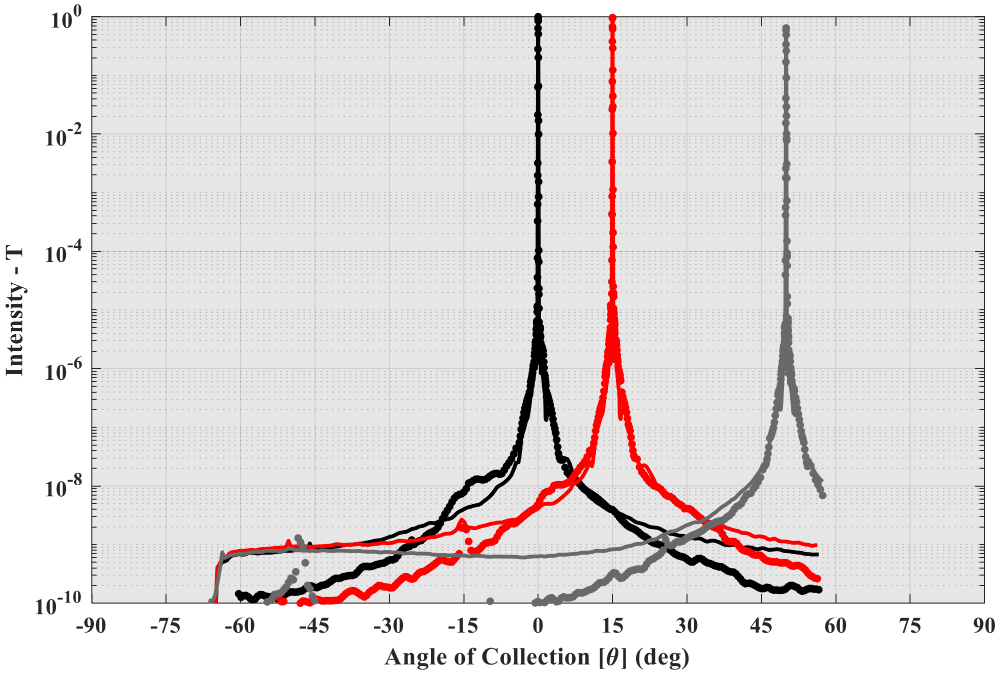

Figure A28. BTDF at 633 nm for nanostructured (solid line) and polished (dots) FS sample at normal (black), 15° (red), and 50°(grey) AOI.

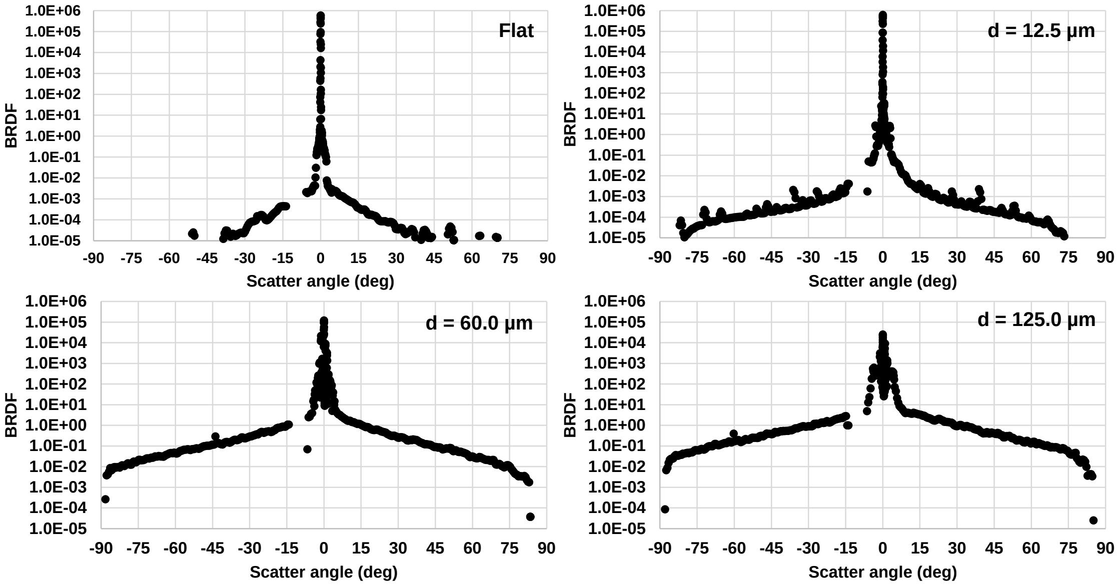

Figure A29. 5° AOI BRDF of Al mirrors with leftover tooling marks of period *d* from diamond turning process.

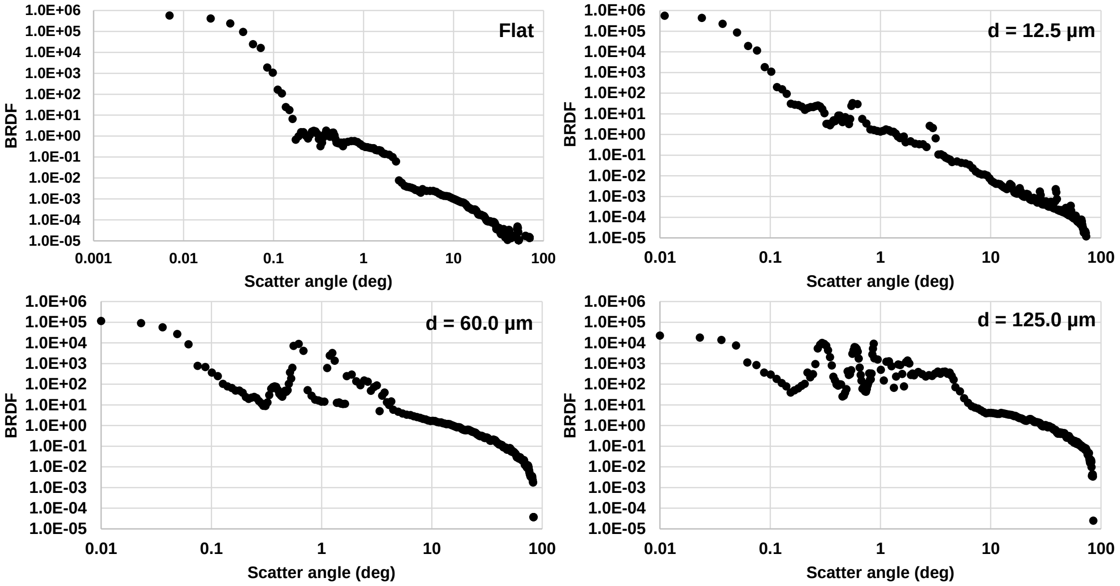

Figure A30. 5° AOI BRDF plotted vs. log-scaled angle of Al mirrors with leftover tooling marks of period *d* from diamond turning process. Diffraction orders due to surface periodicity are visible when plotting in a logarithmic format.

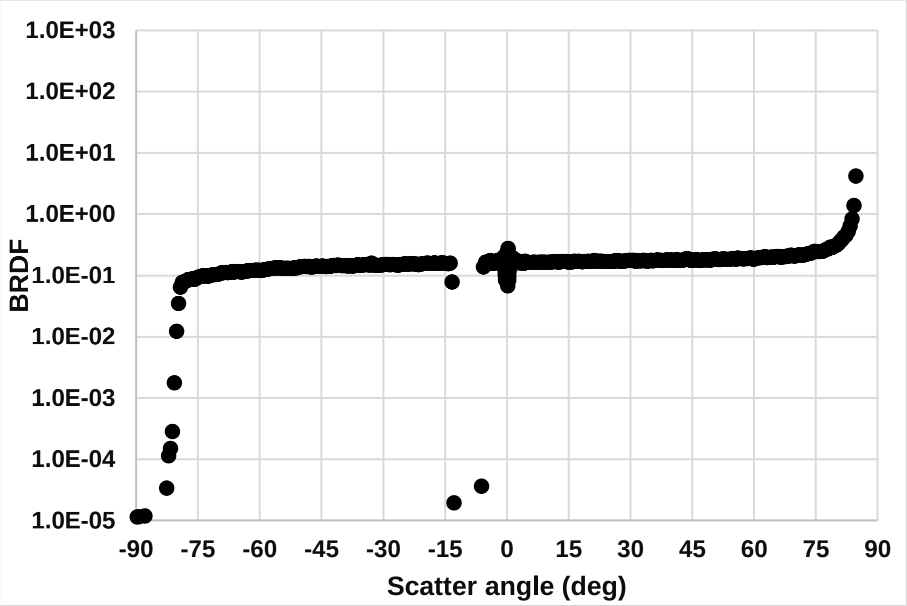

Figure A31. 5° AOI BRDF of Labsphere Spectralon 0.99 reflective diffuse reflectance standard. Sample scatter distribution is extremely Lambertian. The data is not cosine corrected. Measured wide angle (θ_s>70°) scatter shown here unrealistic to performance of the sample and is due to limitations in the scatterometer setup at glancing angles.